Computational Study of the Dynamics of the Flow-Field Induced by Vortex Generators

Pranav Manjunath

Technische Universiteit Delft

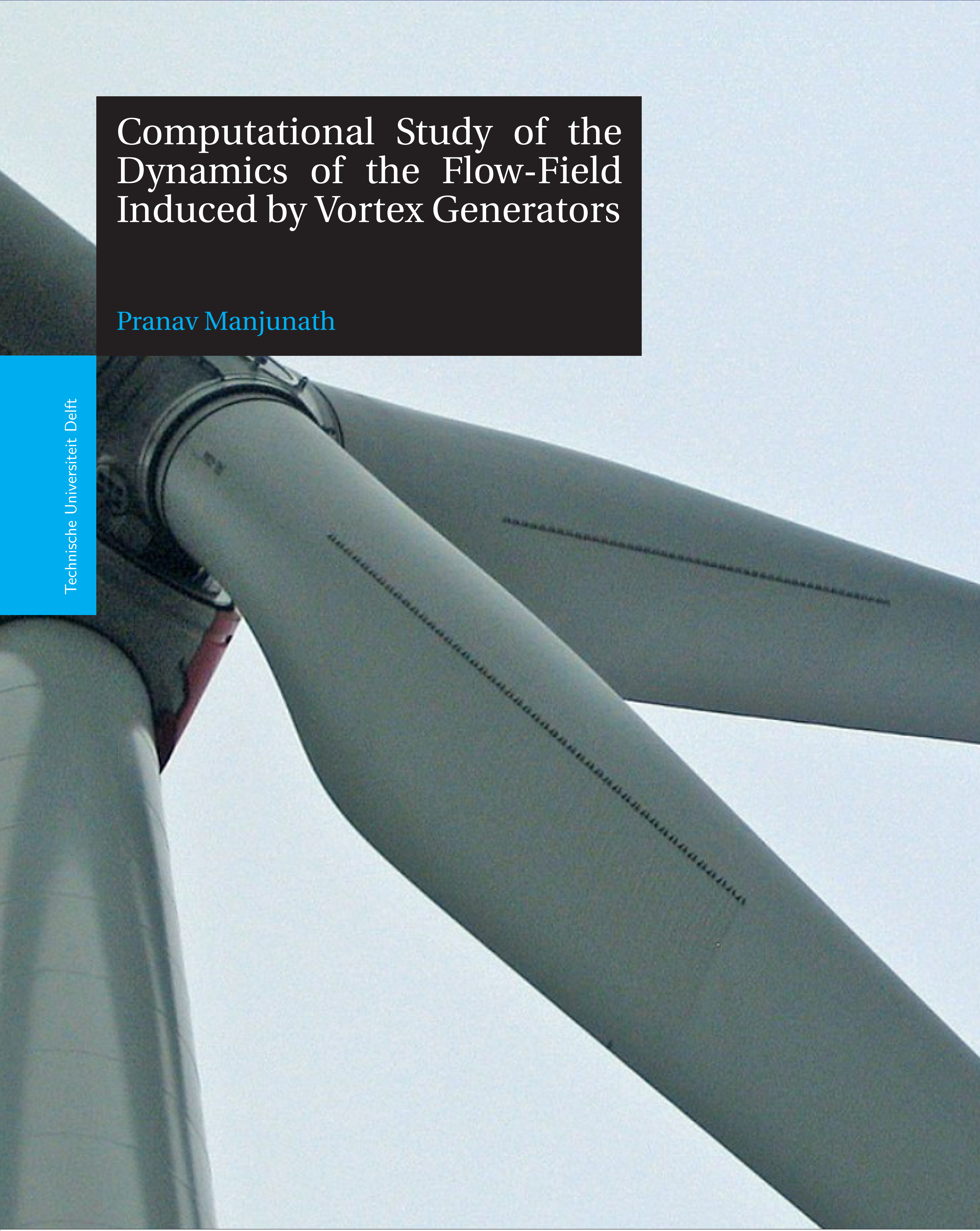

TUDelft
Delft
University of
Technology

Challenge the future

COMPUTATIONAL STUDY OF THE DYNAMICS OF THE FLOW-FIELD INDUCED BY VORTEX GENERATORS

by

Pranav Manjunath

in partial fulfillment of the requirements for the degree of

Master of Science
in Aerospace Engineering

at the Delft University of Technology,
to be defended publicly on Wednesday September 13, 2017 at 15:30 PM.

Student number:	4418174	
Thesis committee:	Prof. dr. Damiano Casalino	TU Delft, supervisor
	Dr. Steven Hulshoff ,	TU Delft
	Dr. Daniele Ragni ,	TU Delft
	Ir. Daniel Baldacchino ,	TU Delft, supervisor

An electronic version of this thesis is available at http://repository.tudelft.nl/.

TU Delft
Delft
University of
Technology

ACKNOWLEDGEMENT

It has been an exciting journey through TU Delft. Starting from zero to almost completing my masters now, time flies. Looking back, there have been some really good moments and some not so good ones as well. Nonetheless, I will cherish all of them and would like to do it all over again (may be a little bit better this time). I have many people to thank:Starting with my family back home, THANK YOU. Without their continued support, love and affection none of this would have been possible.

Next, I would like to thank my supervisors, Prof. Damiano, Daniel and Wouter. THANK YOU for being so patient with me and guiding me through out this adventure. I have made many mistakes en route and every time your bits of advice has always helped me. I will always be grateful for your time and help.

Finally, THANK YOU to all my friends here in Delft and the kite power room for being there for me whenever I needed them!!

Pranav Manjunath
Delft, September 2017

SUMMARY

Vortex Generators (VGs) are one of the most commonly used passive flow control devices. Recent studies have shown that it is beneficial to use Sub-Boundary Layer Vortex Generators (SBVGs). The height of these generators varies between 10% – 50% of the boundary layer thickness. It offers an improvement over conventional VGs in the form of reduced device drag. However, the reduced height causes the induced vortices to be substantially weaker. Therefore using SBVG is beneficial only when the regions of flow separation are well defined. Therefore, there is a need to better understand induced flow-field to comprehensively predict the effectiveness of SBVGs for flow control over a range of operating conditions,

This thesis aims to characterise the flow-field induced SBVGs in a laminar boundary layer flow. To this end, PowerFLOW 5.3b a commercial lattice-Boltzmann solver is used. For analysis, two different SBVGs profile; Rectangular vortex generators (RVGs) and Triangular vortex generators (TVGs) are considered. For both the SBVG profiles, the topic of interest includes mean flow, instantaneous flow, far-field acoustic properties and influence of angle of attack of the VG vane.

To analyse the properties of the induced flow-field dominated by vortices different vortex identification such as velocity discriminant, Q-criteria and λ_2-criteria are reviewed. Of these, λ_2-criteria which is the most restrictive of the above-mentioned techniques is used. However, initial vortex identification results did not match with the visualised flow-field. Therefore, to overcome this, λ_2-criteria is effectively combined with the flow topology based Γ_2-criteria. Using this modified criteria in general, resulted in more accurate vortex identification. Consequently, the properties of the induced vortices for both mean flow and instantaneous flow are determined using the modified criteria.

The main results of the study include the noted presence of secondary vortices, the emergence of local re-circulation zones in between the vanes for RVGs and the properties of the unsteady nature of the vortices.

Visualisation of the mean flow for both the VG profiles shows the presence of secondary vortices in addition to the primary vortices. For RVGs, downstream of the vane one secondary vortex with the same direction of rotation as the primary is observed. However, for the TVGs, two secondary vortices with opposite direction of rotation to the primary is seen. Therefore, the origin, nature and number of secondary vortices are influenced by the VG profile. Further, these secondary vortices are also seen to be sensitive to change in angle of attack of the VG vane.

For the RVGs with an increase in angle of attack of the vane, local re-circulation zones are noted. However, with TVGs this was not observed. The stronger primary vortices and an adverse pressure gradient between the vanes in case of the RVGs is likely responsible for the re-circulation zones.

In case of both the VGs magnitude of unsteady displacement or meandering of primary vortices increases with the downstream position. The increase in angle of attack of the vanes also increased meandering of the vortices. Further, the direction of this meandering is seen to be influenced by the nearest vortex.

In addition to this, results of acoustic far-field spectra for both the VG profiles indicate a minimal contribution to the far-field noise.

Based on the results in this study the secondary vortices are seen significantly influence the properties of the primary vortices aft of the VG vanes. Therefore, effectively managing the secondary vortices using suitable design changes to VG profile could be one of the possible ways to accomplish better flow control.

CONTENTS

List of Figures ix

List of Tables xiii

1 Introduction 1
- 1.1 Introduction 1
- 1.2 Flow Separation and Flow Control 1
- 1.3 Project Definition 3
  - 1.3.1 Research Objective 3
  - 1.3.2 Document Outline 3

2 Background 5
- 2.1 Boundary Layer Parameters 5
  - 2.1.1 Laminar and Turbulent Boundary Layer 6
- 2.2 Aeroacoustics 9
  - 2.2.1 Mechanism of Aerodynamic Noise 10
  - 2.2.2 Noise Prediction 12

3 Vortex Generator Flow 15
- 3.1 Vortex Generator Configuration 15
- 3.2 Induced Flow Field 16

4 Methodology 21
- 4.1 Numerical Simulation 21
  - 4.1.1 Flow Field Simulation 21
  - 4.1.2 Acoustic Radiation Prediction 22
- 4.2 Test Cases 23
- 4.3 Grid Convergence Study 24
- 4.4 Vortex Identification 26
  - 4.4.1 Vorticity Magnitude 26
  - 4.4.2 Velocity Discriminant 26
  - 4.4.3 Q - Criteria 27
  - 4.4.4 λ_2 - Criteria 27
  - 4.4.5 Γ_1 and Γ_2 Criterion 29
  - 4.4.6 Modified Criteria 30

5 Results and Discussion 33
- 5.1 Data Acquisition 33
- 5.2 Rectangular Vortex Generator 34
  - 5.2.1 Mean Flow-Field Properties 34
  - 5.2.2 Instantaneous Flow-Field Properties 38
  - 5.2.3 Acoustics and Surface Pressure Properties 45
- 5.3 Triangular Vortex Generator 47
  - 5.3.1 Mean Flow-Field Properties 47
  - 5.3.2 Instantaneous Flow-Field Properties 50
  - 5.3.3 Acoustics and Surface Pressure Properties 56
- 5.4 Influence of change in Angle of Attack the VG 58
  - 5.4.1 Rectangular Vortex Generator 58
  - 5.4.2 Triangular Vortex Generator 64

6 Conclusions and Recommendations **73**
6.1 Conclusions . . . 73
6.2 Recommendations and Future Research . . . 74

A Appendix **77**
A.1 Turbulent Boundary Layer Validation . . . 77
A.1.1 Computational Setup for Turbulent Boundary Layer Case . . . 79

Bibliography **81**

LIST OF FIGURES

1.1 Illustration of HAWT and VAWT [1]. . . . 1
1.2 Illustration of Flow Separation [2]. . . . 2
1.3 Illustration of On demand Vortex Generator [3]. . . . 3
1.4 Illustration of Vortex generator. . . . 3

2.1 Boundary layer development over flate plate [2]. . . . 5
2.2 Comparison between the Laminar and Turbulent boundary layer [4]. . . . 6
2.3 Blasius profile for boundary layer on a flate-plate in zero pressure gradient conditions, [4]. . . . 7
2.4 Idealised sketch of Natural boudary layer transition [2]. . . . 8
2.5 Typical laminar, transitional and turbulent boundary layer profiles on flate plate[5]. . . . 8
2.6 Mean velocity profile for turbulent boundary layer in terms of u^+ and y^+. [$\circ$] - boundary layer experiments Klebanoff (1954), $Re_\theta = 8000$; [$--$] - boundary layer DNS of Spalart (1988), $Re_\theta = 1410$; [$-$] - van Driest's law of wall [6]. . . . 9
2.7 Illustration of intraction of turbulent eddies with airfoil.[7]. . . . 10
2.8 Illustration of mechanism of laminar boundary layer instability noise.[8]. . . . 11
2.9 Illustration of mechanism of Tubulent boundary layer trailing edge noise.[8]. . . . 11
2.10 Illustration of mechanism of Trailing edge bluntness noise.[8]. . . . 11
2.11 Illustration of mechanism of Tip noise.[8]. . . . 12
2.12 Illustration of mechanism of Separation-Stall noise.[8]. . . . 12
2.13 Illustration of $f(x,t)$ in a domain with a solid body [7]. . . . 14

3.1 Illustration of some of the commonly used differnt VG profiles [9]. . . . 15
3.2 Different configuration of induced vortices. (a) Co-rotating (b) Counter-rotating, common down-wash (c) Counter-rotating, common up-wash. . . . 16
3.3 Map of different possible vortex configuration 17
3.4 (a) Spanwise PDF of vortex centre position (b) Wall-normal PDF of vortex centre position. At $\frac{x}{h}$ = 5.5. [10]. . . . 18
3.5 Mean indicative function for counter-rotating VG arrangement.[11]. . . . 18

4.1 Illustration of the D3Q19 model. . . . 22
4.2 Illustration of Rectangular VG vanes (RVGs) and Triangular VG vanes (TVGs). . . . 24
4.3 Illustration of the VG configuration. . . . 24
4.4 Illustration of the computational domain for laminar boundary layer flow. . . . 24
4.5 Variation of spatially averaged surface pressure in time on VG vane. . . . 25
4.6 Energy content in the different frequencies for the Coarse, Medium and Fine grids. . . . 26
4.7 Instanstaneous vortex induced by the Rectangular VG vane, $\beta = 8°$. . . . 28
4.8 Illustration of Γ_1 calculation. . . . 29
4.9 Illustration of inflection point. . . . 30
4.10 Comparision of the λ_2 - Criteria and the Modified Criteria. . . . 30

5.1 Illustration of the downstream data planes. . . . 33
5.2 Illustration Microphone arrangement for the Sound Pressure Level and directivity plots. . . . 34
5.3 Mean flow-field at $\frac{x-x_{vg}}{h} = 5$ for RVG, $\beta = 14°$. The background contour indicates the axial velocity whereas, the in-plane velocity is indicated by the arrows. . . . 34
5.4 Vorticity contour and downstream evolution of peak streamwise vorticity for RVGs, $\beta = 14°$ 35
5.5 Streamwise evolution of vortex centre paths for RVGs, $\beta = 14°$ 36
5.6 Iso-surface λ_2-criteria with a threshold of -1×10^6 illustrating primary and secoundary vortices for RVGs, $\beta = 14°$. . . . 36
5.7 Recirculation zones surrounding the RVG vane, $\beta = 14°$. . . . 37

5.8 C_p at $\frac{y}{h} = 0.5$ for RVGs, $\beta = 14^\circ$. 37
5.9 C_p along $\frac{z}{h} = 0$ for RVGs, $\beta = 14^\circ$. 37
5.10 Downstream development of the mean velocity profile along $\frac{z}{h} = 0$ for RVG, $\beta = 14^\circ$. 37
5.11 Instantaneous flow-field at $\frac{x-x_{vg}}{h} = 5$ for RVG vanes, $\beta = 14^\circ$. 38
5.12 Streamwise vorticity contour at $\frac{x-x_{vg}}{h} = 5$ for RVGs, $\beta = 14^\circ$ and $t \approx 0.25$s. 38
5.13 Instantaneous peak vorticity at different downstream positions at $t = 0.25$ and variation of peak vorticity at $\frac{x-x_{vg}}{h} = 5$ in time. 39
5.14 Instantaneous vortex centres for RVGs, $\beta = 14^\circ$ at $\frac{x-x_{vg}}{h} = 5$. 39
5.15 Wall-normal and spanwise displacement of the primary counter-clockwise vortex for RVG vanes, $\beta = 14^\circ$ at $\frac{x-x_{vg}}{h} = 5$. 40
5.16 Wall-normal and spanwise displacement of the primary clockwise vortex for RVG vanes, $\beta = 14^\circ$ at $\frac{x-x_{vg}}{h} = 5$. 41
5.17 PDF from the instantaneous vortex centres for RVG vanes, $\beta = 14^\circ$ at $\frac{x-x_{vg}}{h} = 5$. 41
5.18 Illustration of the chracteristic angle,(θ_{eig}) . 42
5.19 Meandering characteristics for RVG, $\beta = 14^\circ$. 42
5.20 Schematic of strain (coloured arrows) induced by the neghouring vortex in a counter-rotating arrangement Leweke *et al.*. 43
5.21 Schematic of the Reynolds Shear Stress due to isotropic meandering [13]. The thick black circle represents the vortex with the iso-values of the RSS represented in the background. 43
5.22 Axis of preferred direction of motion (dashed red line) overlapping the distribution of RSS, $\overline{v'w'}$ for RVG , $\beta = 14^\circ$ at $\frac{x-x_{VG}}{h} = 5$. 44
5.23 Power spectrum of the spanwise component of velocity, for RVG, $\beta = 14^\circ$. 44
5.24 SPL Spectrum for RVG, $\beta = 14^\circ$. 45
5.25 Standard deviation of the surface pressure BPF between frequencies, $f = 2000 - 2400 Hz$ on the suction side for RVG, $\beta = 14^\circ$. 45
5.26 λ_2 visualisation of the averaged flow-field with standard deviation of the surface pressure BPF between frequencies, $f = 2000 - 2400 Hz$. 46
5.27 Directivity plot for RVG, $\beta = 14^\circ$ for $f = 2000 - 2400 Hz$. 46
5.28 Mean flow-field at $\frac{x-x_{vg}}{h} = 5$ for TVG, $\beta = 14^\circ$. The background contour indicates the axial velocity whereas, the in-plane velocity is indicated by the arrows. 47
5.29 Mean streamwise vorticity at $\frac{x-x_{vg}}{h} = 5$ for TVG, $\beta = 14^\circ$. 48
5.30 Downstream evolution of peak streamwise vorticity for TVG, $\beta = 14^\circ$. 48
5.31 Streamwise evolution of mean vortex centre for TVG, $\beta = 14^\circ$. 49
5.32 Iso-surface λ_2-criteria with a threshold of -1×10^6 illustrating primary and secoundary vortices for TVGs, $\beta = 14^\circ$.. 49
5.33 Visualisation of the local re-circulation zones in the flow-field around the TVG vane, $\beta = 14^\circ$. 50
5.34 C_p along $\frac{z}{h} = 0$ for TVG vane, $\beta = 14^\circ$. 50
5.35 Downstream development of the mean velocity profile along $\frac{z}{h} = 0$ for TVG, $\beta = 14^\circ$. 51
5.36 Instantaneous flow-field at $\frac{x-x_{vg}}{h} = 5$ for TVG vanes, $\beta = 14^\circ$.The background contour represents the axial component of the velocity, whereas the arrows depict the in-plane velocity. 51
5.37 Instantaneous streamwise vorticity in the flow-field at $\frac{x-x_{vg}}{h} = 5$ for TVG vanes, $\beta = 14^\circ$. 52
5.38 Instantaneous vortex centres for TVG vanes, $\beta = 14^\circ$ at $\frac{x-x_{vg}}{h} = 5$. 52
5.39 Wall-normal and spanwise displacement of the primary counter-clockwise vortex for TVG vanes, $\beta = 14^\circ$ at $\frac{x-x_{vg}}{h} = 5$. 53
5.40 Wall-normal and spanwise displacement of the primary clockwise vortex for TVG vanes, $\beta = 14^\circ$ at $\frac{x-x_{vg}}{h} = 5$. 53
5.41 PDF of instantaneous vortex centres for TVG vanes, $\beta = 14^\circ$ at $\frac{x-x_{vg}}{h} = 5$. 54
5.42 Meandering characteristics for TVG, $\beta = 14^\circ$. 54
5.43 Axis of preferred direction of motion (dashed red line) overlapping the distribution of Reynolds shear stress, $\overline{v'w'}$ for TVG , $\beta = 14^\circ$ at $\frac{x-x_{vg}}{h} = 5$. 55
5.44 Power spectrum of the spanwise component of velocity, TVG $\beta = 14^\circ$. 55
5.45 Spectrogram for Probe-2 and Probe-3, TVG vanes, $\beta = 14^\circ$. 56
5.46 SPL Spectrum for TVG, $\beta = 14^\circ$. 57
5.47 Standard deviation of the surface pressure BPF between frequencies, $f = 400 - 800 Hz$ on the suction side for TVG, $\beta = 14^\circ$. 57

5.48 λ_2 visualisation of the averaged flow-field with standard deviation of the surface pressure BPF between frequencies, $f = 400-800Hz$ on the suction side for TVG, $\beta = 14°$. 57
5.49 Streamwise evolution $|\omega_{peak}|$ for RVGs at various β. 58
5.50 Streamwise vorticity contour at $\frac{x-x_{vg}}{h} = 5$ for for RVGs at various β. 59
5.51 Variation in vortex circulation for RVGs with change in β at $\frac{x-x_{vg}}{h} = 5$. 60
5.52 Downstream development of the mean velocity profile and the associated shape factor, H along $\frac{z}{h} = 0$ for RVG, at different β. 61
5.53 Iso-Surface of streamwise component of velocity lesser than zero for different β. 61
5.54 C_p along bottom surface at $\frac{z}{h} = 0$ for RVG for various β. 62
5.55 Variation of meandering characteristics for RVG with change in β at $\frac{x-x_{vg}}{h} = 5$. 63
5.56 Power spectrum of the spanwise component of velocity at $\frac{x-x_{vg}}{h} = 5$ for RVG vanes at different angle of attack (β). 64
5.57 SPL Spectrum for RVG at $\beta = 8°, 14°, 20°$and$30°$. 64
5.58 Streamwise evolution $|\omega_{peak}|$ for TVGs at various β. 65
5.59 Iso-surface of the λ_2 criteria with a thershold of -1×10^6 in the mean flow-field around the TVGs at $\beta = 8°$, $14°$, $20°$ and $30°$. 66
5.60 Streamwise vorticity contour at $\frac{x-x_{vg}}{h} = 5$ for TVGs at various β 67
5.61 Illustration of the vortex sytem for $\beta = 14°$, with primary vortex (P_1) and seondary vortices ($S_{1,2}$). 67
5.62 Variation in vortex circulation for RVGs with change in β at $\frac{x-x_{vg}}{h} = 5$. 68
5.63 Downstream development of the spanwise averaged mean velocity profile and the associated shape factor, H for TVGs at different β. 68
5.64 Variation of local-recirculation zones for TVGs at various β 69
5.65 Variation of meandering characteristics for TVG with change in β at $\frac{x-x_{vg}}{h} = 5$. 70
5.66 Power spectrum of the spanwise component of velocity at $\frac{x-x_{vg}}{h} = 5$ for TVG vanes at different angle of attack (β). 71
5.67 SPL Spectra for TVGs at $\beta = 8°, 14°, 20°$and$30°$. 71

A.1 Blasius profile as a function of height and corresponding local Reynolds number, Re 78
A.2 Mean value of streamwise velocity in a plane parallel to the wall at $\frac{y}{h_{strip}} = 1$. 78
A.3 Iso- surface of λ_2 - criteria in the mean flow-field around the zigzag strip, with a threshold of -1×10^5. 79
A.4 Comparision of mean velcity profile at downstream station $60\delta_0$ with Osterlund et al. (2001) [14]. 79
A.5 Comparision of Reynolds shear stress scaled in inner layer variables and plotted with outer layer variables. 80
A.6 Illustration of the computational domain for turbulent boundary layer flow. 80

LIST OF TABLES

4.1 Summary of the computational setup. 25
4.2 Different Grid Resolution 25

5.1 Variation of OSPL with β for RVG. 63
5.2 Variation of OSPL with β for TVG 70

A.1 Zigzag Strip details 77
A.2 Summary of the Computational Domain. 80

NOMENCLATURE

Acronyms

Symbol	Description	Units
CWT	Continuous wavelet transform	-
DNS	Direct numerical simulation	-
FWH	Ffowcs Williams-Hawkings	-
$HAWTs$	Horizontal axis wind turbines	-
LBL	Laminar boundary layer	-
LBM	Lattice Boltzmann method	-
LES	Large eddy simulation	-
$ODVG$	On-demand vortex generator	-
PIV	Particle image velocimetry	-
RVG	Rectangular vortex generator	-
$SBVG$	Sub-boundary layer vortex generator	-
TBL	Turbulent boundary layer	-
TVG	Triangular vortex generator	-
$VAWTs$	Vertical axis wind turbines	-
VG	Vortex generator	-

Greek Symbols

Symbol	Description	Units
β	Angle of attack	deg
δ	Boundary Layer thickness	m
δ^*	Displacement thickness	m
ϵ	Volumetric flow rate	$m^3 s^{-1}$
Γ	Circulation	$m^2 s^{-1}$
μ	Dynamic viscosity	$kg m^{-1} s^{-1}$
ν	Kinematic viscosity	$m^2 s^{-1}$
Ω	Collision operator	-
ω	Vorticity	s^{-1}
ρ	Density	$kg m^{-3}$
σ	Standard deviation	-

τ	Relaxation time	s
τ_w	Wall shear stress	Pa
θ	Momentum thickness	m
θ_{eig}	Preferred direction of motion	deg
u_τ	Wall frictional velocity	ms^{-1}

Subscripts

Symbol	Description	Units
∞	Freestream	-
$mean$	Mean flow	-
$peak$	Peak value	-
ref	Reference	-
rms	Root mean square	-
vg	Trailing edge of the vortex generator	-

Other Symbols

Symbol	Description	Units
c	Speed of sound	ms^{-1}
C_p	Pressure coefficient	-
f	Frequency	s^{-1}
f_i	Particle density distribution function	-
f_s	Sampling frequency	s^{-1}
H	Shape factor	-
h	Vortex generator height	m
h_s	Distance between limiting streamlines	m
l	Vortex generator length	m
M	Mach number	-
$OASPL$	Overall Sound Pressure Level	dB ref:$2 \times 10^{-5} Pa$
p	Pressure	Pa
p_{con}	Rate of convergence	-
PDF	Probability density function	-
PSD	Power spectral density	-
Re	Reynolds number	-
SPL	Sound Pressure Level	dB ref:$2 \times 10^{-5} Pa$
t	Time	s
u	Streamwise component of velocity	ms^{-1}

v	Wall-normal component of velocity	ms^{-1}
w	Spanwise component of velocity	ms^{-1}
x	Streamwise direction	m
y	Wall-normal direction	m
y_s	Distance to the streamline from the surface	m
z	Spanwise direction	m

1

INTRODUCTION

1.1. INTRODUCTION

Wind energy is today considered as a potentially low cost and an environmentally friendly alternative for generating power when compared to conventional techniques of using fossil fuel. The wind turbines based on their axis of rotation is broadly classified as either horizontal axis wind turbines (HAWTs) or vertical axis wind turbines (VAWTs). An illustration of wind turbines is as shown in Figure 1.1.

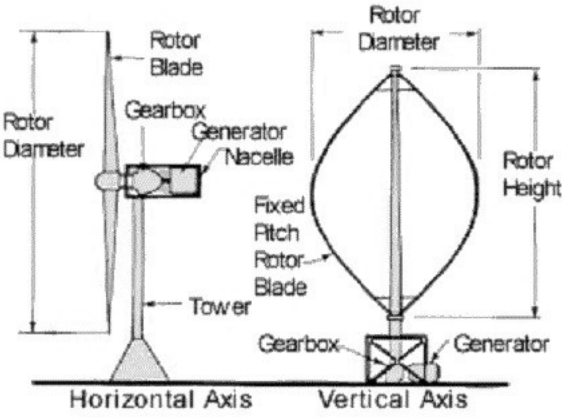

Figure 1.1: Illustration of HAWT and VAWT [1].

The performance of a wind turbine is directly related to the aerodynamic performance of its blades. The blades are designed to perform optimally for a certain range of freestream conditions, called the operating range. Due to the varying freestream conditions occasionally the operating conditions fall outside the operating range, resulting in a diminished performance. Thus, the variable operating conditions make it necessary for the blades to have a broad operating range, to extract the maximum possible energy. Additionally, soiling or surface degradation of the blades also results in diminished performance. It is not feasible to design a blade by considering all these parameters to ensure that it performs ideally under all circumstances. However, it is possible to increase the operating range by using techniques such as passive blade twist control, aerodynamic flow control, etc. These techniques not only help in reducing the excessive aerodynamic load on the blades and associated components but also enable the engineers to reclaim some of the lost performance due to degradation. Hence these techniques beneficial for the design of a lighter and more sustainable wind turbine blades.

1.2. FLOW SEPARATION AND FLOW CONTROL

For a fluid flow around a body immersed in a viscous medium, the nature/state of the boundary layer plays a significant role in determining the net aerodynamic performance. Consider the particles of fluid in the boundary layer, close to the wall; they experience resistance from frictional forces at the wall. Additionally, under certain circumstances flow encounters an additional resistance in the form of an adverse pressure gradient which further retards the fluid particles. Thus, under these conditions, if the particles do not have sufficient kinetic energy, they break away from the adjacent surface to result in a phenomenon called as flow separation. The occurrence of flow separation in the presence of a persistent adverse pressure gradient ($\frac{dp}{dx} > 0$) is illustrated in Figure 1.2.

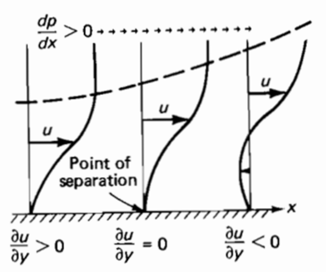
$\frac{dp}{dx} > 0$
u
u
u
Point of separation
x
$\frac{\partial u}{\partial y} > 0$
$\frac{\partial u}{\partial y} = 0$
$\frac{\partial u}{\partial y} < 0$

Figure 1.2: Illustration of Flow Separation [2].

In Ashill *et al.* (2005) it is shown that, based on the analytical expression 1.1 :

$$\frac{1}{2}\omega_w {y_s}^2 h_s = \epsilon \tag{1.1}$$

where, ω_w is the vorticity at the wall, h_s is the distance between the limiting streamlines, y_s is the height of the streamlines from the surface and ϵ is the volumetric flow rate, it is possible to have two mechanisms of flow separation. Firstly, when the magnitude of vorticity at the wall vanishes, it results in the formation of a bubble which isolates a part of the fluid from the main stream. This type of separation is also called as singular separation. Alternately, if the distance between the limiting streamlines becomes very small, it can lead to separation along a line.

The occurrence of flow separation is undesired as it results in energy losses and is also a source of noise. Thus, it is necessary to prevent the occurrence of flow separation. Although this can't be accomplished in all scenarios, it is possible to, at least delay the occurrence of separation in multiple ways, some of which as listed by Ashill *et al.* (2005):

- Increased mixing between upper and lower layers of boundary layer (Example: Using vortex generators).
- Directly increasing the energy in the lower layers of boundary layer (Example: Using tangential blowing on the walls).
- Reducing the adverse pressure gradient (Example: modifying the body shape).

These techniques constitute of what is know as Aerodynamic flow control or Flow control. Further, it is possible to classify aerodynamic flow control into Active flow control and Passive flow control. Active flow control, as the name suggest involves the application of flow control in response to current flow conditions. As a result, in active flow control desired performance gain is achieved, only when necessary, using a suitable feedback mechanism. When flow conditions are normal, no flow control is applied. An example of such a system is the On-Demand Vortex Generators (ODVG) illustrated in Figure 1.3 developed by NASA (Pack and Joslin, 1998). On the other hand, passive flow control technique involves no feedback mechanisms nor can it be selectively applied. An example of passive flow control device is Vortex Generators (VGs), illustrated in Figure 1.4.

The effectiveness and simplicity of VGs make it one of the most widely employed techniques in dealing with flow separation. Thus in the present thesis, it is of primary interest and its working is discussed in detail in Section 3.

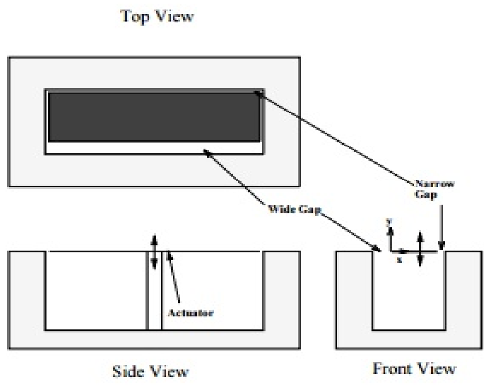

Figure 1.3: Illustration of On demand Vortex Generator [3].

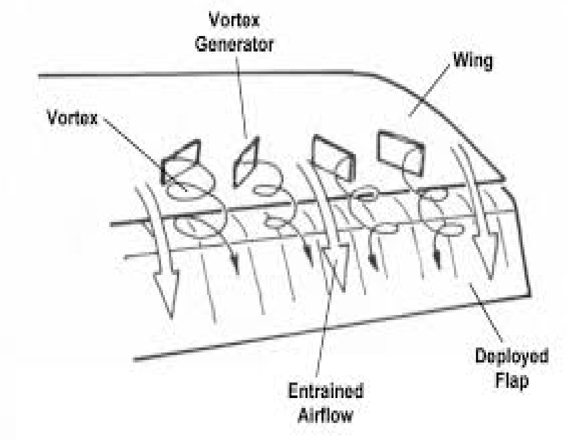

Figure 1.4: Illustration of Vortex generator.

1.3. PROJECT DEFINITION

1.3.1. RESEARCH OBJECTIVE

Recent studies (Lin, 2002; Ashill *et al.*, 2005) have shown that, when using Vortex Generators (VGs) for aerodynamic flow control, it is beneficial to use Sub-Boundary Layer Vortex Generators (SBVGs) rather than conventional Vortex Generators. The two different types of VGs mentioned above, are distinguished based on the height VGs with respect to the boundary layer thickness. The height of conventional VG is comparable to the boundary layer thickness, whereas the height of the SBVG varies between 10% – 50% of the boundary layer thickness. Due to the reduced height, the vortices induced by SBVGs are substantially weaker. As a result, use of SBVGs is limited to scenarios where the regions of flow separation are relatively-fixed or well defined. Therefore, it is necessary to understand better, the flow-field induced by SBVGs, to be able to adequately predict and extend the use SBVGs for flow control over a wide range of conditions. To this end, as a preliminary study, the primary objective of this thesis can be stated as follows:

Objective: Simulate the flow-field induced by the SBVGs in a laminar boundary layer with different profile/shape, to characterise and compare their properties with an emphasis on questions:

- What are the general properties of the flow-field induced by SBVGs?
- How does the VG profile influence the induced flow-field?
- What is the influence of the induced vortices on the downstream development of the boundary layer?
- What are the characteristics of unsteady nature of the induced vortices?
- What is the contribution of SBVGs to far-field noise?

The primary motivation to use a laminar boundary layer for the current thesis stems from the fact that, most of the available literature on VGs have predominantly considered a turbulent inflow condition for analysis. As a result, laminar inflow conditions by and large have been neglected. Study on wake characteristics of vane-type VG in a flat plate by Shim *et al.* (2015) is one of the very few studies considering a laminar boundary layer. Moreover, with VGs being considered in the design phase of a wind turbine blade, it is necessary to look into the behaviour of induced flow-field in these conditions as well.

1.3.2. DOCUMENT OUTLINE

The overall structure of this thesis constitutes of six chapters. Chapter-1 introduces the need for flow control and some of the commonly used techniques in flow control. In Chapter-2 some of the fundamental aspects of boundary layer and aeroacoustics are discussed. Following this, in Chapter-3 an in-depth review of available literature on the properties of flow-field induced by vortex generators is presented. Chapter-4 highlights the methodology used in the current study. First, a brief description of the numerical simulation and setup is given. Following this different test cases, and finally, a review of the different vortex identification techniques leading up to a modified criteria is described. Chapter-5 is dedicated to analyses of the results of various simulations. Initially, a comparison of the flow-field induced by two different sub-boundary layer vortex generator profile is made. Following this, the influence of the change in angle of attack of the vortex generator vane for the same is presented. Finally, in Chapter-6 the conclusion gives a summary of the significant findings and in the recommendation areas of further research is identified.

2

BACKGROUND

This chapter consists of two main sections, one containing a brief overview of the boundary layer parameters and the other dedicated to the introduction of aeroacoustics. First in Section 2.1, some of the essential boundary layer parameters required for the describing results in Chapter 5 are discussed. This is followed by an overview of the properties of the boundary layer. In Section 2.2, aeroacoustics and mechanisms of aerodynamic noise are introduced, leading up to a discussion on noise prediction techniques.

2.1. BOUNDARY LAYER PARAMETERS

For the flow around a body immersed in a viscous medium, there is a region just adjacent to the surface where the viscous effects are predominantly important. This region is referred to as the boundary layer. As a result of the viscosity, the velocity at the surface is zero. This is also referred to as the no-slip condition. As we move away from the surface, in the wall normal direction, the velocity increases until it reaches the freestream value. A schematic representation of the development of boundary layer on the surface of the flat plate is in Figure 2.1.

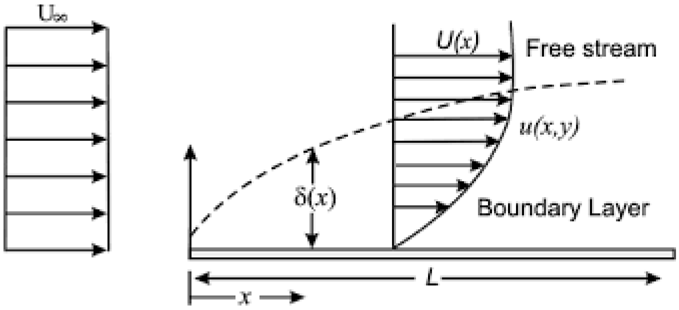

Figure 2.1: Boundary layer development over flate plate [2].

The thickness of the boundary layer (δ) is defined as the height above the surface where the value of the velocity is 99% of the freestream velocity (u_∞). From Figure 2.1 it is seen that δ does not remain constant over the flat plate. Instead, it varies in the streamwise direction and depends on the local velocity profile. In addition to δ some of the other general parameters that are used to characterise the boundary layer are:

- Displacement thickness (δ^*):
  For incompressible flow, δ^* is given by

$$\delta^* = \int_0^\delta (1 - \frac{u}{u_\infty}) dy \tag{2.1}$$

  δ^* can be physically interpreted as the distance from which the streamlines outside the boundary layer are displaced away from the surface when compared to the streamlines of an ideal inviscid case because of the presence of the boundary layer.

- Momentum thickness (θ):
  For incompressible flow, θ is given by

  $$\theta = \int_0^\delta \frac{u}{u_\infty}(1 - \frac{u}{u_\infty})dy \tag{2.2}$$

  Physically θ can be understood as a measure of the additional loss of momentum because of the friction forces when compared to an inviscid flow case. It is nothing but the height of an imaginary stream tube in the inviscid condition carrying momentum equal to that, which would have been lost due to friction in the viscous condition.

- Shape factor (H):
  H is a nondimensional number defined as the ratio of displacement thickness and momentum thickness.

  $$H = \frac{\delta^*}{\theta} \tag{2.3}$$

  Depending on the value of H at a particular location, it is also possible to ascertain if the boundary layer at that point is either laminar, turbulent or separated. For a laminar flow, H varies from around 2 to 3.5, beyond 3.5 it is possible that the flow might have separated White and Corfield (2006). For a turbulent flow H ranges from around 1.3 to 2.5.

One of the most important flow parameters is the Reynolds number (Re). It is a non-dimensional number defined as the ratio of inertial forces to viscous forces. The Re at position x is given by

$$Re_x = \frac{\rho u_\infty x}{\mu} = \frac{u_\infty x}{\nu} \tag{2.4}$$

where ρ is the fluid density, x is the characteristic length scale, μ is the dynamic viscosity, and ν is the kinematic viscosity. In the case of flow over flat plate shown in Figure 2.1 x is the distance from leading edge of the flat plate. Based on Re_x it possible to classify boundary layer into either a Laminar boundary layer or Turbulent boundary layer. A comparison between the laminar and turbulent boundary layer profiles is illustrated in Figure 2.2.

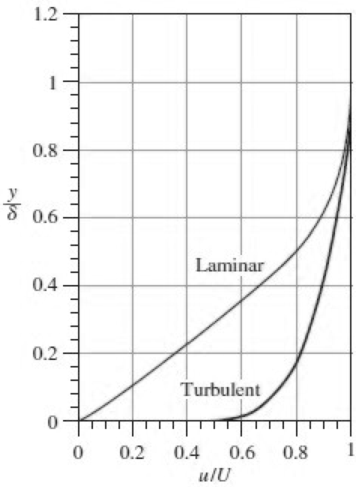

Figure 2.2: Comparison between the Laminar and Turbulent boundary layer [4].

2.1.1. LAMINAR AND TURBULENT BOUNDARY LAYER

The laminar boundary layer is characterised by smooth streamlines originating as a result of fluid moving uniformly in layers without any macroscopic mixing across these layers. At low Re ($Re < Re_{crit}$) flow is considered to be laminar. As evident from Figure 2.1 boundary layer thickness grows as we move downstream from the leading edge of the plate. This is because of the effect of the viscous forces on the consecutive layers of the fluid, which is responsible for decelerating the flow. Thus with a growing boundary layer, the velocity profile varies at each downstream position. Nevertheless, according to White and Corfield (2006), for zero pressure gradient conditions, by selecting a suitable similarity parameter, it is possible to obtain a self-similar solution for the different velocity profile at various downstream positions. This self-similar profile is called Blasius profile, named after H. Blasius who in 1908 first deduced this property. Blasius introduced a nondimensional similarity parameters η given by:

$$\eta = y\sqrt{\frac{U_\infty}{\nu x}} \tag{2.5}$$

The Blasius profile scaled using the similarity parameters is shown in Figure 2.3.

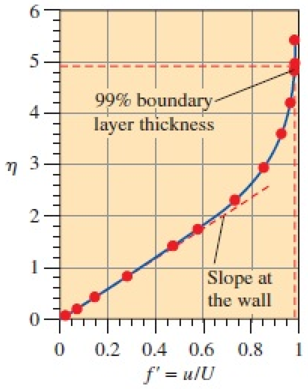

Figure 2.3: Blasius profile for boundary layer on a flate-plate in zero pressure gradient conditions, [4].

As the laminar boundary layer grows, the Reynolds number associated with it also increases. At a certain Reynolds number referred to as the critical Reynolds number (Re_{crit}) the flow transforms from a laminar state to a turbulent state. This transformation is known as flow transition.

The process of transition is a phenomenon involving several stages. The developing laminar boundary layer is subjected to infinitesimally small perturbations which lead to unstable Tollmien-Schlichting (TS) waves. As these TS waves grow, the longitudinally stretched vortices begin to breakdown, resulting in the formation of the turbulent spots in the flow. These turbulent spots further entrain the surrounding fluid to result in a fully turbulent flow. This process is referred to as natural transition and is illustrated in Figure 2.4. Alternately, in the presence of large disturbance in the flow, it is possible to bypasses some of the early stages of natural transition to directly result in the formation of turbulent spots eventually leading to a fully turbulent flow, this process is referred to as bypass transition.

Once the flow transitions from a laminar to a turbulent state, drastic changes in the velocity profile of the flow is observed. In general, the turbulent boundary layer can be described as complex, unsteady and non-uniform. The comparison of the mean velocity profile of the turbulent boundary layer and the velocity profile of the laminar flow is shown in Figure 2.5. It is evident that the turbulent profile in fuller with a steeper gradient close to the wall and a larger boundary layer thickness in comparison to the laminar profile. The mean velocity profile for turbulent flow can non-dimensionalised using u^+ and y^+ given by:

$$\begin{gathered} u^+ = \frac{\overline{u}}{u_\tau}, \quad y^+ = \frac{y u_\tau}{\nu} \\ \text{with, } u_\tau = \sqrt{\frac{\tau_w}{\rho}} \end{gathered} \tag{2.6}$$

where $\overline{u}$ is the mean velocity, u_τ is the wall frictional velocity and τ_w is the wall shear stress. The mean profile in turbulent flow in terms of u^+ and y^+ is shown in Figure 2.6. Unlike the Blasius profile, it not possible to obtain a self-similar single expression for the turbulent mean velocity profile. Instead, the velocity

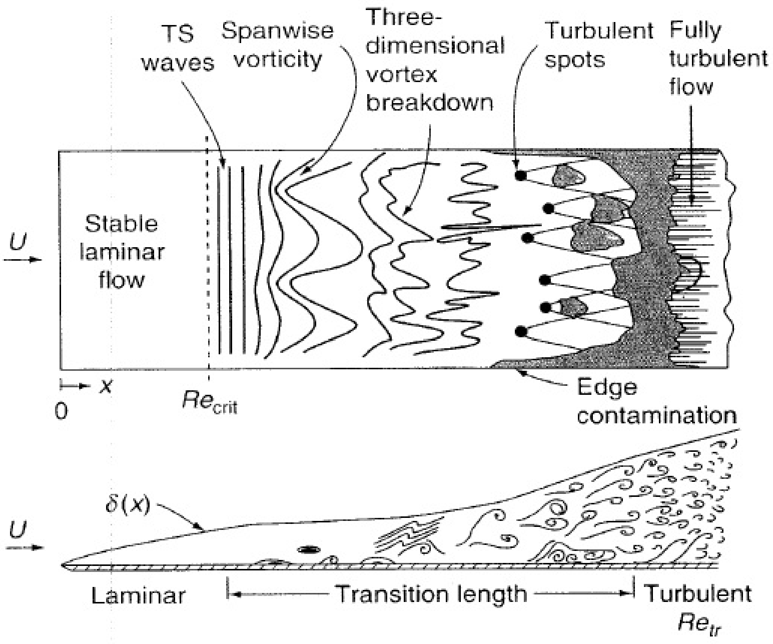
TS waves
Spanwise vorticity
Three-dimensional vortex breakdown
Turbulent spots
Fully turbulent flow
Stable laminar flow
U
x
0
Re_{crit}
Edge contamination
$\delta(x)$
U
Laminar
Transition length
Turbulent
Re_{tr}

Figure 2.4: Idealised sketch of Natural boudary layer transition [2].

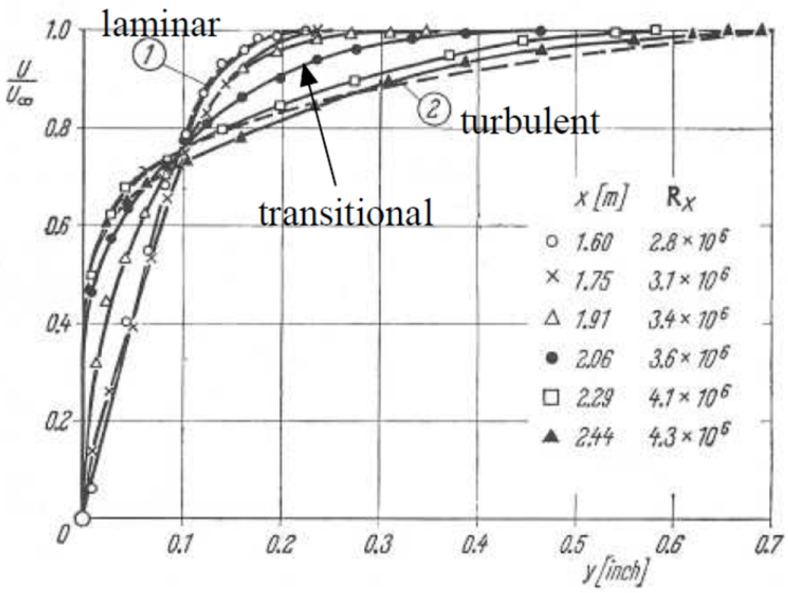

Figure 2.5: Typical laminar, transitional and turbulent boundary layer profiles on flate plate[5].

profile is divided into different regions such as inner and outer with a common overlap region having separate similarity solutions. The inner layer is characterised by dominant viscous stresses. However, in the outer regions, turbulent stresses are more dominate. In the overlap region, both the turbulent and viscous stresses influence the velocity profile. The nondimensional relation's for different regions is given below (White and Corfield, 2006):

$$\text{Inner layer:} \quad u^+ = f(y^+) \tag{2.7}$$

$$\text{Outer layer:} \quad \frac{u_\infty - \overline{u}}{u_\tau} = g(\frac{y}{\delta}, \xi) \quad \text{where,} \quad \xi = \frac{\delta}{\tau_w}\frac{dp_e}{dx} \tag{2.8}$$

$$\text{Overlap layer:} \quad u^+ = f(\frac{\delta u_\tau}{\nu}\frac{y}{\delta}) = \frac{u_\infty}{u_\tau} - g(\frac{y}{\delta}) \tag{2.9}$$

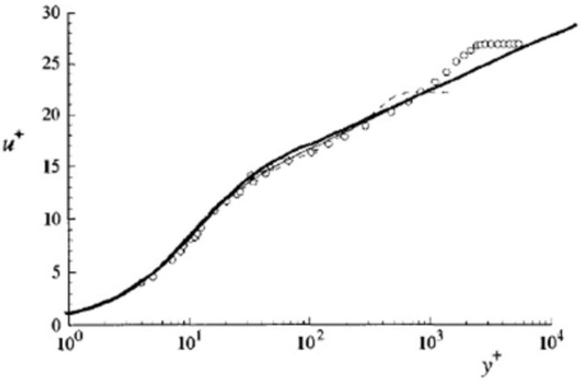

Figure 2.6: Mean velocity profile for turbulent boundary layer in terms of u^+ and y^+. [○] - boundary layer experiments Klebanoff (1954), $Re_\theta = 8000$; [−−] - boundary layer DNS of Spalart (1988), $Re_\theta = 1410$; [−] - van Driest's law of wall [6].

From equation 2.9 using functional analysis, it can be shown that the velocity profile in the overlap region is logarithmic. This is also evident in Figure 2.6 as well, where the mean velocity profile is seen to be linear in the log scaled y^+ between $y^+ = 50$ to 100, which corresponds to the overlap region. Studies on turbulent boundary layers show the presence of densely populated 'hairpin' vortices in the boundary layer (Adrian *et al.*, 2000). These hairpin structures are responsible for the logarithmic profile. Additionally, these structures enhance the momentum transfer between the different layers of boundary layer flow. As a result, the turbulent boundary layer is more energetic (in the regions close to the wall) when compared to the laminar boundary layer.

2.2. AEROACOUSTICS

The study of flow induced noise is known as aeroacoustics. 'It is concerned with the sound generated by turbulent and/or unsteady vortical flows including the effects of any solid boundaries in the flow' (Wang *et al.*, 2006).

A recent study on the visual and acoustic impact of wind farms by van den Berg *et al.* (2008) concluded that the annoying noise generated by the wind turbines is leading to a negative attitude towards them. As a result, governments across the globe have started imposing strict noise regulations (Maris *et al.*, 2007) which require the wind turbines to operate at reduced power in some conditions, for instance, during the night. Thus, there is a need to analyse and mitigate the different noise sources in the wind turbine.

The noise from the wind turbines is broadly classified into:

- Mechanical noise, and
- Aerodynamic noise.

The mechanical noise originates from different mechanical components, such as the generator and the gearbox. Using known engineering solutions such as sound absorption material and others it is possible to reduce mechanical noise. However, the aerodynamically generated noise which radiates from the blades and other external components still poses a formidable challenge.

2.2.1. MECHANISM OF AERODYNAMIC NOISE

For the aerodynamic noise generated by the wind turbines, according to Wagner *et al.* (2012) the different noise mechanisms can be separated into three groups.

First, we have noise generated due to the interaction of the rotating blade with localised flow features such as wake of an upwind wind turbine. This leads to unsteady loading on the blades, which results in noise, generally dominated by frequencies related to the blade passing frequency of the wind turbine rotor.

Second, we have inflow turbulence noise. Here, based on the size of the turbulent eddy in comparison to the chord of the airfoil, it is possible to expect either low-frequency or high-frequency noise. In case of the low-frequency inflow turbulence noise, the size of the eddy is larger than the blade chord. Therefore, the loading on the entire blade is expected to change. This results in radiation of sound whose wavelength is much bigger than the chord of the blade. Under such circumstances, the sound source is considered to be acoustically compact. The intensity of this type noise radiation varies with the sixth power of the Mach number (M^6). For the high-frequency inflow turbulence noise, the size of the eddy is much smaller than the chord of the blade. This leads to localised load fluctuations which are not expected to have a significant impact on the global aerodynamics. The noise radiated from such a source will have a higher frequency and effectively a smaller wavelength when compared to the chord of the blade. Therefore, this type of source is not acoustically compact, and the intensity varies with the fifth power of Mach number (M^5). An illustration of the low-frequency and high-frequency eddies interacting with the airfoil is shown in Figure 2.7. According to Wagner *et al.* (2012) the shape of an airfoil with an emphasis on the leading edge is expected to play a major role in determining the turbulence inflow noise.

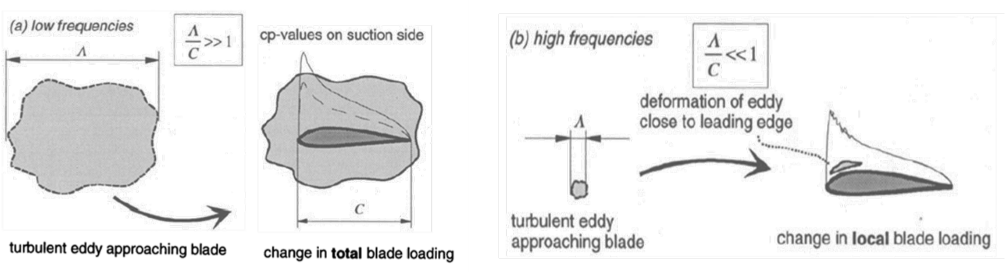
(a) low frequencies
$\frac{\Lambda}{c} >> 1$
Λ
cp-values on suction side
c
turbulent eddy approaching blade
change in **total** blade loading
(b) high frequencies
$\frac{\Lambda}{c} << 1$
deformation of eddy close to leading edge
Λ
turbulent eddy approaching blade
change in **local** blade loading

Figure 2.7: Illustration of intraction of turbulent eddies with airfoil.[7].

Lastly, we have airfoil self-noise due to the interaction of the boundary layer instabilities or turbulence with the airfoil. Airfoil self-noise can be further sub-divided based on the mechanism involved as:

- Laminar boundary layer instability noise
- Turbulent boundary layer - Trailing edge noise
- Trailing edge bluntness noise
- Tip noise
- Separated/Stalled flow noise

For low Reynolds number ($Re < 10^6$) flow on the blades of a wind turbine, it is possible to have a laminar boundary layer on either side of the airfoil. Depending on the Re this laminar flow can persist till the trailing edge of the airfoil. As previously discussed, laminar boundary layers are susceptible to instabilities like TS waves. Acoustic waves generated at the trailing edge of the airfoil can travel upstream to amplify these instabilities which can lead to flow separation or upstream transition of flow. This kind of feedback mechanism according to Wagner *et al.* (2012) results in a tonal (periodic) noise and is called laminar boundary layer instability noise. An illustration of this mechanism is shown in Figure 2.8.

The turbulent eddies in the boundary layer of an airfoil are known to be an inefficient source of sound. However, at shape edges such as trailing edge of an airfoil, there is a sudden change in the boundary conditions coupled with the interactions of eddies from both the suction and pressure sides of the airfoil. Under

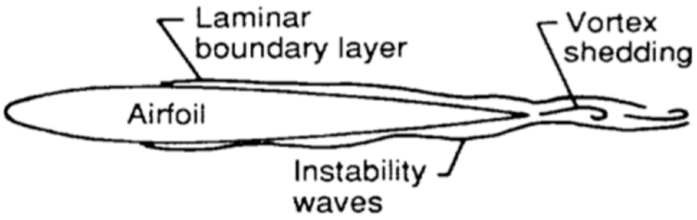

Figure 2.8: Illustration of mechanism of laminar boundary layer instability noise.[8].

these conditions, the eddies become a more efficient source of sound (van der Velden, 2017). This type of sound is broadband (non-periodic) in nature and is referred to as the turbulent boundary layer - trailing edge noise. An illustration of this mechanism is shown in Figure 2.9.

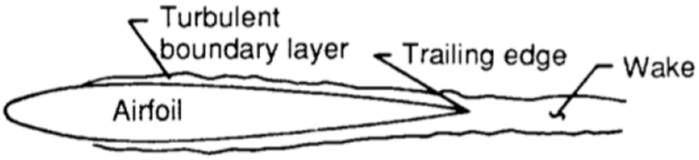

Figure 2.9: Illustration of mechanism of Tubulent boundary layer trailing edge noise.[8].

For blunt airfoils, with an increase in the ratio of the trailing edge thickness (t^*) to the displacement thickness (δ^*) beyond a certain critical value, an additional tonal (periodic) source of sound is observed at the trailing edge (Blake, 1986). This is because, with an increase in t^*, alternating vortices resembling a von Karman sheet is shed from the trailing edge of the airfoil. This periodic shedding results in a periodic pressure fluctuation, generating a tonal sound. This is known as trailing edge bluntness noise and an illustration of this mechanism is shown in Figure 2.10.

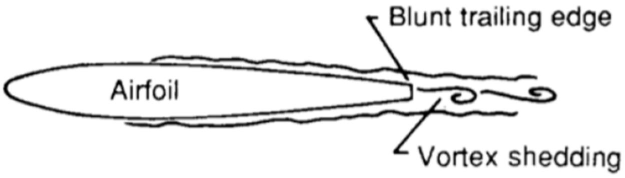

Figure 2.10: Illustration of mechanism of Trailing edge bluntness noise.[8].

The pressure difference between the two sides of an airfoil at the tip of the blade results in generating the tip vortex. The interaction of the so formed tip vortex with the trailing edge of the airfoil, similar to the interaction of turbulent eddies, is said to a source of sound (Brooks and Marcolini, 1986). This is known as tip noise and is said to have a broadband nature (Jianu *et al.*, 2012). An illustration of the tip noise mechanism is shown in Figure 2.11.

At high angles of attack of the airfoil, the boundary layer on the gets detached from the surface to result in flow separation (discussed in section 1.2). The occurrence of flow separation results in the formation of unsteady structures of different scales depending on the extent of separation. These unsteady structures interact with the trailing edge of the airfoil to result in separation-stall noise. For mildly separated flow, noise is radiated from the trailing edge (Wagner *et al.*, 2012), however at very high angles of attack, large scale structures are shed from the airfoil which increases low-frequency noise (Brooks and Marcolini, 1986). An

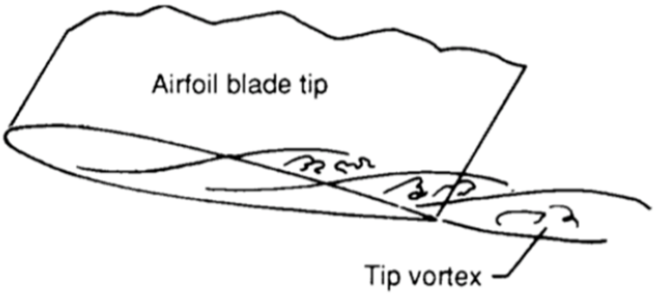

Figure 2.11: Illustration of mechanism of Tip noise.[8].

illustration of the mechanism separation-stall noise is shown in Figure 2.12.

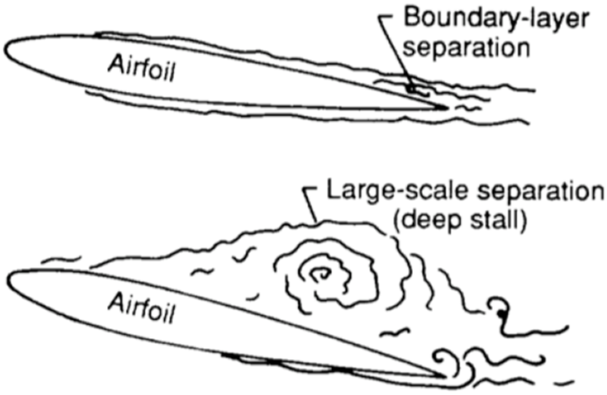
Boundary-layer separation
Airfoil
Large-scale separation (deep stall)
Airfoil

Figure 2.12: Illustration of mechanism of Separation-Stall noise.[8].

2.2.2. NOISE PREDICTION

It is possible to determine the flow generated noise by using either experimental or computational techniques. Using a computational techniques it possible to use either a direct method or a hybrid method.

In the direct method, the sound is computed together with its fluid dynamic source field by solving for the compressible flow equations (Wang *et al.*, 2006). This can be achieved by either using direct numerical simulation (DNS) or large eddy simulation (LES). Since DNS is computationally very expensive, its use is limited to only low or moderate *Re* flows. The use of LES and the influence of subgrid scale models on the computed acoustics is a topic of active research; an overview of this is available in the study on the computational prediction of flow generated sound by Wang *et al.* (2006). Further, using the direct method requires special treatment at the boundary to prevent the influence of the acoustic reflection from the boundaries (Tam, (2004)). Thus, it is both challenging and computationally very expensive to employ the direct method.

In contrast, for the hybrid method, the acoustics is decoupled from the computation of the flow-field. The far-field sound is obtained by additionally post-processing the flow-field using suitable acoustic analogies. This involves the fundamental assumption that there is no acoustic feedback, i.e. generated acoustic waves do not influence the flow-field in any way whatsoever. The decoupling of the acoustics alleviates the need for very a high numerical accuracy, there by making it possible to use lower-resolution schemes (Wang *et al.*, 2006).

In the current thesis, the hybrid approach is used. This is selected based on the computational effect needed and the simplicity of the hybrid method. Moreover, the test cases in the current thesis involve low Mach numbers, where the difference in the length scales between the hydrodynamic and acoustic quantities is large. Therefore, use of the direct method is more complicated. Some of the necessary acoustic analogies for the hybrid method are discussed below

Lighthill's Analogy

Consider a generic vector, q comprising of the velocity and thermodynamic quantities sufficient to uniquely define the flow-field. This satisfies the Naiver-Stokes equations as:

$$N(q) = 0 \tag{2.10}$$

Equation 2.10 can be re-arranged to form an acoustic analogy (Wang *et al.*, 2006) as:

$$Lq = S(q) \tag{2.11}$$

where, L is the linear wave propagation operator $(\frac{\partial^2}{\partial t^2} - c_0^2\frac{\partial^2}{\partial x_i \partial x_j})$ and $S(q)$ is the non-linear sound source, which is assumed to act analogous to an externally applied source. This $L-S$ decomposition is referred to as the Lighthill's analogy. For an arbitrary source region surrounded by a unbounded quiescent fluid we have:

$$\frac{\partial^2 \rho'}{\partial t^2} - c_0^2 \frac{\partial^2 \rho'}{\partial x_i \partial x_j} = \frac{\partial^2 T_{ij}}{\partial x_i \partial x_j} \quad \text{with,} \quad T_{ij} = \rho u_i u_j + (p' - c_0^2 \rho')\delta_{ij} - \tau_{ij} \tag{2.12}$$

where, c_0 is the reference speed of the sound, $\rho' = \rho - \rho_0$ is the density fluctuations and T_{ij} is the source term also called as the Lighthill stress tensor. The first term, $\rho u_i u_j$ in this tensor corresponds to Reynolds stresses. The second term, $(p' - c_0^2\rho')\delta_{ij}$ represent the departure from a state where all the changes are isentropic. Lastly, the third term in the tensor corresponds to the viscous stresses. For low Mach number, high Reynolds number flows, the change in entropy term and the viscous stresses can be neglected, therefore $T_{ij} \approx \rho u_i u_j$ and equation 2.12 reduces to:

$$\frac{\partial^2 \rho'}{\partial t^2} - c_0^2 \frac{\partial^2 \rho'}{\partial x_i \partial x_j} \approx \frac{\partial^2 (\rho u_i u_j)}{\partial x_i \partial x_j} \tag{2.13}$$

Wagner *et al.* (2012) points out that an important conclusion from Lighthill's theory is that, *’it allows to compute the sound field radiated by a bounded region of fluctuating (turbulent) flow by solving an analogous problem of forced oscillation, provided that the flow is known’*. In the above equation, the source term on the right-hand side involves a double spatial derivative. This implies that the source either has a four lobed quadrupole or a two lobed dipole directivity pattern, depending on whether the spatial derivatives are in the different direction or same direction, respectively.

Ffowcs Williams-Hawkings Analogy

The application of Lighthill's theory is restricted to only unbounded flow. Thus, the presence and influence of solid surface on the radiated sound is neglected. Curle (1955), to overcome this shortcoming implemented an extension of the Lighthill's theory where the influence of the static solid surfaces is also considered. Williams and Hawkings (1969) further improved upon the Curle's extension to include the influence of the arbitrary motion of solid surfaces. This is also referred to as the Ffowcs Williams-Hawkings (FWH) analogy. In FWH analogy, the domain is divided into regions of interior flow and exterior flow, with respect to the surface which bounds solid body. To this end, a function $f(x,t)$ depicting the shape of the solid and its motion, such that $f(x,t) = 0$ at the surface, is considered. An illustration of the this bifurcation and $f(x,t)$ is shown in Figure 2.13.

The resulting FWH equation obtained by rearranging the generalised Naiver-Stokes equations is as below:

$$\frac{\partial^2 \rho'}{\partial t^2} - c_0^2 \frac{\partial^2 \rho'}{\partial x_i \partial x_j} = \frac{\partial^2 T_{ij}}{\partial x_i \partial x_j} - \frac{\partial}{\partial x_i}(P_{ij}\delta(f)\frac{\partial f}{\partial x_j}) + \frac{\partial}{\partial t}(\rho_0 u_i \delta(f) \frac{\partial f}{\partial x_i}) \tag{2.14}$$

where T_{ij} is the Lighthill's stress tensor, similar to equation 2.12. In addition to the Lighthill's tensor in equation 2.14 two additional source terms are present. The second term on the right-hand side of the equation 2.14 contains a spatial derivative, indicating a two lobed dipole source. This dipole source is seen to be proportional to the component of the stress tensor P_{ij} consisting of both the normal and viscous stresses in the direction of the wall-normal at the surface of the solid given by $\frac{\partial f}{\partial x_j}$. This corresponds to the force excreted

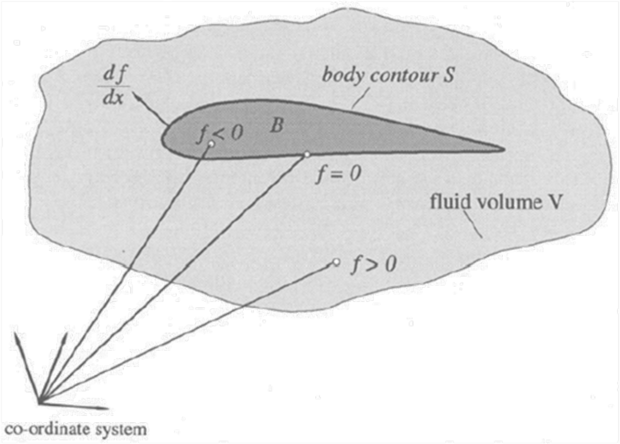

Figure 2.13: Illustration of $f(x,t)$ in a domain with a solid body [7].

by the body on the fluid and is also commonly referred to as loading noise. The third term on the right-hand side of the equation 2.14 contains a time derivative, indicating an omnidirectional monopole source. This monopole source is seen to be proportional to the local acceleration of the surface in the wall-normal direction. This monopole source is commonly referred to as thickness noise. Based on this, Wagner *et al.* (2012) points out that '*solid surfaces are acoustically equivalent to a surface distribution of monopoles and dipoles, with the respective strength being equal to the local acceleration of the surface and the net force exerted onto the fluid*'.

Farassat (1981) deduced the general solution for the monopole and dipole sources in the FWH equation. For the thickness noise, in Wagner *et al.* (2012) solution is expressed as:

$$4\pi p'(x,t) = \frac{\partial}{\partial t}\int_S \frac{\rho_0 u_n}{r(1-M_r)} ds(y) \tag{2.15}$$

Similarly, the solution for loading noise is expressed as:

$$4\pi p'(x,t) = \frac{\partial}{\partial x_i}\int_S \frac{P_{ij} n_j}{r(1-M_r)} ds(y) \tag{2.16}$$

where, u_n is the velocity of the surface in the normal direction to the surface, $P_{ij} n_j$ is the force per unit area exerted by the surface on the fluid and M_r is relative Mach number in source region y. M_r is defined as the ratio of the component of source velocity in the direction of the observer x with the reference speed of sound (c_0).

3

VORTEX GENERATOR FLOW

Vortex Generators (VGs) are devices which induce a swirling flow, and as stated earlier, is widely used as a passive flow control device. This swirling flow produced by VGs results in streamwise vortices which re-energises the boundary layer by redistributing the momentum. Consequently, this additional energy in the lower layer of the boundary layer enables the fluid particles close to the wall to overcome the resistive forces. For example in case of an airfoil, on the suction side, the resistive forces mainly constitutes of the frictional force and force due to the adverse pressure gradient. In the following sections, the state-of-the-art on the flow-field induced by VGs will be described.

3.1. VORTEX GENERATOR CONFIGURATION

VGs were first introduced by Taylor (1947) to eliminate the occurrence of flow separation in diffusers. Ever since, there have been numerous studies on VGs proving their effectiveness in preventing or delaying separation (Ashill *et al.*, 2005; Lin, 2002). Over the years different VG profile has been utilised and studied, some of the more commonly employed profiles are as depicted in Figure 3.1.

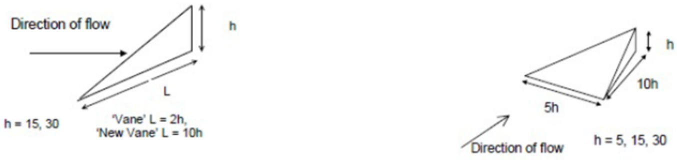

(a) Triangular vane

(b) Forward wedge

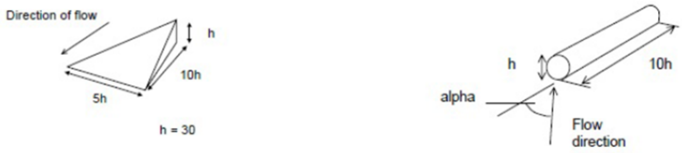

(c) Backward Wedge

(d) Dowel

Figure 3.1: Illustration of some of the commonly used differnt VG profiles [9].

VG's are generally characterised based on their height, traditionally the height of VGs have been comparable to the order of magnitude of the boundary layer thickness. Such VG's are referred to as conventional VG's. However, in an attempt to lower the drag penalty of the VGs studies from Lin *et al.* (1990) has shown that, it is more efficient to use VGs smaller than the thickness of boundary layer. These smaller VGs are called as Micro or Sub Boundary Layer VGs (SBVGs). The height of SBVGs varies between 0.1 to 0.5 times the boundary layer thickness. The primary difference between the SBVGs and the conventional VGs is the fact that vortices induced from SBVGs is completely submerged inside the boundary layer. In an investigation of longitudinal vortices in turbulent boundary layer, Mehta and Bradshaw (1988) points out that, for conventional VGs, the induced vortices are displaced by as much as two times the boundary layer thickness in the wall normal direction. In applications where the separation line is fairly consistent, studies following from the initial separation control study by Rao and Kariya (1988) have shown that it could be advantageous to use SBVGs because of the much lower device drag and the localized flow control provided by SBVGs (Lin, 2002). On the other hand, SBVGs are more sensitive to placement, as previously indicated, making it necessary to understand better the downstream development of the induced vortices. This is so because, it will enable the use of SBVGs more effectively for a wide variety of flow conditions. Thus in the the present study, only SBVGs have been considered. Henceforth in this report, SBVGs will be refereed to as only VGs unless explicitly stated as otherwise.

By arranging the VGs in an array of VG pairs it is possible generate either co-rotating or counter-rotating vortex pairs. In the co-rotating configuration both the vortices from a VG pair will be rotating in the same direction i.e. either clockwise or counter-clockwise. In the counter-rotating configuration the vortices from the VG pair are rotating in opposite direction with respect to each other i.e one clockwise and the other counter-clockwise. Further, in this configuration it possible to have either a common up-wash or a common down-wash setup. Up-wash or down-wash indicates the direction of the mean induced flow in-between the two vortices. Figure 3.2 illustrates some of the different configurations. For both the conventional VGs and SBVGs studies have shown that counter-rotating setup is more benificial than co-rotating setup (Wendt and Biesiadny, 2001; Godard and Stanislas, 2006). However, this observation can't be generalised for all applications. For example, in case of the VGs employed on swept wings, Lin (2002) points out that a co-rotating setup is more efficient. For the current study, based on the fact that, on wind turbine blades counter - rotating common down-wash setup is widely employed, only this setup has been chosen for the analysis.

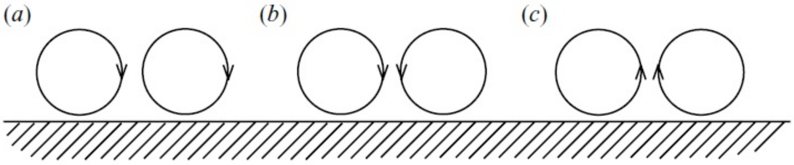

Figure 3.2: Different configuration of induced vortices. (a) Co-rotating (b) Counter-rotating, common down-wash (c) Counter-rotating, common up-wash.

3.2. INDUCED FLOW FIELD

Having discussed the different VG configuration so far, it is now necessary to discuss the properties of the flow field induced by the vortex generators. In the flow-field measurements of a device induced stream-wise vortex, Yao *et al.* (2002) notes that the characteristic of the induced vortex is 'broadly similar' for both conventional VGs and SBVGs. Therefore, literature from both conventional and SBVGs has been used to describe the induced flow field.

In studies involving VGs, predominantly the properties of induced vortices of interest, in the averaged flow field are:

- Strength of the induced vortex, Γ.
- Downstream evolution of the induced vortex.

In the study of initial circulation and peak vorticity by Wendt and Biesiadny (2001), it is emphasized that strength of the induced vortex observed in the averaged flow field is influenced by parameters such as freestream velocity (U_∞), angle of attack of the VG vane (β) and ratio of the height of VG vane to the boundary layer thickness ($\frac{h}{\delta}$). Angele and Grewe (2007), further highlights that the initial strength of the induced vortex is linked to the freestream velocity as a function of the velocity at the tip of VG vane. Similarly, Velte *et al.* (2014) looked at the influence of the VG vane shape on the strength of the induced vortex by comparing rectangular VG vane, triangular VG vane and cambered VG vane. The results from this study points out the difference in the strength of the vortex observed in averaged field, with rectangular VG vane inducing the strongest vortex.

Thus, shape of the VG vane is also an influencing factor in induced flow field. Collectively, these studies outline the critical parameters which influence the strength of the induced vortex.

With respect to the downstream evolution of the induced vortex observed in a time averaged field, Lögdberg *et al.* (2009) based on the identified vortex centres using Q-criteria (see Section 4.4.3), showed that, in a wall-normal streamwise plane, vortices initially close to the VG vane approach the wall. However, further downstream the vortices move away from the wall. Similarly, in the spanwise-streamwise plane the observed vortices start to move away from each other in the spanwise direction in the region close to the VG vanes, to finally asymptote to a balanced position. These observation are similar to results from various other studies on flow field induced by vortex generators as indicated in the review articles of Ashill *et al.* (2005) and Lin (2002). Additionally, in the study of Lögdberg *et al.* (2009) it is also noted that the divergence of the observed vortices in the spanwise plane is a function of the induced vortex strength, with the divergence increasing as the vortex strength increases. It is to be noted that the above described vortex behaviour corresponds to the counter-rotating common-down flow configuration shown in Figure 3.2.

In terms of the vortex size and vortex decay, Lögdberg *et al.* (2009) showed that, as we move downstream from the VG vanes the size of vortex increases but the strength decays rapidly. The observed rate of decay is found to be maximum close to the VG vanes. In view of all that has been mentioned so far, one may state that the initial strength of the vortex is dictated by the physical parameters of the VG vane where as the downstream evaluation is linked the vortex wall interactions.

In a recent parametric investigation of the regimes of flow past a VG by Velte *et al.* (2012) it is noted that, in addition to clockwise and counter-clockwise vortices discussed above, it is possible to have additional vortex structures in the flow field. It is important to note that in Velte *et al.* it is stated that the presence additional vortices (secondary vortices) is highly dependent on the prevalent flow condition and is not a consistent feature of the flow field. A schematic representation of one of the observed flow configurations induced by a single VG vane, consisting of a primary counter-clockwise vortex (P) and two additional secondary vortices (H_S, H_P) is as shown in Figure 3.3a. In Figure 3.3b, a map of the the various vortex structures observed as a function of $\frac{h}{\delta}$ and angle of attack of the VG vane (β) from Velte *et al.* is shown.

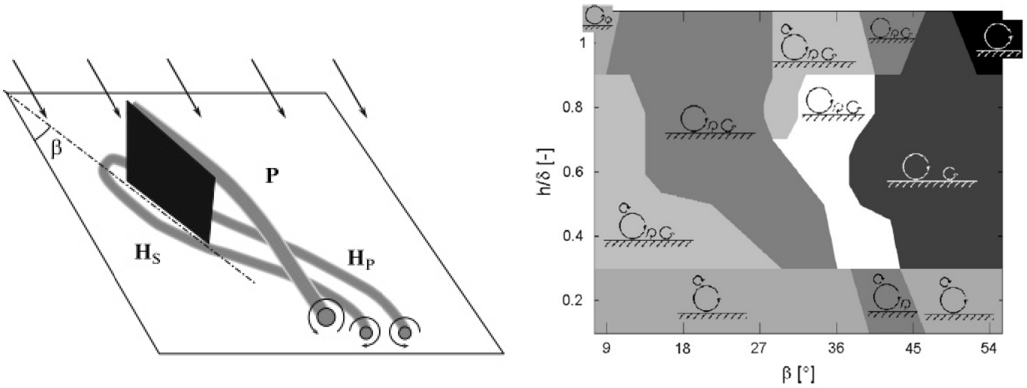

(a) Illustration of Primary(P) and Secondary vortices (H_S, H_P)

(b) Vortex configurations as a function of $\frac{h}{\delta}$ and β

Figure 3.3: Map of different possible vortex configuration [37].

In the above discussed flow field properties it can be noted that, the unsteady or non-stationary nature of the induced vortices has not been explicitly addressed. In the investigation of instatntaneous behaviour of streamwise vortices in a turbulent boundary layer by Angele and Grewe (2007), it is clearly evident that the vortices are not stationary. The instantaneous vortex centres positions identified and integrating in time to arrive at a probability density function (PDF), describing the most likely position of the vortex at any given time from Angele and Grewe is shown in Figure 3.4. Similarly, in the experimental investigation of the flow structure behind the VGs embedded in a decelerating turbulent boundary layer, Cathalifaud *et al.* (2009) presented a mean indicative function of the vortices as shown in Figure 3.5. This mean indicative function, according to the authors can be considered as a spatial probability function of identifying a vortex. This was computed based on the loci of vortex centres identified from instantaneous PIV data. This which further illustrates the unsteady nature of the vortices and thus it is essential to take into account this unsteady nature of the vortices when evaluating the properties of the flow field induced by the VG vanes. As seen in Figure 3.4, the unsteady nature of the vortices is visible in the form of lateral and wall-normal displacement of the vortex about the mean vortex centre. This unsteady behaviour is generally referred to as vortex wandering or vortex meandering. The source of this unsteady meandering is still not very clear and this is a topic that is being actively researched.

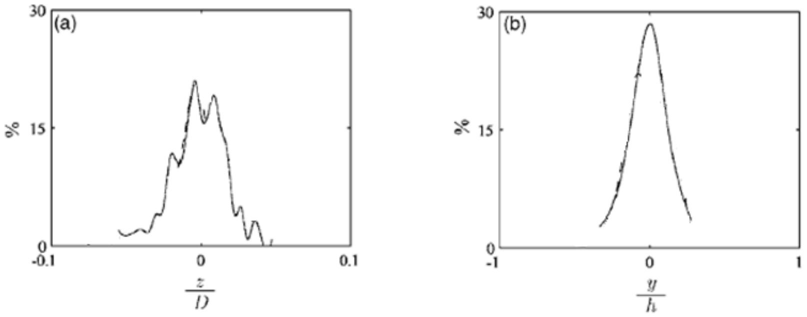

Figure 3.4: (a) Spanwise PDF of vortex centre position (b) Wall-normal PDF of vortex centre position. At $\frac{x}{h}$ = 5.5. [10].

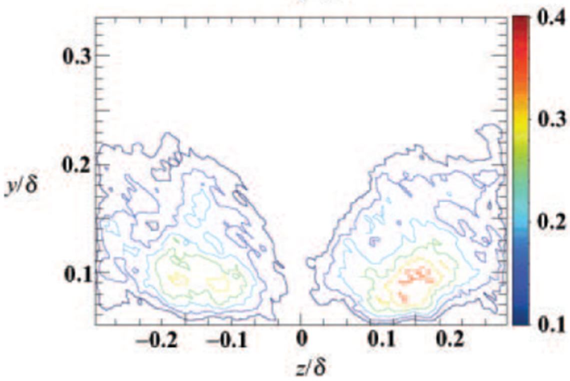

Figure 3.5: Mean indicative function for counter-rotating VG arrangement.[11].

The occurrence of this unsteady meandering in vortices is not just limited to the embedded vortices as in the case of the VG induced flow, but can also observed in the tip vortices being shed from the aircraft wing. In fact, much of the available literature on this topic has been focused on studies relating to the occurrence of meandering in wing tip vortices or free vortices. Studies by Devenport *et al.* (1996), Jacquin *et al.* (2003), and Jacquin *et al.* (2005) provides a good overview of the complex nature of vortex meandering. Some of the possible sources as suggested in study of instability and unsteadiness of aircraft wake vortices by Jacquin *et al.* (2003) include:

- Excitation of vortex core by background turbulence.
- Co-operative instabilities.
- Viscous core instabilities.

For vortices embedded in the boundary layer, as in the case of VG induced flow, in addition to above mentioned factors, it can be hypothesised that the shearing nature of the boundary layer profile, can also influence the meandering. This has been considered based on the study of excitation of vortex meandering in shear flow by Schröttle *et al.* (2015). Further, the presence of additional flow structures, as previously discussed, can also influence the meandering in the primary vortices. In this regard, the experimental study on the instability in secondary vortices in ground effect by Harris and Williamson (2012) points out that the weaker secondary vortices are susceptible to co-operative instabilities. In return, it is possible to consider that these secondary vortices can perturb or induce instability in the primary structures. However, it is important to note that, in the experiments of Harris and Williamson (2012) the vortex system considered did not involve any axial flow unlike the vortices induced by VGs. Thus, it is not appropriate to draw a direct analogy, but has been presented here to highlight the fact that, the presence of secondary vortices could also influence the primary vortices.

By drawing on the concept of meandering, Gardarin *et al.* (2008) in the study of flow separation control with vortex generators, indicated the presence of co-operative instabilities as a dominant source of vortex meandering. These co-operative instabilities, according to Gardarin *et al.* (2008) are triggered due to the excitation of the unstable wavelength by the freestream turbulence entrapped in the vortex core during its formation. Further, in this study it is also hypothesised that these instability mechanisms are responsible for determining the vortex lifetime as well. Thus based this hypothesis, it can be said that the efficiency of the VGs to either prevent or delay separation depends on the susceptibility of the vortices to instabilities.

The studies discussed thus far, outline the general properties of the flow field induced by the VGs. The key observation being that the induced vortices are unsteady in nature. One can think of two possible effects of this unsteady behaviour: unsteady vortices, further enhances the mixing in the boundary layer when comped to steady vortices. This can help to eliminate the regions of local recirculation zones, thereby improving aerodynamic flow control. Contrary to this, in the presence of instabilities leading upto unsteady behaviour, results in enhanced destruction of the vortices. Therefore, the influence of these vortices in the streamwise direction will be short-lived. This is clearly not desirable for aerodynamic flow control.

VGs in addition to helping in flow separation control, also eliminate or reduce the stall-separation noise. However, if the VGs are not effectively positioned to achieve the desired flow control, the additional unsteady flow induced, can also be a source of sound. Going back to the acoustics in Section 2.2, from the perspective of VGs as source of sound, the loading noise most likely expected to dominate.

4

METHODOLOGY

In this chapter, details regarding the numerical simulation and vortex identification are discussed. First, an overview numerical approach is described in section 4.1. Following this, in section 4.2 the test case setup, explaining the vortex generator configuration and computational setup is described. The grid refinement study used to select the optimal grid is presented in section 4.3. Finally, section 4.4 discusses some of the commonly used vortex identification techniques followed by details of the selected method to identify vortex centre.

4.1. NUMERICAL SIMULATION

The advent of experimental techniques such as Particle Image Velocimetry (PIV) has highlighted to a greater extent the nature of the flow-field induced by Vortex Generators (VGs)(Angele and Grewe, (2007); Yao *et al.*, (2002)). This technique has enabled us to capture instantaneous data in a plane or in a volume which was earlier not possible using single point measurement methods such as hot wire anemometry. Nevertheless, the main draw back this technique is that it requires a rather elaborate setup with strict optical access requirement. Alternately, in the current thesis, a computational approach is used to study the flow-field induced by the VGs.

4.1.1. FLOW FIELD SIMULATION

For the current study, a lattice Boltzmann method (LBM) is used to simulate the flow physics. Unlike the traditional Naiver-Stokes based solvers, it involves solving the fundamental kinetic theory using the discrete Boltzmann equation in order to determine the macroscopic fluid dynamics. To this end, PowerFLOW 5.3b a commercial LBM solver is used. In general,the Lattice Boltzmann equations are used to describe the evolution of density distribution function in time. Given a particle density distribution function f_i, which describes the probability of presence of a particle at a position x with a discrete velocity c_i in the direction i at particular time t, the discrete Lattice - Boltzmann equation using explicit time-stepping and a collision operator can be written as:

$$f_i(x + c_i \Delta t, t + \Delta t) - f_i(x, t) = \Omega_i(x, t) \tag{4.1}$$

where, Ω_i is the collision operator. Over the years numerous models have been developed to predict the collision operator, however in LBM one of the simplest and most widely used model developed by Bhatnagar, Gross and Krook (BGK) is adopted (Bhatnagar *et al.*, 1954). Ω_i in BGK form is given as:

$$\Omega_i = -\frac{\Delta t}{\tau}(f_i(x, t) - f_i^{eq}(x, t)) \tag{4.2}$$

where, f^{eq} is the local Maxwell-Boltzmann equilibrium distribution function and τ is the relaxation time parameter. The equilibrium distribution relates the LBM quantities to fluid properties. The second order expansion of the equilibrium functions valid for small Mach number is given by (Chen and Doolen, 1998):

$$f_i^{eq} = \rho w_i (1 + \frac{c_i u}{a_s^2} + \frac{(c_i u)^2}{2a_s^4} + \frac{|u|^2}{2a_s^2}) \tag{4.3}$$

where, w_i is the weight function related to velocity discretization and a_s is the non-dimensional speed of sound. The density (ρ) and velocity (u) of the macroscopic fluid which is computed by summing the discrete density distribution functions as:

$$\rho(x,t) = \sum_i f_i(x,t) \tag{4.4}$$

$$\rho u(x,t) = \sum_i c_i f_i(x,t) \tag{4.5}$$

In PowerFLOW the domain is constructed as a Cartesian grid made up of number of cubic cells known as lattice. In each lattice a D3Q19 discretization considering 19 possible directions in which particle distribution can move to the neighbouring lattice as illustrated in Figure 4.1 is considered. At the boundaries, typically a bounce back condition is implement to replicate the no-slip condition. Further in PowerFLOW, it is possible to use various resolutions in the grid sizes, however the change in grid size between two adjacent lattice/cells is restricted to a factor of two. The solution is advanced in time using an explicit time stepping scheme which is characteristic of LBM and the time-step is determined based on the characteristic velocity in the domain and the smallest lattice/cell size.

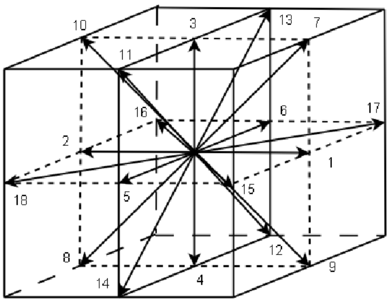

Figure 4.1: Illustration of the D3Q19 model.

Since computationally, it is too expensive to resolve all the different scales in the domain, the standard sub-grid scale model available in PowerFLOW is utilized. This model is a modified version of the two equation RNG k - ϵ model (Yakhot and Orszag, 1986). In PowerFLOW this model has been adapted such that modelled turbulence is accordingly reduced in the presence of grid resolved vortical structures (Casalino *et al.*, 2014). Further, for high Re wall bound flows, resolving the boundary layer down to the viscous sublayer can be very expensive. Therefore, PowerFLOW provides a hybrid a wall shear stress-model based on generalised law of the wall (Launder and Spalding, 1974) given by

$$u^+ = f(\frac{y^+}{A}) = \frac{1}{k} ln(\frac{y^+}{A} + B) \tag{4.6}$$

$$A = 1 + f(\frac{dp}{dx}) \tag{4.7}$$

This equation is iteratively solved to provide a good estimate of the wall shear-stress in the lattice/cell closest to the wall. The so determined local skin friction in then realised using the surface collision process.

4.1.2. ACOUSTIC RADIATION PREDICTION

In order to determine the far-field acoustics PowerACOUSTICS 4.0a, a post processing tool which can be used to analyse the time-dependent data from the solver, PowerFLOW is employed. In PowerACOUSTICS, the far-field acoustics data is recovered based on the formulation 1A developed by Farassat and Succi (1980) for the FWH equation 2.14. This is achieved by using a source-time dominant algorithm in the time domain proposed by Casalino (2003) also refereed to as the advanced time approach. The advanced time approach in principle reinterprets of the retarded time solutions of Farassat (1981) for the FWH equation 2.14 with the point of view of the source, rather than the listener, as initially proposed by Farassat. The comprehensive description of the advanced time approach including the key differences when compared to the retarded time solution is avalable in the work of Casalino (2003).

In the current thesis, since the sources of interest (VGs) are stationary, the loading noise remains as the only source of noise from the analogy. As input to the PowerACOUSTICS far-field noise computation module, the time varying surface pressure data is utilised. Under such circumstance, van der Velden *et al.* (2016) points out that the integral solutions for the current analogy can be expressed as:

$$4\pi p'(x,t) = \frac{1}{c_0}\int_{f=0}\left[\frac{\dot{L}_i\hat{r}_i}{r(1-M_i\hat{r}_i)^2}\right]_{ret} dS + \int_{f=0}\left[\frac{L_i\hat{r}_i - L_iM_i}{r^2(1-M_i\hat{r}_i)^2}\right]_{ret} dS + \int_{f=0}\left[\frac{L_i\hat{r}_i(M_i\hat{r}_i - M^2)}{r^2(1-M_i\hat{r}_i)^3}\right]_{ret} dS \quad (4.8)$$

where, L_i the fluctuating pressure force on the surface of VGs, $\dot{L}_i$ is the time derivative of the fluctuating pressure pressure force on the surface of VGs, r is the effective acoustic distance, computed considering the time delay between the emission of sound from source at location x to the reception of that sound at the listener located at y:

$$r = \frac{-M_0(x_1-y_1)+r^\star}{\beta^2} \quad \text{with,} \quad r^\star = \sqrt{(x_1-y_1)^2+\beta^2[(x_2-y_2)^2+(x_3-y_3)^2]} \quad (4.9)$$

with $\beta = \sqrt{1-M_0^2}$. $\hat{r}_i$ is the unit radiation vector given by:

$$\hat{r}_i = \left[\frac{-M_0r^\star+(x_1-y_1)}{\beta^2 r}, \frac{x_2-y_2}{r}, \frac{x_3-y_3}{r}\right] \quad (4.10)$$

and, $[...]_{ret}$ implies that the solution is evaluated based on the emission time and the effective acoustic distance.

The so computed result from PowerACOUSTICS generates a measurement file containing the time history of the acoustic pressure at the desired listener locations. This output file can be further processed to generate the required results.

Returning briefly to the discussion on LBM, some of appealing features which makes its use attractive are:

- In LBM, pressure is computed using the ideal gas equation. This is seen to computationally more cost effective, when compared to solving the Poisson equation, in Naiver-Stokes based solvers (Jahanshaloo *et al.*, 2013).
- Using LBM, according to Succi (2001) presents a 'much gain no pain' opportunity on parallel computers. This is so, because the LBM algorithm makes it easy to subdivide the domain and execute on different processors. In Succi (2001), it is noted that, LBM achieves a linear speed-up on increasing the number of processors on all grids expect the smaller ones.
- Another highlight of LBM is that, it is easy set up cases, even with complex geometries (Succi, 2011).

4.2. TEST CASES

To achieve the research objectives defined in Section 1.3.1, two different profile of VG vanes: Rectangular and Triangular shown in Figure 4.2 is considered.

The rectangular VGs are abbreviated as RVGs and the Triangular VGs as TVGs. The height, h of the VGs is set to be 0.5 times the height of the boundary layer (δ). Godard and Stanislas (2006) in the optimisation study of passive vortex generators noted the ratio of the length of the VG vane to its height, $\frac{l}{h}$ should at least be two. Thus, the length of VG vane in the current study is chosen as $3h$. To investigate the influence of the change in angle of attack (β) of the VG vane on the induced flow, four angles 8°, 14°, 20° and 30° is selected.

The computational setup used in the current study is depicted in Figure 4.4. Further, to replicate the induced flow-field four VG vanes arranged in a row as shown in Figure 4.3 is considered.

At the inlet, a Blasius profile with a freestream velocity of $15m/s$ and a boundary layer thickness of $9mm$ is prescribed. Initial results showed that $150mm$ downstream from the start of the domain, the boundary

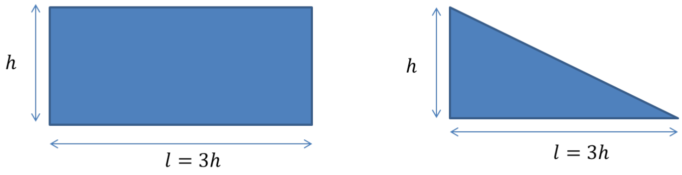

Figure 4.2: Illustration of Rectangular VG vanes (RVGs) and Triangular VG vanes (TVGs).

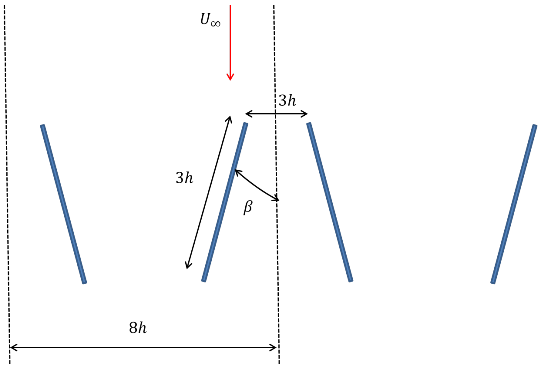

Figure 4.3: Illustration of the VG configuration.

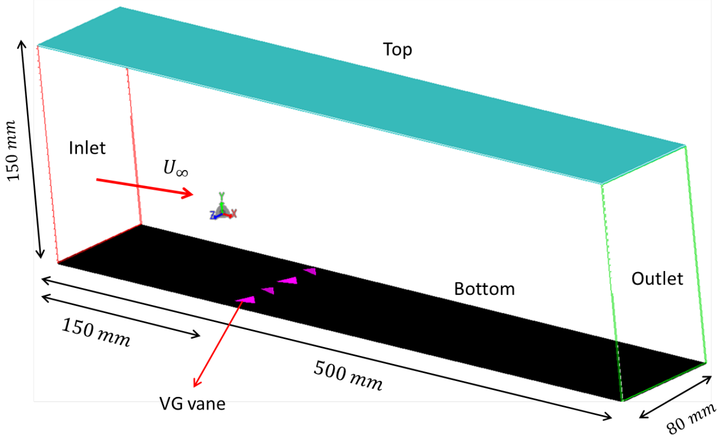

Figure 4.4: Illustration of the computational domain for laminar boundary layer flow.

layer thickness (δ) grew to approximately $10mm$. The VG vanes are placed at this point and consequently, the height of the VG vanes is selected to be $5mm$, so that $\frac{h}{\delta} = 0.5$. At the outlet, a pressure boundary condition is imposed and the default, the periodic boundary condition is retained on either side of the domain. The primary reason for using four VG vanes in the computational domain rather than just one vane is to reduce the influence of the periodic boundary condition on the unsteady flow-field. For example, the experimental study on the stability of the counter-rotating vortex pair by Leweke and Williamson (1998) showed that the unsteady movement of vortices about the centre line is not symmetric in the presence of vortex instabilities. The summary of both the cases is tabulated in Table 4.1.

4.3. GRID CONVERGENCE STUDY

In any given computational study it is necessary to select the appropriate grid (mesh) resolution carefully. The selection of this grid should be based on the type of analysis required and the likely flow conditions to be encountered. To this end, a grid convergence study, which helps to quantify the numerical uncertainty is

Computational Domain ($length \times width \times height$)	At Inlet	Position of VG vane	δ at position of VG vane	h
500 mm × 80 mm × 150 mm	Blasius profile $\delta = 9mm$ $u_\infty = 15m/s$	150 mm	10 mm	5 mm

Table 4.1: Summary of the computational setup.

employed. One of the most commonly used methods in CFD to ascertain grid convergence is by performing a Grid Refinement Study (GRS) (Roache, 1997).

In essence, GRS involves considering three grids which have been systematically refined. Using these three grids of different resolution (say: coarse, medium and fine) it is possible to determine the rate the convergence ($p_{convergence}$). One of the ways to identify $p_{convergence}$ is by graphically plotting the monitored parameter vs the grid size on a log-log plot. The slope of this curve gives the $p_{convergence}$. Further, using this $p_{convergence}$ in conjunction with Richardson extrapolation technique it possible to arrive at the Grid Convergence Index (GCI) and the required resolution. The paper on quantification of uncertainty in CFD by Roache (1997) provides a comprehensive overview of this process.

In the current thesis, something similar was attempted. Three grids labelled coarse, medium and fine with resolution/minimum cell size as noted in Table 4.2 is considered. To determine the rate of convergence, spatially averaged surface pressure on the VG vane is considered. The resultant log plots did not show any clear trend which could be associated with convergence. As a result, it was not possible to determine the rate of convergence. This is likely because the VG induced flow is inherently unsteady. Additionally, the occurrence of the further unsteady phenomenon such as local re-circulation zones close to the VG vanes impacts the spatially averaged surface pressure values. Consequently, contributing to misleading data for the convergence study. The observed variation in spatially averaged surface pressure values with time is shown in Figure 4.5. The y-axis has been normalised by using $P_{ref} = 101.325kPa$.

Grid Type	**Min Lattice Dimension [m]**
Coarse	0.125×10^{-3}
Medium	0.1×10^{-3}
Fine	0.08×10^{-3}

Table 4.2: Different Grid Resolution

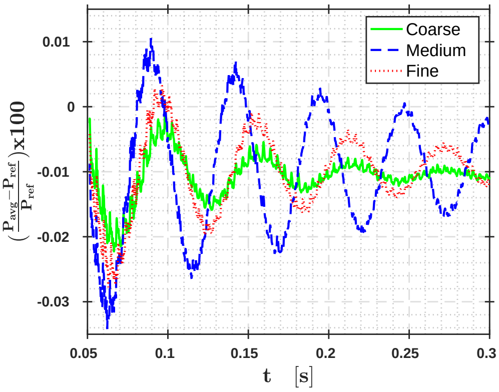

Figure 4.5: Variation of spatially averaged surface pressure in time on VG vane.

The pressure signals in Figure 4.5 is transformed into the frequency domain using Matlab's pwelch function. In pwelch, the given input signal is divided appropriately into segments with a default 50% overlap. A Hamming window then multiplies the segments before computing the periodogram. These modified periodograms are then averaged to get the power spectral density (PSD) as a function of frequency. The results of PSD is scaled in Decibels (dB) and represented as function of frequency in Figure 4.6a. The figure shows that the energy distribution in different frequencies changes with the grid resolution. This is likely because the sampling frequency is not the same for all the grids considered. In PowerFLOW, the grid resolution as previously mentioned is linked to the time-step. Further, the time-step determines the frequency at which data is collected (sampling frequency, f_s). The sampling frequency for the coarse, medium and fine grids are $13.465 kHz$, $16.83 kHz$ and $19.093 kHz$ respectively. Therefore, interpolating the original pressure signal such that the $f_s = 13.465 kHz$ for all the grids and replotting the result in the frequency domain in Figure 4.6b.

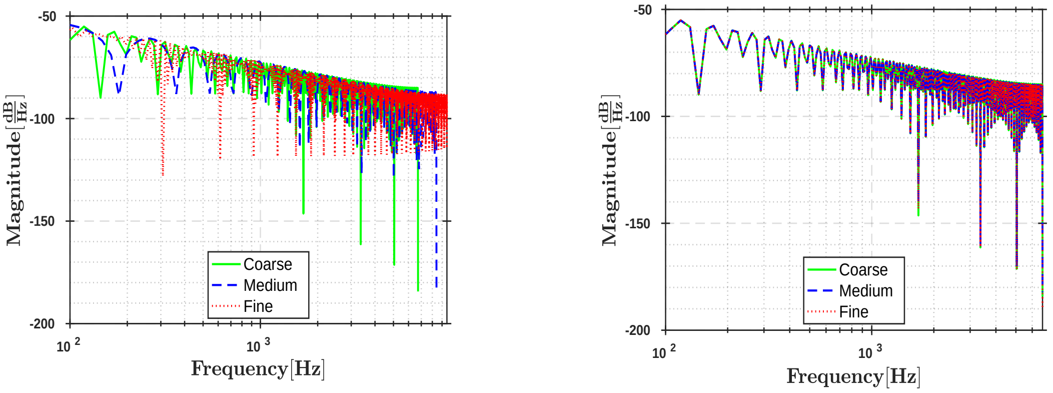

(a) With different sampling frquency, f_s

(b) With same sampling frequency, $f_s = 13.465 kHz$

Figure 4.6: Energy content in the different frequencies for the Coarse, Medium and Fine grids.

In Figure 4.6b,interestingly the energy distribution for the different grids coincide. Indicating that the coarse grid replicates the energy distribution in the fine grid at this f_s. Since the frequency of interest in the current study is on the order of $1000 Hz$ (based on the frequency associated with vortex instabilities), the resolution of the coarse grid is chosen for all the simulations. Additionally, the required computation time and resources for using the fine or medium grid is found to be not feasible.

4.4. VORTEX IDENTIFICATION

Identification of vortices using suitable mathematical model is one of the prevailing issues turbulent flow. The article on the identification of a vortex by Jeong and Hussain (1995), provides an overview of the most commonly used vortex identification techniques. Some of these techniques from [57] are as discussed below:

4.4.1. VORTICITY MAGNITUDE

Vorticity magnitude ($|\omega|$) is related to the intensity of the vortices and can be used to represent the vortex cores (Metcalfe *et al.*, 1987; Bisset *et al.*, 1990). However, in case of vortices close to the ground, using peak vorticity $|\omega_{peak}|$ to identify vortex centre can result in inaccuracies. This inaccuracy is mostly due occurrence of ω maxima and minima or vice versa at the wall, depending on the direction of rotation of the vortex. Therefore, $|\omega|$ is not best suited for studies involving vortices close to the wall.

4.4.2. VELOCITY DISCRIMINANT

For the Galilean-invarient techniques, the velocity gradient tensor (∇u) is extensively used. The eigenvalues (σ) of the ∇u tensor satisfies the characteristic equation:

$$\sigma^3 - P\sigma^2 + Q\sigma - R = 0 \tag{4.11}$$

where, P, Q and R are the invariants of the ∇u tensor, which can be expressed in terms of the summations of the partial derivatives of the components of velocity as :

$$P = \frac{\partial u_i}{\partial x_i} \tag{4.12}$$

$$Q = \frac{1}{2}((\frac{\partial u_i}{\partial x_i})^2 - \frac{\partial u_i}{\partial x_j}\frac{\partial u_j}{\partial x_i}) \tag{4.13}$$

$$R = det(\frac{\partial u_i}{\partial x_j}) \tag{4.14}$$

The velocity discriminant (Δ), is defined as:

$$\Delta = (\frac{1}{3}Q)^3 + (\frac{1}{2}R)^2 \tag{4.15}$$

For complex eigenvalues of equation 4.11, the velocity discriminant will be greater than zero. Chong *et al.* (1990), in the study of three-dimensional flow-field showed that for $\Delta > 0$, the velocity field about that point would resemble a vortex. Physically, for $\Delta > 0$, local streamlines about that point will form a spiral or a closed pattern when moving with the reference frame moving with the same velocity as that of the point considered. Nevertheless, Jeong and Hussain (1995) notes that in comparing Δ with other vortex identification techniques, Δ is found to be inadequate for conically symmetric vortex flows. Further, in Jeong and Hussain it is also noted that Δ results in very noisy vortex boundary.

4.4.3. Q - CRITERIA

Using the second invariant of the ∇u tensor, Q (equation 4.13) Hunt *et al.* (1988) defined vortex as a region of positive Q with local pressure being lower than ambient value. This technique is also commonly referred to as the 'Q-Criteria'. For incompressible flow ($\frac{\partial u_i}{\partial x_i} = 0$), Q from equation 4.13 can be simplified and expressed in terms of the symmetric (S) and anti-symmetric (Ω) components of ∇u as:

$$Q = -\frac{1}{2}\frac{\partial u_i}{\partial x_j}\frac{\partial u_j}{\partial x_i} = \frac{1}{2}(||\Omega||^2 - ||S||^2) \tag{4.16}$$

$$||\Omega|| = [tr(\Omega\Omega^T)]^{\frac{1}{2}} \quad \text{with,} \quad \Omega_{ij} = \frac{1}{2}(\frac{\partial u_i}{\partial x_j} - \frac{\partial u_j}{\partial x_i}) \tag{4.17}$$

$$||S|| = [tr(SS^T)]^{\frac{1}{2}} \quad \text{with,} \quad S_{ij} = \frac{1}{2}(\frac{\partial u_i}{\partial x_j} + \frac{\partial u_j}{\partial x_i}) \tag{4.18}$$

The symmetric part (S) and antisymmetric part (Ω) represents the shear strain rate and vorticity respectively. Thus, the Q-criteria physically represents the balance between the vorticity and shear-strain. The region with $Q > 0$ corresponds to a region with vorticity greater than the shear strain and therefore associated with a vortex. However, Jeong and Hussain (1995) importantly points out that for a region with $Q > 0$ the occurrence of pressure minimum inside that region is not necessarily explicit with the possibility that the pressure minima could be on the boundary of the region with $Q > 0$.

4.4.4. λ_2 - CRITERIA

For an ideal vortex, pressure tends to have local minimum about the axis of rotation of the fluid due to the cyclostropic balance between the centrifugal force and the pressure force. Using this as the starting point, Jeong and Hussain (1995) associates a vortex with a local pressure minima in a plane normal to axis of the vortex. The so defined vortex region mathametically corrsesponds to $\lambda_2 < 0$. Here, λ_2 is the second eigenvalue of the pressure Hessian ($\frac{\partial^2 p}{\partial x_i \partial x_j}$) tensor, arranged such that $\lambda_1 \geq \lambda_2 \geq \lambda_3$. The equation for Hessian of pressure is obtained by taking the gradient of the momentum equation as:

$$\frac{\partial a_i}{\partial x_j} = -\frac{1}{\rho}\frac{\partial^2 p}{\partial x_i \partial x_j} + \nu\frac{\partial^3 u_i}{\partial x_j \partial x_k \partial x_k} \tag{4.19}$$

where, $\frac{\partial a_i}{\partial x_j}$ ($a_i = \frac{Du_i}{Dt}$) is the acceleration gradient, which can be decomposed into symmetric and anti-symmetric parts as:

$$\frac{\partial a_i}{\partial x_j} = [\frac{DS_{ij}}{Dt} + \Omega_{ik}\Omega_{kj} + S_{ik}S_{kj}] + [\frac{D\Omega_{ij}}{Dt} + \Omega_{ik}S_{kj} + S_{ik}\Omega_{kj}] \tag{4.20}$$

Since the pressure term from equation 4.19 is symmetric, equating just the symmetric part from equation 4.19, we have pressure Hessian given by:

$$\frac{DS_{ij}}{Dt} - \nu\frac{\partial^2 S_{ij}}{\partial x_k \partial x_k} + \Omega_{ik}\Omega_{kj} + S_{ik}S_{kj} = -\frac{1}{\rho}\frac{\partial^2 p}{\partial x_i \partial x_j} \tag{4.21}$$

The local pressure minima in the flow can be determined based on the eigenvalues of the pressure Hessian tensor. If the eigenvalues are positive and real, then it corresponds to a minimum. From equation 4.21 it is seen that the pressure is not just influenced by rotation as previously indicated in the ideal vortex scenario. In fact, equation 4.21, shows that pressure is also affected by unsteady straining and viscous effects given by the first and second terms on the left-hand side of the equation. Jeong and Hussain (1995) showed that by constructing the pressure tensor using only the third and fourth terms on the left-hand side of equation 4.21, thereby ignoring the unsteady straining and viscous effects a more restrictive condition for identifying vortices is possible. This forms the basis for identification of vortices by λ_2 criteria. Thus, the eigenvalues λ_1, λ_2 and λ_3 ($\lambda_1 \geq \lambda_2 \geq \lambda_3$) of the so formed pressure Hessian tensor by considering the contributions from only $S^2 + \Omega^2$ with $\lambda_2 < 0$ (because of the negative sign in equation 4.21) becomes the requirement for the vortex core.

Jeong and Hussain (1995), compares the different vortex identification techniques discussed above, it is noted that for various flow scenarios considered, results for Q-criteria and λ_2-criteria are quite similar. In fact, it is shown the Q is related to $\lambda_{1,2,3}$ as : $Q = -\frac{1}{2}(\lambda_1 + \lambda_2 + \lambda_3)$. Nevertheless, in case of vortices subjected to strong external strain, it is found that Q-criteria is inadequate. Further, according to Chen *et al.* (2015) considering the different identification techniques discussed above, when no threshold is specified, the λ_2 -Criteria 'imposed the strictest limit on the identified vortices'. As a result, λ_2 picked up the least number of vortices on the sample PIV data, with the weaker structures being discarded. Thus, based on these observations for identifying vortices induced by VGs, using λ_2 criteria would be beneficial.

On the other hand, Chakraborty *et al.* (2005) in the study of the relationship between local vortex identification schemes, points out that using λ_2-criteria does suffer from the draw back as well. This draw back concerns insufficient understanding of the relation between the actual pressure distribution and the modified pressure distribution considered for the λ_2 computation. Additionally, a snapshot of instantaneous flow induced by the RVG at an angle of attack, $\beta = 8°$ shown in Figure 4.7, indicates that the induced vortex is not axis-symmetric and consists of multiple vortical structures in proximity. Considering that the impact of vortex asymmetry is not known for any of the above-discussed vortex identification techniques, it is necessary to examine further techniques based on flow topology. To this end, scalar vortex field functions Γ_1 and Γ_2 of Graftieaux *et al.* (2001) is considered.

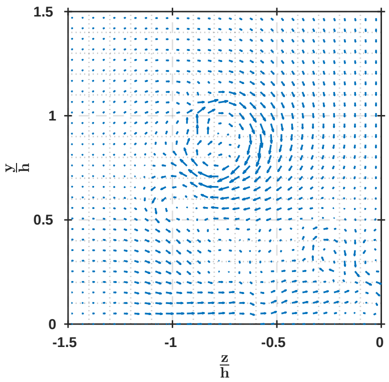

Figure 4.7: Instanstaneous vortex induced by the Rectangular VG vane, $\beta = 8°$.

4.4.5. Γ_1 AND Γ_2 CRITERION

The dimensionless scalar Γ_1 about a fixed point, P is given by:

$$\Gamma_1(P) = \frac{1}{S}\int_{M\in S} \frac{(PM \times U_M).z}{||PM||.||U_M||} ds = \frac{1}{N}\sum_{i=1}^{N} Sin(\theta_M) ds \tag{4.22}$$

where, S is the rectangular domain surrounding the point P, N is the number of points in S, z is a unit vector normal to the measurement plane, θ_M is the angle between velocity vector U_M and the radius vector between points P and M and $||.||$ is the Euclidean norm. Huang and Green (2015) notes that typically the $|\Gamma_1|$ ranges between 0.9 and 1 in the regions close to the vortex centres. A simple illustration of a rectangular domain on a grid with the line intersection representing the points N_i, the centre point P and an arbitrary point M with velocity vector U_M is as shown in Figure 4.8.

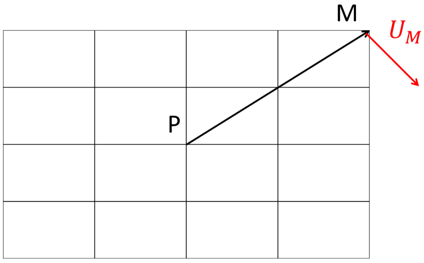

Figure 4.8: Illustration of Γ_1 calculation.

Further, studies from both Graftieaux *et al.* (2001) and Huang and Green (2015) note that the number of points, N in the domain acts like a spatial filter and is seen to weakly affect the location of maximum $|\Gamma_1|$. However, one of the problems with Γ_1 is that, it is not Galilean invariant, i.e. Γ_1 changes with the translation of the reference frame. In order to overcome this, a new scalar function Γ_2 is defined, which also considers the convection velocity (U_P) around P. This is given by:

$$\Gamma_2(P) = \frac{1}{N}\sum_{i=1}^{N} \frac{(PM \times (U_M - U_P)).z}{||PM||.||U_M - U_P||} \quad \text{with,} \quad U_P = \frac{1}{N}\sum_{i=1}^{N} U ds \tag{4.23}$$

For a small S ($S \longrightarrow 0$), Graftieaux *et al.* (2001) mentions that Γ_2 can be shown to be a function of the anti-symmetric part of ∇u tensor and the eigenvalues of the symmetric part of ∇u. Using this, Graftieaux classifies local flow topology as:

- $|\Gamma_2| < \frac{2}{\pi}$ - local flow dominated by strain.
- $|\Gamma_2| = \frac{2}{\pi}$ - Pure shear.
- $|\Gamma_2| > \frac{2}{\pi}$ - local flow dominated by rotation.

Dispute the fact that above discussed vortex identification techniques have been validated for different flow scenarios, it is seen that there is no single technique which performs the best under all circumstances. Each of these techniques are seen to have certain drawbacks. For example, as previously mention, Q-criteria becomes inaccurate in the presence of strong shear. Similarly, for λ_2 criteria, the relation between the modified pressure used to identify vortex and the actual pressure is not very clear and moreover, for the local velocity based technique, the finite size of the domain could influence the Γ_2 calculation. Thus for the current study due to the unsteady nature of the induced flow-field consisting of the primary vortices and additional secondary vortices in random combination, it is found that, it is difficult and inaccurate to a priory select one identification technique and employ it to automatically select the vortex centres for all the encountered scenarios. In an attempt to minimise the inaccuracies it is attempted here to use a modified vortex identification criteria, wherein λ_2 criteria based on the ∇u tensor is used in concurrence with the local flow topology base Γ_2 criteria.

4.4.6. MODIFIED CRITERIA

In the modified criteria, initially, the λ_2 - criteria is applied to the flow-field in-order to identify the different vortex regions. Considering the asymmetric nature of some of the vortical structures observed, it is expected that, even if the minimum of λ_2 criteria (ideally corresponds to vortex center) does not correspond to the centre of rotation, it is atleast able to identify a general region of rotation based on the value of threshold specified. Using the so obtained vortex region, an inflection point check is performed at all the points forming the vortex region. Here, inflection point is defined as a point about which atleast one of in-plane velocity components are zero i.e. either horizontal or vertical. An illustration of the inflection point, P such that $u_1 + u_2 = 0$ is as shown in Figure 4.9.

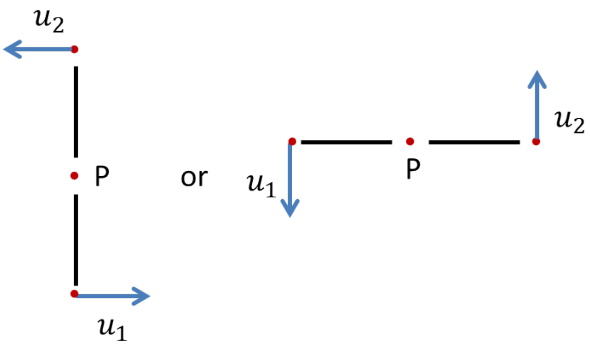

Figure 4.9: Illustration of inflection point.

This is based on the idea that, for an ideal vortex, sum of the in-plane velocity components about the centre is zero. Further, at all the identified inflection points, Γ_2 is computed with the domain size appropriately selected based on trial and error in accordance with the flow-field considered. The point about which the $|\Gamma_2|$ is the highest, is selected as the vortex centre. Figure 4.10, illustrates the comparison between the vortex centres identified using the λ_2 - criteria and modified criteria on a theoretical Lamb-Oseen vortex and instantaneous flow-field data downstream of the VG.

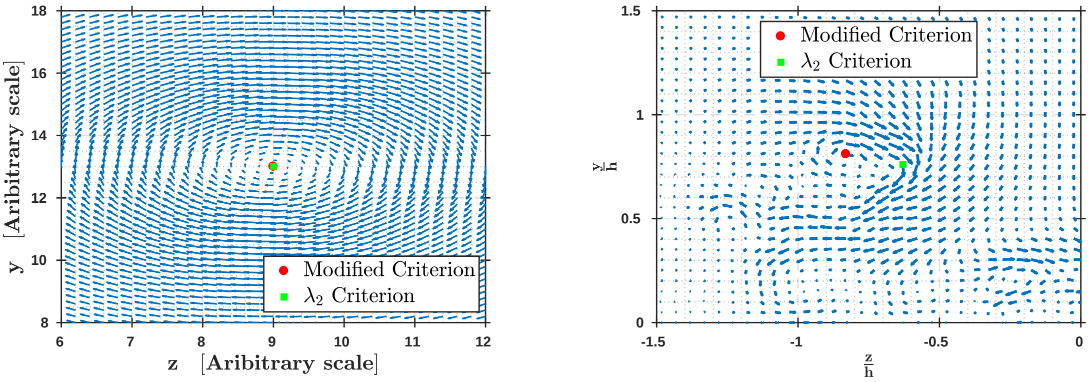

(a) Theoretical Lamb-Oseen vortex

(b) Instantaneous flow-field downstream RVG, $\beta = 8°$

Figure 4.10: Comparision of the λ_2 - Criteria and the Modified Criteria.

From Figure 4.10, it is seen that, in case of the theoretical vortex model shown in Figure 4.10a, there is a good agreement in vortex identification for both the λ_2 and modified criteria. However, in Figure 4.10b, where the instantaneous flow-field data is considered, based on visual comparison, using the modified criteria results in a vortex centre which is much closer to the actual centre than in case of the λ_2-criteria. However, it is imperative to mention here that, the observed improvement in vortex centre identification was not true for all the test cases considered. In fact, in some of the test cases it was observed that λ_2 - criteria resulted in better vortex centre identification. Nevertheless, on an average it is observed that using modified criteria resulted in lower inaccuracies in vortex centre identification. The algorithm of the modified criteria is illustrated below:

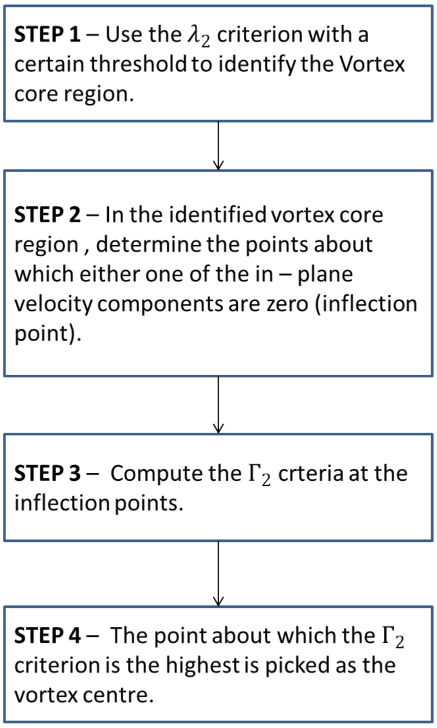

STEP 1 – Use the λ_2 criterion with a certain threshold to identify the Vortex core region.

STEP 2 – In the identified vortex core region , determine the points about which either one of the in – plane velocity components are zero (inflection point).

STEP 3 – Compute the Γ_2 crteria at the inflection points.

STEP 4 – The point about which the Γ_2 criterion is the highest is picked as the vortex centre.

5

RESULTS AND DISCUSSION

In results and discussion, initially, details of the different data acquisition planes is described in Section 5.1. Following this in Section 5.2 results for rectangular vortex generators (RVGs) at an angle of attack (β) of 14° is presented. Then, results for triangular vortex generators (TVGs) under the same conditions is shown in Section 5.3. For both the cases, results are looked at from the perspective of mean flow-field, instantaneous flow-field and acoustics. It is of interest to note the difference in the flow-field induced by the two different VG profiles. Finally, in Section 5.4 influence of the angle of attack of the VG vane on both RVGs and TVGs is discussed.

5.1. DATA ACQUISITION

In the current thesis, to study the flow-field induced by the Vortex Generators (VGs) data is acquired at three different downstream positions. By setting the origin of the x-axis at the trailing edge of the VG vane ($\frac{x-x_{vg}}{h} = 0$), data is acquired at downstream positions corresponding to h, $5h$ and $20h$, where h represents the height of the VG vane. This is illustrated in Figure 5.1.

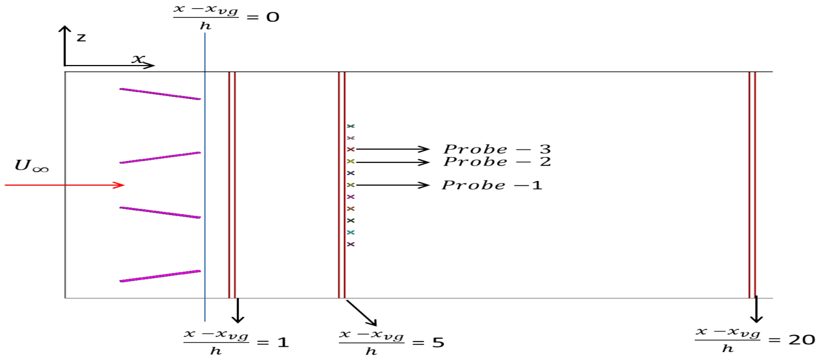

Figure 5.1: Illustration of the downstream data planes.

In addition to this, probes of local cell/voxel size are placed in the domain at $\frac{x-x_{vg}}{h} = 5$. There are multiple probes distributed spanwise in a line at this downstream position, all of them at the height of $\frac{y}{h} = 1$. These are primarily used to capture data at very high frequency, $f = 6.734 \times 10^4 Hz$. However, data from only probes labelled 1, 2 and 3 is found to be most useful (discussed later). The spanwise positions of the Probes 1, 2 and 3 corresponds to $\frac{z}{h} = 0$, 1.6 and 2.4 respectively. For the far-field acoustics, surface pressure data of the VG vanes is captured. The sampling frequency for the surface pressure data is also, $f = 6.734 \times 10^4 Hz$. Further, for flow visualisation, averaged flow-field data and surface data is captured in the entire domain. Data is sampled for all the cases after two flow passes in the entire domain.

The arrangement of the microphone array to evaluate the far-field acoustics is shown in Figure 5.2. All the microphones, represented by crosses in Figure 5.2 are radially at a distance of 500h from the mid-point of the VG pair, encircled in Figure 5.2. For all the sound pressure level (SPL) plots the data from microphone coinciding with the mid-point of the VG-pair is used. For the directivity plots the data from the remaining microphones, forming a circle is utilised.

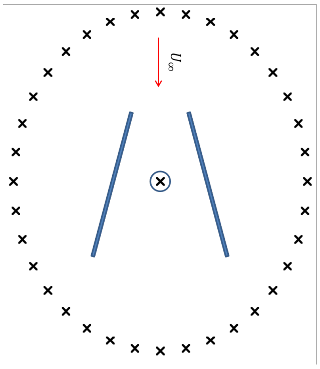

Figure 5.2: Illustration Microphone arrangement for the Sound Pressure Level and directivity plots.

5.2. RECTANGULAR VORTEX GENERATOR

To assess the effectiveness of VGs, streamwise evolution of the mean flow-field is considered. In this section results for Rectangular VG (RVG) vane at 14° subjected to Laminar boundary layer (LBL) is presented.

5.2.1. MEAN FLOW-FIELD PROPERTIES

The mean velocity contour of the flow-field 5h downstream of the RVG vane is as shown in Figure 5.3.

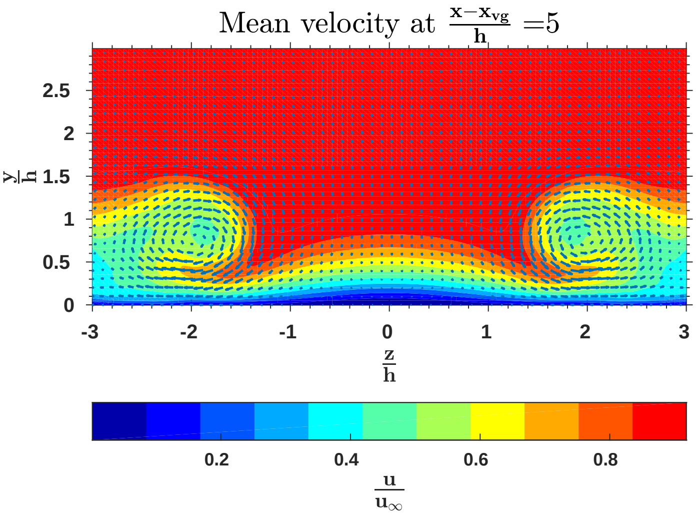

Figure 5.3: Mean flow-field at $\frac{x-x_{vg}}{h}$ = 5 for RVG, $\beta = 14°$. The background contour indicates the axial velocity whereas, the in-plane velocity is indicated by the arrows.

From Figure 5.3, it is evident that the mean flow-field shows the presence of a counter-rotating vortex pair, with a deficit in the axial velocity in the region close to the vortex core. The arrangement of these vortices is identical to the common down-wash arrangement previously shown in Figure 3.2. The streamwise vorticity contour computed using the in-plane velocity components at $\frac{x-x_{vg}}{h} = 5$, shown in Figure 5.4, indicates the presence of concentrated vortex structures. The downstream evolution of peak streamwise vorticity is shown in Figure 5.4.

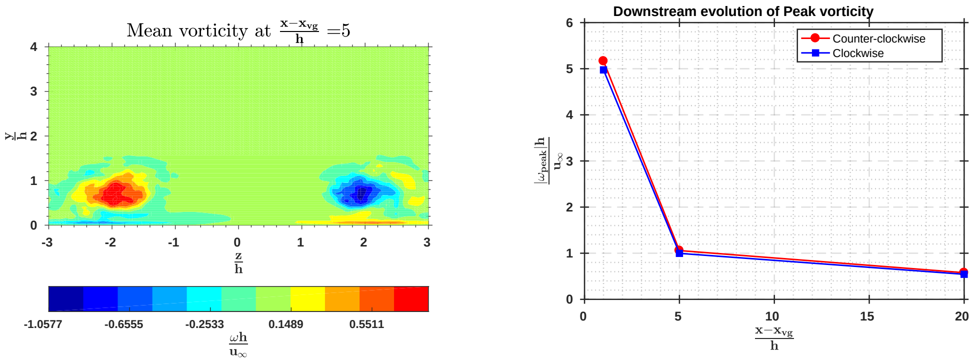

(a) Vorticity contour

(b) Downstream evolution of peak streamwise vorticity

Figure 5.4: Vorticity contour and downstream evolution of peak streamwise vorticity for RVGs, $\beta = 14°$.

Figure 5.4b indicates a rapid decay of peak streamwise vorticity downstream of the VG vanes. At $\frac{x-x_{vg}}{h} = 20$, the value of peak vorticity is reduced to approximately 12% of the value at the plane closest to the VG vane. This decay is most plausibly due to the combined effect of vortex core diffusion and enhanced dissipation due to the proximity to the wall, resulting in higher shear. Yao *et al.* (2002) in the study of embedded streamwise vortices also notes a peak vorticity decay. However, the observed rate of decay in their study is much lower, with peak streamwise vorticity reducing to about 10% of the initial value at $\frac{x-x_{vg}}{h} = 50$. This observed difference is most likely because in the study of Yao *et al.* (2002), the VG vane is subject to a turbulent boundary layer (TBL) profile. This TBL unlike the LBL is much fuller. As a result, stronger vortices are induced, which in-turn can persist further downstream.

On the other hand comparing the results in Figure 5.4b with measurements from Shim *et al.* (2015), where a LBL is used, the results show better agreement. In their study, $|\omega_{peak}|$ is shown to be approximately 16% of the initial value at $\frac{x-x_{vg}}{h} = 20$, which is still higher than the value observed in the current study. However, this difference is likely because VG vanes in Shim *et al.* (2015) is bigger with $\frac{h}{\delta} = 1$.

Using the modified criteria previously described in Section 4.4.6 to identify the vortex centres , the observed downstream evolution of the mean clockwise and counter-clockwise vortices for RVGs at $\beta = 14°$ is shown in Figure 5.5. The mean vortex path indicated that both clockwise and counter-clockwise vortex in the spanwise direction moves away from each other. Further, looking at the wall-normal direction the vortices initially move towards the wall, however further downstream, they traverse away from the wall. Based on potential theory, Pearcy (1961), Lögdberg *et al.* (2009) and others, explain the observed spanwise movement of the vortices as an influence of the imaginary or mirror vortices. The initial downward wall-normal motion of the vortices is due to the neighbouring (real) vortex of the same VG pair. However, further downstream as the vortices grow and simultaneously move away in the spanwise direction, they begin to come under the influence of the (real) vortex from the neighbouring VG pair resulting in the observed upward motion.

In addition to the clockwise and counter-clockwise (primary) vortices, horseshoe vortices, arising from the leading edge of the VG vanes are also present. These horseshoe vortices are also referred to as secondary vortices. Figure 5.6, showing the iso-surface of λ_2 criterion illustrates the presence of secondary vortices.

Focusing on the flow around VG vane, the presence of various flow recirculation zones is noted. Figure 5.7 highlights the regions in which the streamwise component of velocity is less than zero in the domain sur-

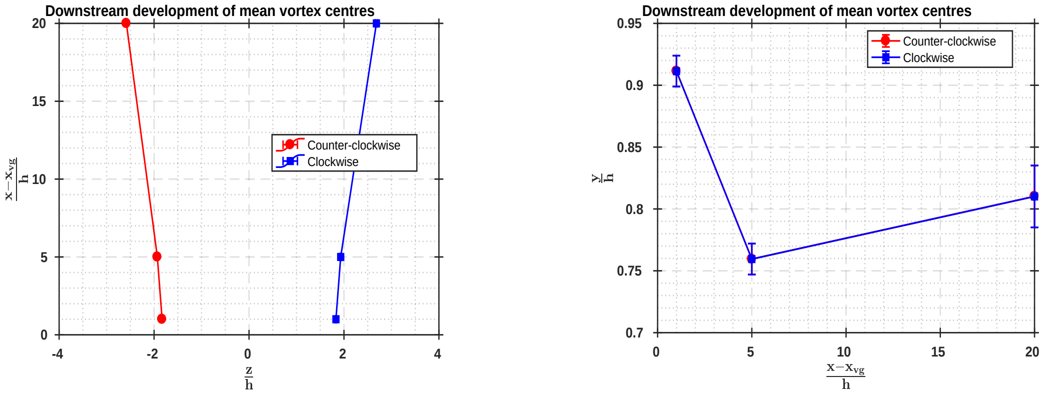

(a) Vortex centre path in the x-z plane (b) Vortex centre path in the x-y plane

Figure 5.5: Streamwise evolution of vortex centre paths for RVGs, $\beta = 14°$.

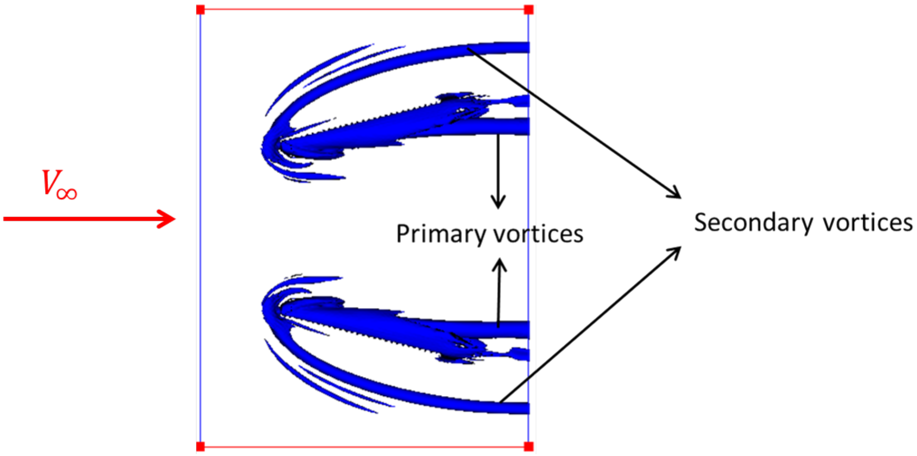

Figure 5.6: Iso-surface λ_2-criteria with a threshold of -1×10^6 illustrating primary and secoundary vortices for RVGs, $\beta = 14°$.

rounding the RVG vanes. The recirculation zones are labelled A-E in Figure 5.7. Visual examination indicates that Zone A based on its shape is linked to the formation of the stagnation point at the leading edge of the vane and the curved secondary vortex. Zone B indicates the presence of a leading edge separation bubble on VG vane. Similar separation bubble is also encountered in flow over an airfoil at moderate angles of attack (Vatsa and Carter, 1984). The C_p [$C_p := \frac{P-P_{ref}}{P_{ref}}$ with, $P_{ref} = 101.325 kPa$] distribution of the mean surface pressure on the VG vane at $\frac{y}{h} = 0.5$ is shown in Figure 5.8. This figure indicates the presence of a suction peak at the leading edge of the vane followed by a plateau, which is typically associated with the separated zone as the pressure fails to recover. Zone D just downstream of the trailing edge of the vane indicates the presence of the recirculation zone in the near wake region. Zones C and E indicate the presence of re-circulation zones in between the VG vanes. The cause for their occurrence is not very clear. A likely explanation could be the influence of a relatively strong primary vortex coupled with the local pressure gradient induced in between the vanes. Figure 5.9 showing the plot of C_p obtained by considering the mean surface pressure on the bottom surface along the $\frac{z}{h} = 0$, confirms the presence of a pressure gradient in the streamwise direction.

For flow control, it is important to observe the mean velocity profile. For RVGs at $\beta = 14°$ the downstream development of the mean velocity along the centre line of the VG pair ($\frac{z}{h} = 0$), is shown in Figure 5.10. Progressively downstream, as expected, the boundary layer profile is fuller. Further investigating the boundary layer profile in Figure 5.10 at $\frac{x-x_{vg}}{h} = 1$, close to the wall a small curve indicative of flow reversal is evident.

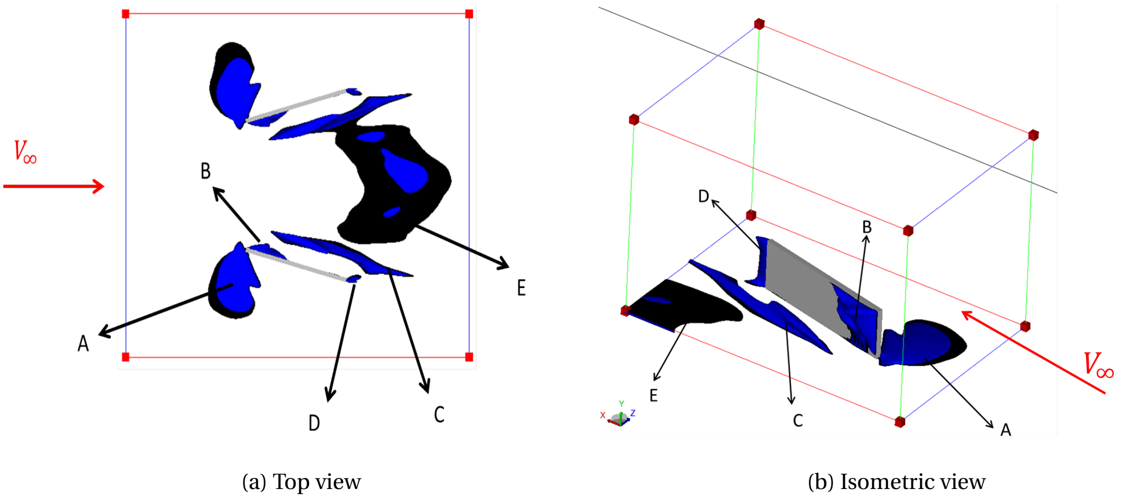

(a) Top view (b) Isometric view

Figure 5.7: Recirculation zones surrounding the RVG vane, $\beta = 14°$.

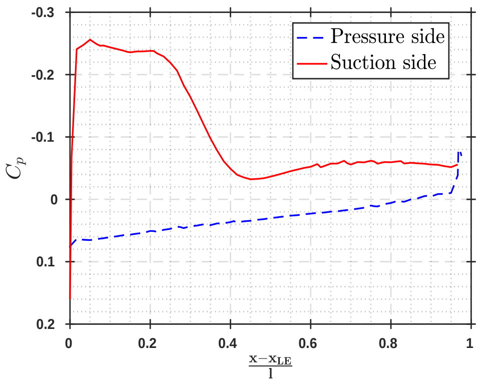

Figure 5.8: C_p at $\frac{y}{h} = 0.5$ for RVGs, $\beta = 14°$.

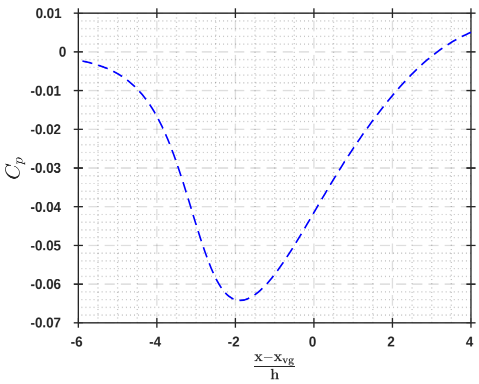

Figure 5.9: C_p along $\frac{z}{h} = 0$ for RVGs, $\beta = 14°$.

Thereby, re-illustrates the presence of previously noted re-circulation zones in between the VG vane.

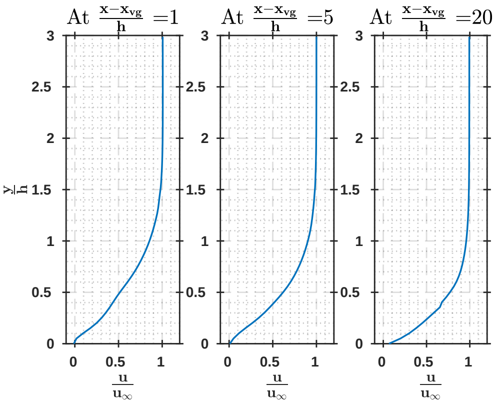

Figure 5.10: Downstream development of the mean velocity profile along $\frac{z}{h} = 0$ for RVG, $\beta = 14°$.

5.2.2. INSTANTANEOUS FLOW-FIELD PROPERTIES

The velocity contour of the instantaneous flow-field $5h$ downstream of the RVG at $\beta = 14°$ subjected to LBL is shown in Figure 5.11. Unlike the velocity contour in mean flow, which indicates the presence of circular vortex structures, results from instantaneous flow show irregular vortices. The streamwise vorticity contour at the same downstream position from the RVG vanes shown in Figure 5.12 further illustrates this point. Thereby, suggesting that the circular nature of the vortex in the mean flow-field could be due to averaging of the data.

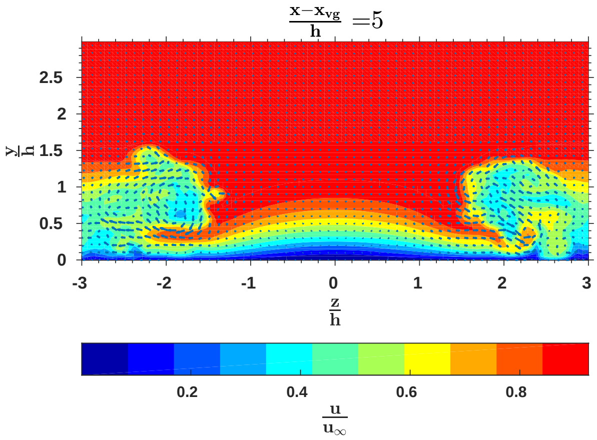

Figure 5.11: Instantaneous flow-field at $\frac{x-x_{vg}}{h} = 5$ for RVG vanes, $\beta = 14°$.

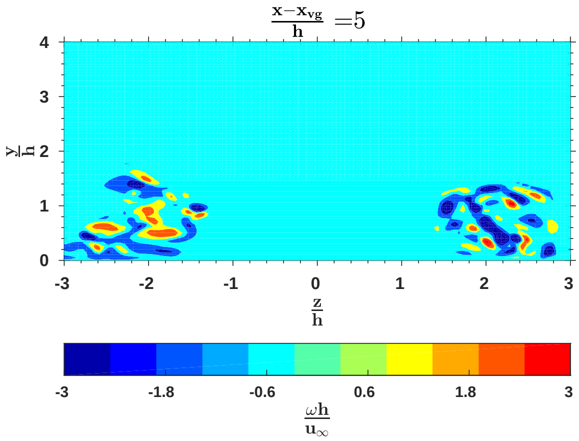

Figure 5.12: Streamwise vorticity contour at $\frac{x-x_{vg}}{h} = 5$ for RVGs, $\beta = 14°$ and $t \approx 0.25$s.

Surprisingly, Figure 5.12 indicates the presence of a cluster of irregular patches of vorticity in the region where previously in the mean flow contour (Figure 5.4a) compact regions of vorticity is observed. This result needs to be interpreted with caution because, in the presence of a vortex close to the wall, vorticity of the opposite nature/sign is induced close to the wall, it is possible that this opposite sign vorticity is entrapped into the primary vortex flow as it curls and simultaneous convects downstream. Alternately, it is also possible that the interaction of the primary vortex structures with various other flow structures could also be responsible for the current vorticity plot. Nevertheless, it is of the author's opinion that unless individual fluid particles are tracked in a Lagrangian sense, it will difficult to explain the result in the vorticity contour. One implication of this result is to highlight the difference between mean and instantaneous flow-fields. The results of both instantaneous velocity and vorticity corresponds to a time instant of $t = 0.25s$

The values of peak vorticity at different downstream positions, frozen in time ($t = 0.25s$) is as shown in Figure 5.13a. Assuming that this peak vorticity is associated with the primary vortices, and comparing with the same in the mean flow (Figure 5.4b), results from instantaneous flow indicate to a much higher magnitude of peak vorticity. A similar observation is noted in the study of Angele and Grewe (2007). Further, in their study it is pointed out that the lower magnitude of vorticity in mean flow is due to the unsteady nature of the vortices, which tends to smear out the vorticity during ensemble averaging.

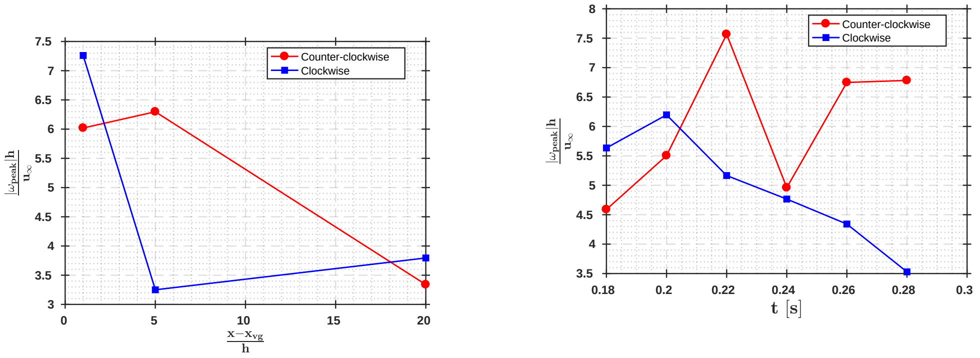

(a) Dowstream variation of peak streamwise vorticity.

(b) Variation of peak streamwise vorticity at $\frac{x-x_{vg}}{h} = 5$.

Figure 5.13: Instantaneous peak vorticity at different downstream positions at $t = 0.25$ and variation of peak vorticity at $\frac{x-x_{vg}}{h} = 5$ in time.

Further, in Figure 5.13, it is seen that there is no clear trend in the variation of the magnitude of the peak vorticity. This is as expected, as the flow is unsteady and the magnitude of vorticity at any given downstream position should be a function of time. This is clearly evident in the plot of variation in peak vorticity with time for both clockwise and counter-clockwise vortices at downstream position $\frac{x-x_{vg}}{h} = 5$, shown in Figure 5.13b. To further analyse this unsteady behaviour of the vortices, instantaneous vortex centres identified using the modified criteria (see Section 4.4.6) at downstream position $\frac{x-x_{vg}}{h} = 5$ as shown in Figure 5.14 is considered.

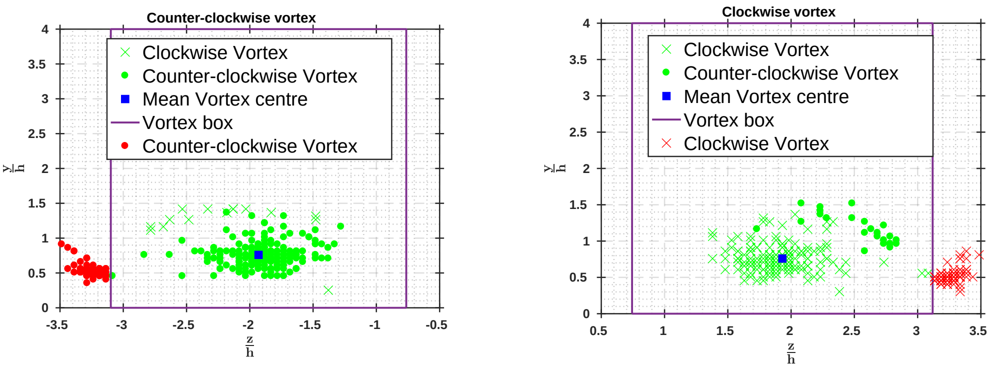

(a) Counter-clockwise vortex centres.

(b) Clockwise vortex centres.

Figure 5.14: Instantaneous vortex centres for RVGs, $\beta = 14°$ at $\frac{x-x_{vg}}{h} = 5$.

In Figure 5.14, the clockwise vortices are indicated by crosses (×) and the counter-clockwise vortices by dots (●). The direction of rotation of the vortices is identified based on the sign of vorticity at the identified vortex centres. Both in Figure 5.14a and Figure 5.14b, in addition to cluster of vortex centres surrounding the averaged/mean vortex centre, a second group of vortices (highlighted in red) is seen. On average, this second cluster of points is further outward in the spanwise direction from $\frac{z}{h} = 0$ and also closer to the wall. This applies to both Figure 5.14a and Figure 5.14b. Based on the previous λ_2 visualisation of the mean flow in Figure 5.6, the red vortex centres appear to coincide with the regions in which the secondary vortices are seen. This is interesting, as initially it is expected that only the primary vortices would be recognised. This is so, because, the code is designed to pick only the strongest vortex in a given snapshot of flow-field. Consequently, this suggests that either the secondary structures are more dominant or primary vortices are highly distorted/irregular in the flow-field. Considering the multiple flow structures seen in Figure 5.11 for instantaneous flow, as result of increased vortex interaction, the latter of the two more plausible. This is considered as a significant drawback of the vortex identification technique implemented, where in the presence of an irregularly shaped vortex, the next strongest vortex which conforms best with the identification method is picked. In order to overcome this, the green coloured vortex centres identified as those linked to the primary vortices is distinguished from the red coloured centres based on the vortex box illustrated in Figure 5.14. The width of this vortex box is determined such that, in both Figure 5.14a and Figure 5.14b it is able to separate the two vortex centre clusters. Based on trial and error for the present flow, a width of 2.5 times the standard deviation about the mean vortex centre is found to be ideal. The standard deviation is determined by considering all vortex centres identified in the respective figures.

Considering the identified green vortex centres, both in Figure 5.14a and Figure 5.14b there is an additional small cluster of opposite sign vortices with respect to the expected counter-clockwise and clockwise vortices respectively. Based on its position, looking back at the different vortex configurations (Figure 3.3) describe by Velte *et al.* (2012), it is possible to expect the presence opposite signed additional secondary vortices. Consequently, by considering only the vortices with the correct sign/direction of rotation, the vortex kinematics is computed. The observed spanwise and wall-normal displacement of the primary counter-clockwise and clockwise vortices about the respective mean vortex centres is shown in Figure 5.15 and Figure 5.16.

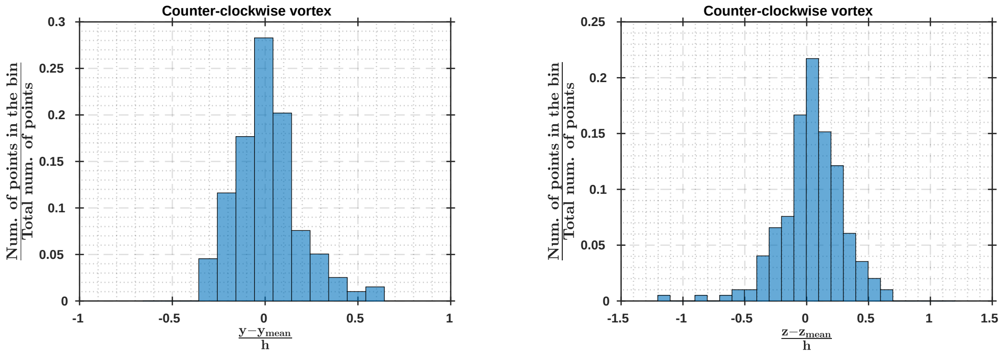

(a) Wall-normal vortex displacement (b) Spanwise vortex displacemnet

Figure 5.15: Wall-normal and spanwise displacement of the primary counter-clockwise vortex for RVG vanes, $\beta = 14°$ at $\frac{x-x_{vg}}{h} = 5$.

From Figure 5.15 and Figure 5.16 it is evident that for both the primary vortices, the observed spanwise displacement of the vortex is greater than the wall-normal displacement of the vortex. This observation is in agreement with those of Angele and Grewe (2007) where experimental results show a similar trend. The presence of the wall close to the vortex is most likely responsible for this difference in the wall-normal and spanwise displacement of the vortices. At the downstream position $\frac{x-x_{vg}}{h} = 5$ the variation in the spanwise position for counter-clockwise and clockwise vortices is approximately $1.5h$ and h respectively. Similarly, the variation in the wall-normal position for the counter-clockwise and clockwise vortices is approximate h and $1.3h$ respectively. From the instantaneous vortex centres indicated in Figure 5.14, the probability density

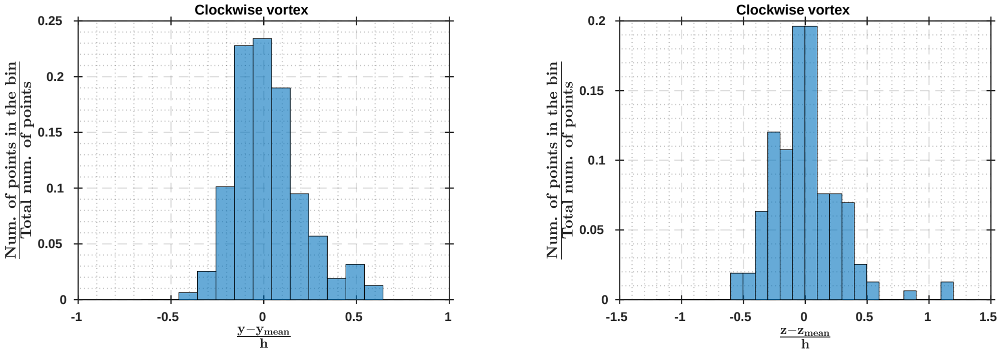

(a) Wall-normal vortex displacement

(b) Spanwise vortex displacemnet

Figure 5.16: Wall-normal and spanwise displacement of the primary clockwise vortex for RVG vanes, $\beta = 14°$ at $\frac{x-x_{vg}}{h} = 5$.

function (PDF), representing the most likely position of the primary vortices at any given time is shown in Figure 5.17.

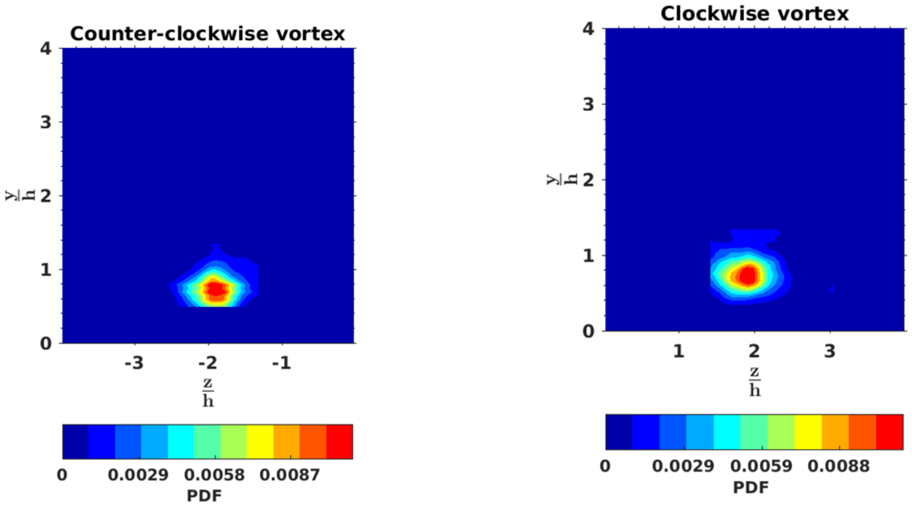

(a) Counter-clockwise vortex.

(b) Clockwise vortex.

Figure 5.17: PDF from the instantaneous vortex centres for RVG vanes, $\beta = 14°$ at $\frac{x-x_{vg}}{h} = 5$.

To further characterise the motion of the primary vortex, the covariance of the matrix containing the vortex centres is considered. The resultant is a symmetric 2 × 2 matrix with variance along the diagonal and covariance in the nondiagonal positions. Subsequently, using the eigenvector and eigenvalues of this matrix, it is possible to characterise the cluster of primary vortex centres distributed around the mean vortex. The principal eigenvector gives the direction along which the observed variation in vortex centre positions is maximum, and the square root of the corresponding eigenvalue gives its magnitude.

In the experimental study involving vortex pairs with axial flow, Roy *et al.* (2011) interpret the direction of principal eigenvector as the preferred direction of motion of the primary vortex. Similarly, in this study, the unsteady motion/meandering of the vortex is characterised based on the angle made by the principal eigenvector with the horizontal (θ_{eig}). This θ_{eig} is illustrated in Figure 5.18. Further, the magnitude of the principal eigenvector is symbolically referred to as the magnitude of meandering. In Figure 5.19, the downstream evolution of both the properties mentioned above is illustrated.

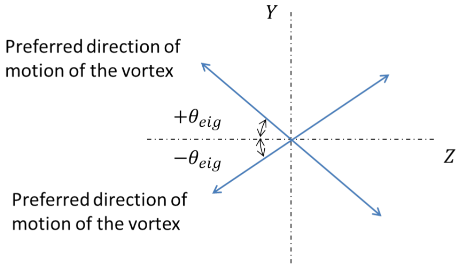

Figure 5.18: Illustration of the chracteristic angle,(θ_{eig}) .

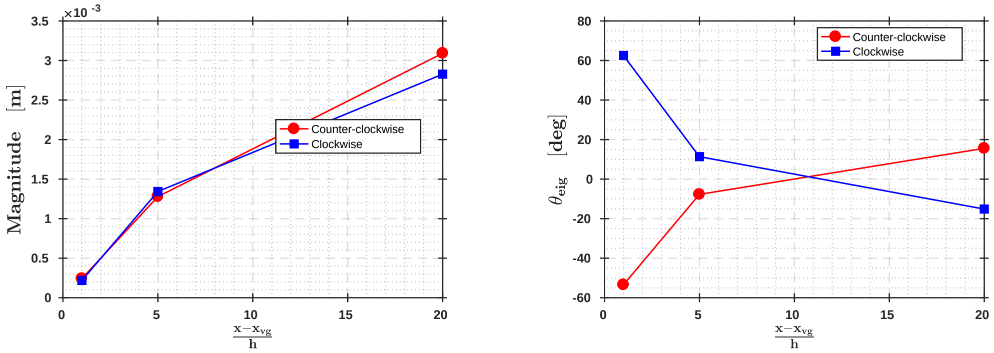

(a) Variation of the magnitude of meandering along the preferred direction with downstream positions.

(b) Variation of chracteristic angle, θ_{eig} with downstream positions.

Figure 5.19: Meandering characteristics for RVG, $\beta = 14°$.

The trends in Figure 5.19a indicates that as we move downstream from the trailing edge of the VG vane, the meandering magnitude increases. A similar trend is noted in the experimental results in Roy *et al.* (2011). Subsequently, in their study, the increase in meandering is shown to be due to the presence elliptical instability (one of the types of co-operative instability). However, it is important to note that the effect of the presence of the wall and additional secondary structures results in a more complicated vortex system in comparison to the single vortex pair arrangement considered by Roy *et al.* (2011). Therefore, based on this, in the current thesis, a direct one to one relation regarding the presence of instability can neither be established nor ignored.

In Figure 5.19b, the characteristic angle (θ_{eig}) depicting the preferred direction of motion of the vortex is shown at different downstream positions. It is interesting to note that θ_{eig} is not constant. Further, for both the clockwise and counter-clockwise vortices as we move from $\frac{x-x_{VG}}{h} = 1-20$, θ_{eig} becomes inverted. To explain this, we must first consider a system of vortices. We have that, any given vortex in this system is under straining influence of the remaining vortices (Jacquin *et al.*, (2003); Leweke *et al.*, 2016). For example, in case of an isolated counter-rotating vortex pair, Jacquin *et al.* (2003) note that the axes of the so induced strain field due to neighbouring vortex is oriented at ±45° as illustrated in Figure 5.20.With this as the basis, returning to Figure 5.19b and also considering the instantaneous vortex centre clusters shown in Figure 5.14, it is possible to make the following observation. At $\frac{x-x_{vg}}{h} = 5$ in Figure 5.14, the nearest vortex, for both the primary clockwise and counter-clockwise vortex is the corresponding secondary vortices. Similarly, at $\frac{x-x_{vg}}{h} = 1$ the secondary vortices are again the closest vortices. However, at $\frac{x-x_{vg}}{h} = 20$, this is no-longer true, because the secondary vortices are not seen to persist till $20h$ downstream. Based on the development of the primary vortices in the mean flow-field shown in Figure 5.5 the image/mirror vortices should be the nearest vortices. This is interesting because, this trend of change in nearest vortex is seen to match the θ_{eig} variation with the observed θ_{eig} getting inverted at $\frac{x-x_{vg}}{h} = 20$ for both the clockwise and counter-clockwise vortex.

However, it is important to note that, the above observation would be valid based on the premise that, the preferred direction of motion is due to the presence of vortex instabilities. Recollecting that the instabilities originate as a result of stretching of vorticity perturbations in the strain field, it can be argued that the strain field induced by the nearest vortex is likely to exert a dominant influence on the vortex under study by virtue of position. Thereby, seemingly responsible for inducing vortex instabilities. Gardarin *et al.* (2008), in the study of flow separation control with VGs, notes a similar inversion and describes it as vortex pair exchange. This vortex pair exchange in their study also represents a change in the influence of nearest neighbouring vortex.

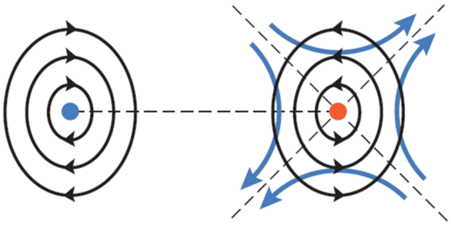

Figure 5.20: Schematic of strain (coloured arrows) induced by the neghouring vortex in a counter-rotating arrangement Leweke *et al.*.

Forestier *et al.* (2003) considered a Lamb-Oseen vortex in a plane and subjected it to random isotropic motion about the centre. Under these circumstances, the Reynolds shear stress (RSS) is seen to be equally distributed in a four lobed structure, as illustrated in Figure 5.21.

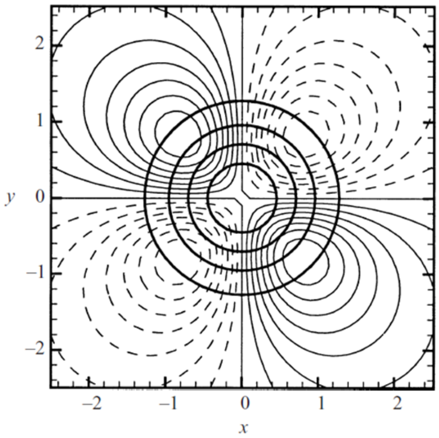

Figure 5.21: Schematic of the Reynolds Shear Stress due to isotropic meandering [13]. The thick black circle represents the vortex with the iso-values of the RSS represented in the background.

Looking back at the results of vortex kinematics in Figure 5.16 and Figure 5.15 it is already seen that vortex displacement is not isotropic as in the case of Forestier *et al.* (2003). As a result, it can be expected that the RSS distribution will look different. In Figure 5.22, the mean RSS distribution computed using the in-plane components of velocity, $(\overline{v'w'})$ is plotted for both the clockwise and counter-clockwise vortices from RVG at $\beta = 14°$.

From Figure 5.22, it is evident that unlike the stress distribution in Figure 5.21, the four lobes here are not equally distributed. For the clockwise vortex, the two positive lobes are dominating over the other two negative lobes and vice versa for the counter-clockwise vortex. Overlapping the previously defined preferred direction of motion of the vortex on the RSS, it is observed that for both clockwise and counter-clockwise vortices the preferred direction of motion of the vortex is almost in-line with the dominant shear stress lobes.

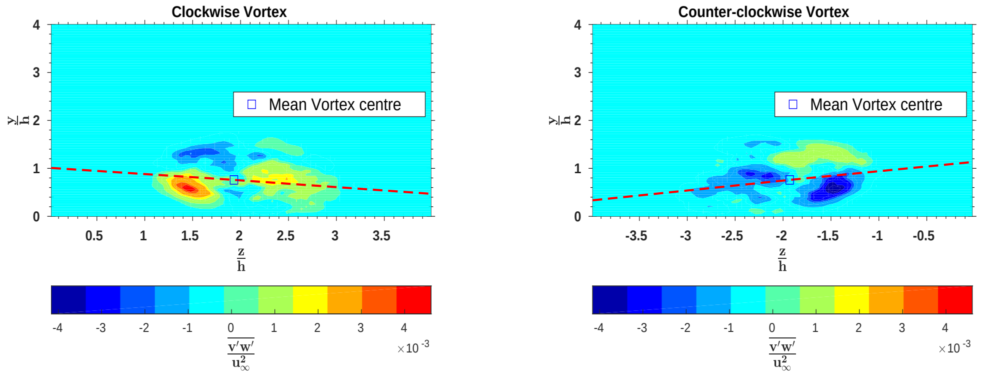

Figure 5.22: Axis of preferred direction of motion (dashed red line) overlapping the distribution of RSS, $\overline{v'w'}$ for RVG , $\beta = 14°$ at $\frac{x-x_{VG}}{h}$ = 5.

This could be an indication that the strain imparted by the neighbouring vortices could be responsible for the induced motion along the preferred direction.

Previous experimental studies on vortex instabilities involving isolated vortices (Devenport *et al.*, 1996; Jacquin *et al.*, 2003), notes of a broadband spectrum with an excess of energy at distinct frequencies when looking at the energy distribution in the flow-field with a meandering vortex. Further, according to Jacquin *et al.* (2001) this characteristic signature of meandering is best captured by considering the energy distribution at mean vortex centre. Therefore to further analyse the presence of any co-operative instability, the power spectrum of the spanwise component of velocity at the probes depicted in Figure 5.1 is examined. As a priori the mean vortex centre is not known, the probes closest to the a posteriori determined mean vortex centre at $\frac{x-x_{vg}}{h}$ = 5 from Figure 5.5a is considered. The location of the probes correspond to $\frac{z}{h}$ = 0,1.6 and 2.4.

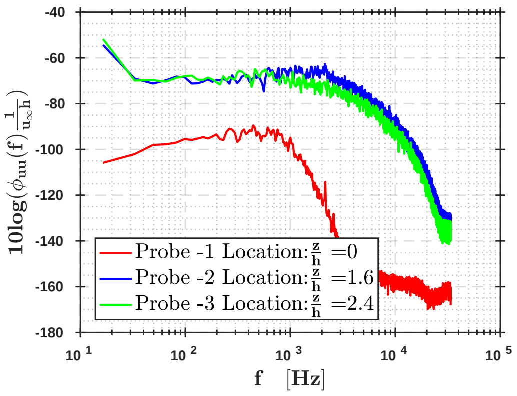

Figure 5.23: Power spectrum of the spanwise component of velocity, for RVG, $\beta = 14°$.

In Figure 5.23, the power spectrum is obtained using the pwelch function in Matlab. The resultant PSD is non-dimensionalised by $u_\infty h$ and scaled in Decibels (dB). The results indicate a broadband spectra for both Probe-2 ($\frac{z}{h}$ = 1.6) and Probe-3 ($\frac{z}{h}$ = 2.4) in comparison to the spectrum at Probe-1 ($\frac{z}{h}$ = 0). Additionally, in the spectrum for Probe-2 ($\frac{z}{h}$ = 1.6) a small increase in energy content at frequency, $f = 2137\ Hz$ is noted. Gardarin *et al.* (2008) in the study of flow separation control with VGs notes a similar trend when investigating the flow-field induced by RVGs subjected to a turbulent boundary layer in an adverse pressure gradient condition. However, in the study by Gardarin the observed dominant frequency corresponds to $f = 950Hz$, which is much lower than the frequency of the peak observed in the current study. These results, therefore, need to be interpreted with caution and will be re-visited after discussing the results for acoustics and surface pressure in the following section.

5.2.3. ACOUSTICS AND SURFACE PRESSURE PROPERTIES

For far-field acoustics, the pressure signal is predicted using the FWH-analogy implemented in PowerACOUSTICS described in Section 4.1.2. For the sound pressure level (SPL) sprectrum the location of the microphone/pressure signal is as described in section **??**. The so obtained pressure signal is further post-processed in Matlab using the pwelch funtion to obtain the PSD. This PSD is then converted to SPL using the following expression:

$$SPL = 20log(\frac{P_{rms}}{P_{ref}}) \quad \text{with,} \quad P^2_{rms} = \int_{f_1}^{f_2} PSD(f)df \tag{5.1}$$

The so obtained pressure spectrum, with $P_{ref} = 2 \times 10^5 Pa$ is as shown in Figure 5.24.

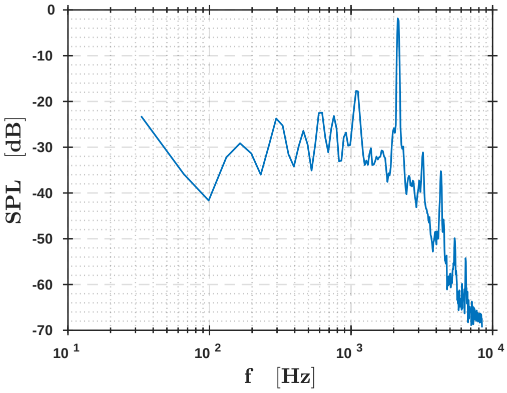

Figure 5.24: SPL Spectrum for RVG, $\beta = 14°$.

Figure 5.24 indicates to the presence of a distinctive tonal peak corresponding to frequency, $f = 2137 Hz$. A likely source, responsible for this tonal peak could be the shedding of vortices from the VG vanes. To further analyse this, the surface pressure data on the VG is bandpass filtered (BPF) between frequencies $2000 - 2400 Hz$. The standard deviation (σ_p) of the filtered pressure signal, defined in equation 5.2, is illustrated in Figure 5.25.

$$\sigma_p = \sqrt{\frac{1}{N}\sum_{i=o}^{N-1}(p(t_i) - p_{mean})^2} \qquad p_{mean} = \frac{1}{N}\sum_{i=0}^{N} p(t_i) \tag{5.2}$$

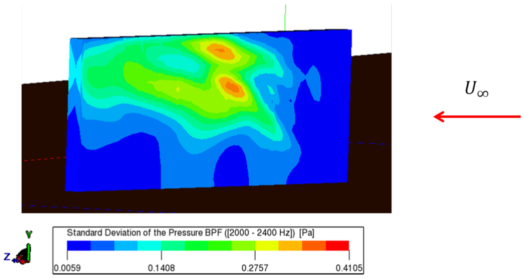
U_∞
Y
Z
Standard Deviation of the Pressure BPF ([2000 - 2400 Hz]) [Pa]
0.0059
0.1408
0.2757
0.4105

Figure 5.25: Standard deviation of the surface pressure BPF between frequencies, $f = 2000 - 2400 Hz$ on the suction side for RVG, $\beta = 14°$.

Figure 5.25 shows that, on the suction side of the VG vane, the regions dominated by the pressure fluctuations in the frequency of interest corresponds to the areas where flow curls from the pressure side to suction side. Further downstream, the magnitude of σ_p reduces. The region with reduced σ_p is seen to extend to the trailing edge of the VG vane. Thus based on the pattern of σ_p, it is likely that the tonal peak is due to the interaction of the primary vortex with the VG vane. This is affirmed by the isosurface of the λ_2 criteria in the averaged flow-field around the VG vane shown in Figure 5.26.

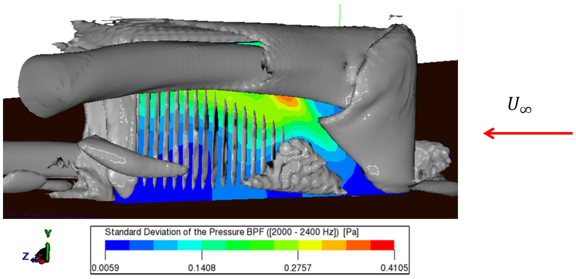
U_∞
Y
Z
Standard Deviation of the Pressure BPF ([2000 - 2400 Hz]) [Pa]
0.0059
0.1408
0.2757
0.4105

Figure 5.26: λ_2 visualisation of the averaged flow-field with standard deviation of the surface pressure BPF between frequencies, $f = 2000 - 2400Hz$.

To quantitatively observe the behaviour of the tonal noise, directivity analysis is performed. An array of 36 microphones in a circular fashion at a radial distance of $500h$ about the centre of the VG pair shown in Figure **??** is considered. The resultant directivity plot in the frequency band $2000 - 2400Hz$ is shown in Figure 5.27. you

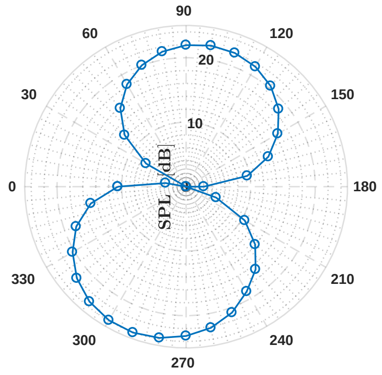

Figure 5.27: Directivity plot for RVG, $\beta = 14°$ for $f = 2000 - 2400Hz$.

Briefly, returning to the power spectrum of the spanwise component of velocity seen in Figure 5.23, the dominant frequency, $f = 2137Hz$ is identical to the frequency of the tonal peak in SPL spectrum (Figure 5.24). Further, with the results of the surface pressure distribution in Figure 5.25 indicating that this frequency is linked to the primary vortex formation and interaction with the VG vane, it is very likely that the influence of the same is being captured in the spectrum in Figure 5.23. Therefore, suggesting that the observed energy accumulation at the dominant frequency cannot be directly linked to the presence of co-operative vortex instability in the present study, unlike in case of Gardarin *et al.* (2008).

Thus based on the above results for the RVG at $\beta = 14°$ in a laminar boundary layer, the presence of co-operative instabilities which results in vortex breakdown and as a result, determines the longevity of the primary vortices, remains uncertain. However, some of the interesting observations from the mean flow-field include, the presence of the secondary vortices seen to originate at the leading edge of the VG vanes and the emergence of the various local re-circulation zones in the regions surrounding the RVG pair. Further, from the instantaneous flow results, the spanwise displacement of the primary vortices is noted to be higher than the wall normal movement. Interestingly, this unsteady movement of the vortices is seen to be influenced by the nearest neighbouring vortex. Finally, looking at the acoustic signature from the RVG vane, it found to be minimal with the highest contribution associated with the primary vortex formation.

5.3. TRIANGULAR VORTEX GENERATOR

To assess the effectiveness of Triangular VG (TVG), streamwise evolution of the flow-field is considered. In this section results for TVG vane at 14° subjected to laminar boundary layer (LBL) is presented.

5.3.1. MEAN FLOW-FIELD PROPERTIES

Starting with the mean velocity contour of the flow-field $5h$ downstream of the trailing edge of the Triangular Vortex generator (TVG) vane at $\beta = 14°$ and subjected to laminar boundary layer is as shown in Figure 5.28. The background contour indicates the axial velocity whereas, the in-plane velocity is indicated by the arrows.

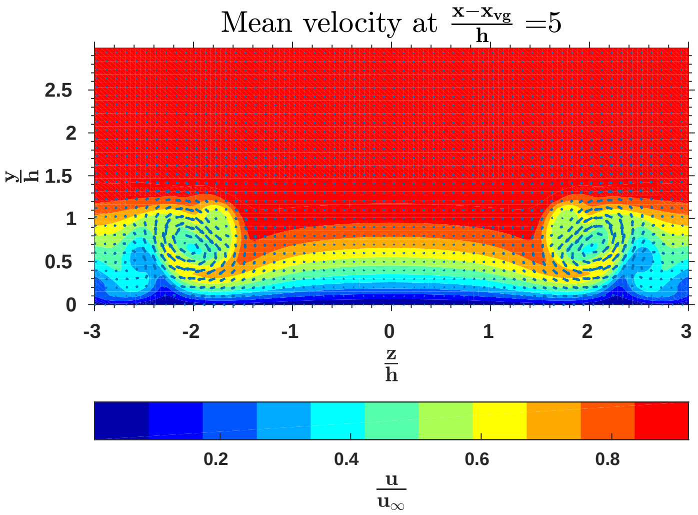

Figure 5.28: Mean flow-field at $\frac{x-x_{vg}}{h} = 5$ for TVG, $\beta = 14°$. The background contour indicates the axial velocity whereas, the in-plane velocity is indicated by the arrows.

Visually comparing the in-plane mean flow results for TVG vane from Figure 5.28 with the same for RVG vane in Figure 5.3, a distinct difference in the structure of the primary vortices is visible. Here, for the TVG vane, the vortex is seen to be more elliptical in nature and inclined at an angle to the ground. The presence of additional secondary structures (not visible in Figure 5.28) on either side of the primary vortices is anticipated to be responsible for this elliptical vortices. The mean streamwise vorticity contour shown in Figure 5.29 elucidates the presence of secondary vortices in the mean flow-field.

In Figure 5.29, the larger patches of vorticity seen in the region where elliptical vortices are visible in Figure 5.28 corresponds to the primary vortices, whereas the smaller concentric regions of opposite vorticity on either side of the primary vortices correspond to the secondary structures. Comparing the vorticity contour with that for RVG vane in Figure 5.4a, for TVG vane, vorticity is more concentrated. The downstream evolution of peak vorticity shown in Figure 5.30 illustrates this better.

Comparing the magnitude of peak vorticity in Figure 5.30, with the corresponding RVG vane in Figure 5.4b, it is interesting to note that the magnitude of peak vorticity at $\frac{x-x_{vg}}{h} = 1$ for TVG vane is almost half of the value at the same position for RVG vane. Further downstream, at $\frac{x-x_{vg}}{h} = 5$ an opposite trend, that peak vorticity for TVG vane is 2.2 times higher than that for RVG vane is observed. However, far downstream at $\frac{x-x_{vg}}{h} = 20$, the magnitude of peak vorticity is seen quite similar for both the RVG vane and TVG vane.

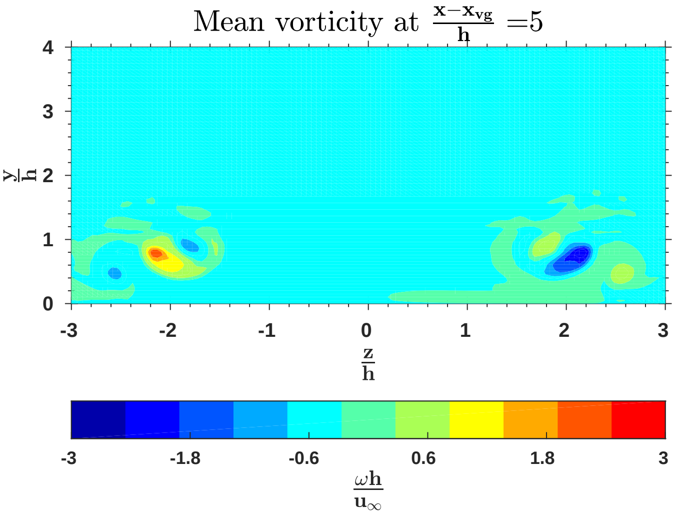

Figure 5.29: Mean streamwise vorticity at $\frac{x-x_{vg}}{h}$ = 5 for TVG, β = 14°.

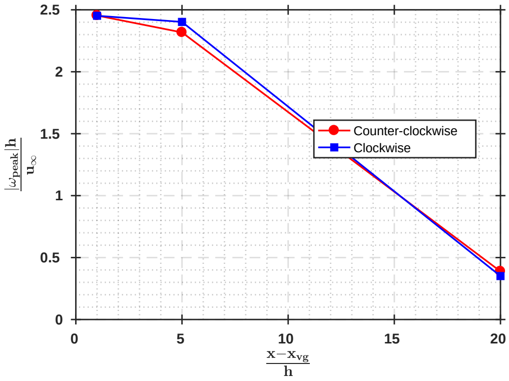

Figure 5.30: Downstream evolution of peak streamwise vorticity for TVG, β = 14°.

This interestingly suggests that, in the near wake of the TVG vane, vorticity does not decay as rapidly as in case of the RVG vane. However, it is important to remember that this might not reflect the general tendency and could only be true at the current angle of attack considered. The presence of more persistent secondary structures on either side of the primary vortices could be a possible reason for this lower rate of decay in TVGs.

The observed streamwise and wall-normal evolution of the primary vortices for the TVG vane corresponding to β = 14° and subjected to LBL is as shown in Figure 5.31.

In Figure 5.31a, the observed behaviour of the mean vortex in the spanwise direction is similar to the RVG vane in Figure 5.5a. However, in the wall normal direction, unlike in RVG vane, where the primary vortices were initially seen to move towards the wall and later away from it, here loci of vortex centres indicate that the vortices move away from the wall. Additionally, at different downstream positions considered, the primary vortices for TVG vanes, in general, is much closer to the wall. A similar observation is also noted in the study of wake characteristics of vane type VGs by Shim *et al.* (2015).

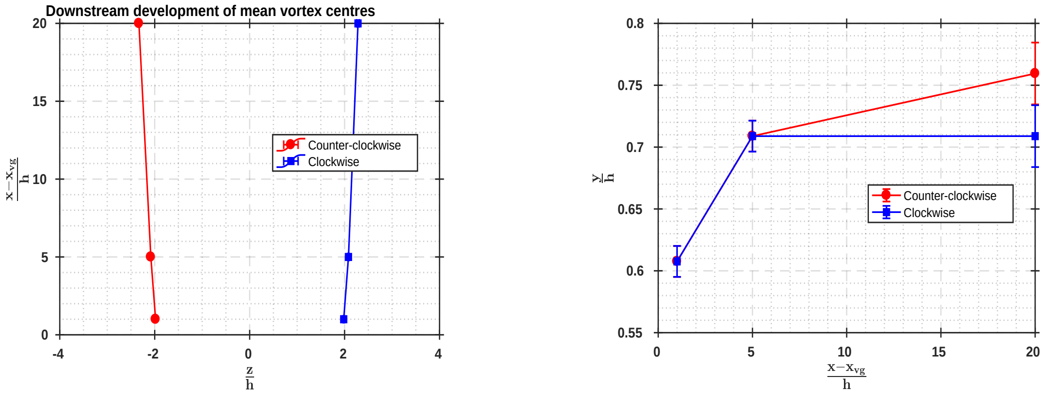

(a) Vortex centre path in the x-z plane

(b) Vortex centre path in the x-y plane

Figure 5.31: Streamwise evolution of mean vortex centre for TVG, $\beta = 14°$.

The Iso-surface of λ_2 - criteria highlighting the flow features induced by TVGs is shown in Figure 5.30.

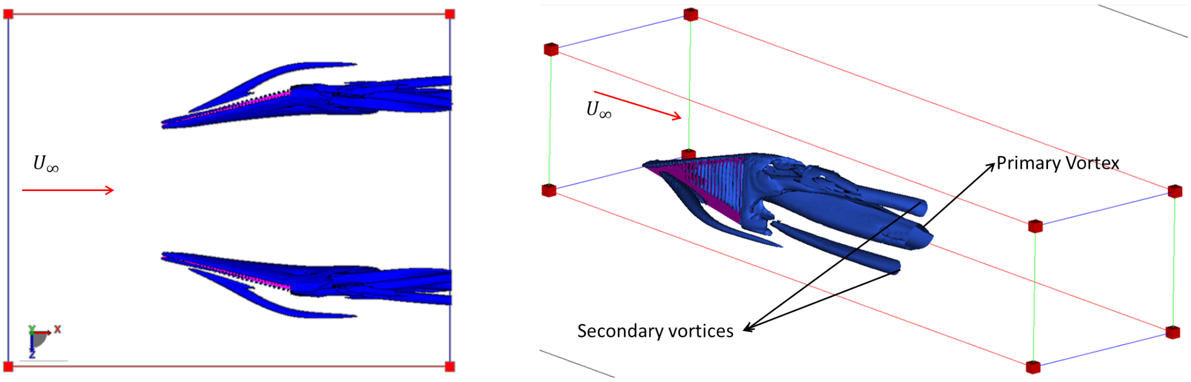

Figure 5.32: Iso-surface λ_2-criteria with a threshold of -1×10^6 illustrating primary and secoundary vortices for TVGs, $\beta = 14°$..

From Figure 5.32, it is evident that the secondary structures induced by TVG vanes are strikingly different from the corresponding structures in RVG vanes seen in Figure 5.6. Unlike, the RVG vanes, where secondary vortices are seen to originate as horseshoe vortices from the leading edge of the vane, in TVG vanes, the secondary vortices are seen to arise on the suction side of the vane and in the near wake behind trailing edge vane. The secondary structure observed on the suction side of the TVG vane is similar to the secondary vortex seen in flow over slender delta wings (Pershing, 1964). Further, looking at the local re-circulation zones, for TVG vanes there are distinct two zones visible: one near the leading edge of the vane and the other near the trailing edge of the vane as illustrated in Figure 5.33. Of the two recirculation zones, the one at the leading edge is the weaker, i.e. magnitude of the flow in this region is less than $0.5 m/s$. Visually comparing the regions with secondary structures in Figure 5.32 with the re-circulation zones indicated in Figure 5.33, the observed secondary vortex close to the wall is arising near the re-circulation zone downstream of the TVG. Similarly, Yanagihara and Torii (1993) in the study of heat-transfer augmentation by longitudinal vortices observed a secondary vortex induced downstream of the TVG vane.

Interestingly, in Figure 5.33 for TVGs no re-circulation zones is observed in between the VG vanes. This is in contrast to the previous observation of re-circulation zones for RVG vanes in Figure 5.7. The observed C_p [$C_p := \frac{P-P_{ref}}{P_{ref}}$ with, $P_{ref} = 101.325 kPa$] on the bottom surface along the $\frac{z}{h} = 0$ line is shown in Figure 5.34. Interestingly this figure indicates that the pressure gradient induced by TVG vanes is much lesser, with the

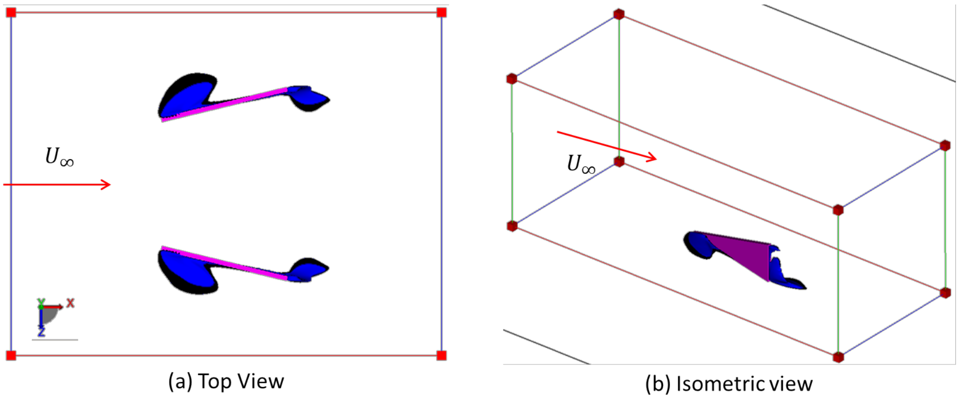

(a) Top View (b) Isometric view

Figure 5.33: Visualisation of the local re-circulation zones in the flow-field around the TVG vane, $\beta = 14°$.

rise in pressure in the streamwise direction being only 40% of the corresponding increase in pressure for the RVG vanes. Thereby, highlighting the influence of the induced pressure gradient in aiding the formation of local re-circulation zones in between the VG vanes.

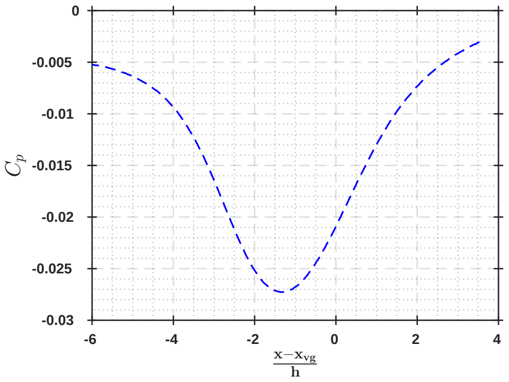

Figure 5.34: C_p along $\frac{z}{h} = 0$ for TVG vane, $\beta = 14°$.

Finally, the downstream development of the boundary layer along the $\frac{z}{h} = 0$ line, is represented in Figure 5.35. This figure shows that, as we move downstream the boundary layer is fuller. A similar observation is also noted previously in case of the RVG vanes. However, in comparison, it is seen that the velocity profile for the RVG vanes is fuller at $\frac{x-x_{vg}}{h} = 20$. Additionally, unlike the RVGs, as expected from the λ_2 visualisation, no flow reversal is noted at $\frac{x-x_{vg}}{h} = 1$.

5.3.2. INSTANTANEOUS FLOW-FIELD PROPERTIES

The velocity contour of the instantaneous flow-field $5h$ downstream of the TVG vanes at $\beta = 14°$ and subjected to LBL is shown in Figure 5.36.

Comparing the instantaneous flow-field with the corresponding mean flow-field result for TVG vanes shown in Figure 5.28, differences in the vortex structure is evident. However, interestingly it is noted that when compared to the results for RVGs for the same, the cross-correlation between the mean flow and instantaneous flow is much higher for TVGs.

Comparing the mean streamwise vorticity contour at $\frac{x-x_{vg}}{h} = 5$ in Figure 5.29 with the corresponding instantaneous streamwise vorticity contour in Figure 5.37, re-illustrates the difference between the instanta-

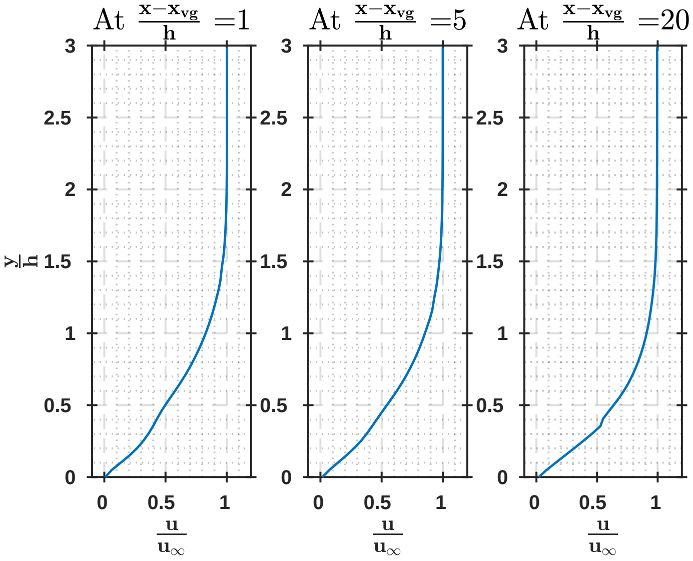

Figure 5.35: Downstream development of the mean velocity profile along $\frac{z}{h} = 0$ for TVG, $\beta = 14°$.

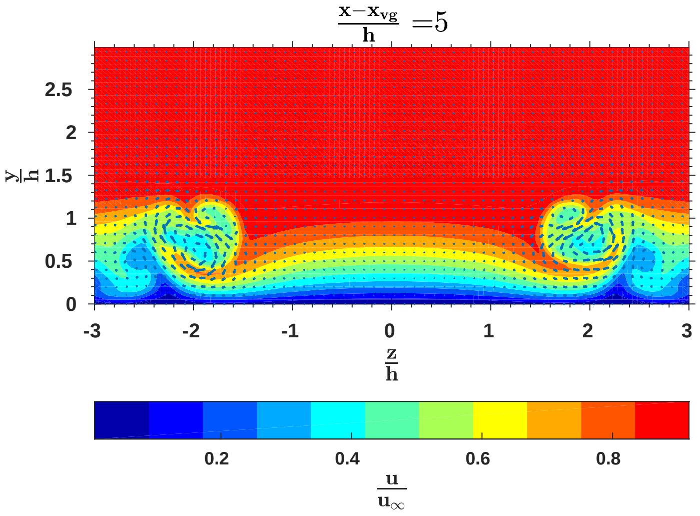

Figure 5.36: Instantaneous flow-field at $\frac{x-x_{vg}}{h} = 5$ for TVG vanes, $\beta = 14°$.The background contour represents the axial component of the velocity, whereas the arrows depict the in-plane velocity.

neous and mean flow-fields. For both the instantaneous velocity and vorticity contours presented in Figure 5.36 and Figure 5.37, the data corresponds to a time instant, $t = 0.25s$.

Having already established that vortices induced by RVGs are unsteady, a similar behaviour is anticipated for vortices induced other VG profile as well. With this in mind, the various instantaneous vortex centres identified at downstream position $\frac{x-x_{vg}}{h} = 5$, using the modified criteria (see Section 4.4.6) as a function of time is as shown in Figure 5.38.

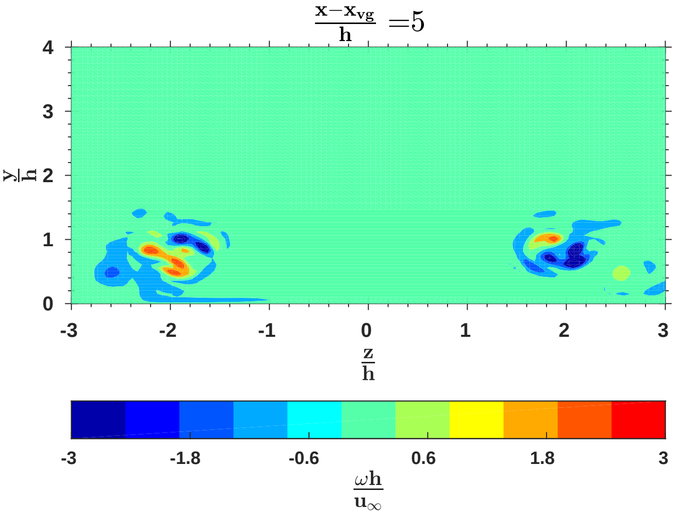

Figure 5.37: Instantaneous streamwise vorticity in the flow-field at $\frac{x-x_{vg}}{h}=5$ for TVG vanes, $\beta=14°$.

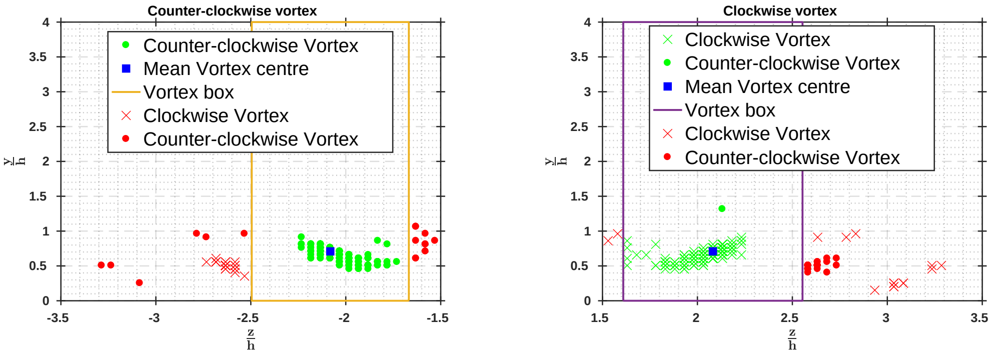

(a) Counter-clockwise vortex centres.

(b) Clockwise vortex centres.

Figure 5.38: Instantaneous vortex centres for TVG vanes, $\beta=14°$ at $\frac{x-x_{vg}}{h}=5$.

In Figure 5.38, the clockwise vortices are indicated by crosses (×) and the counter-clockwise vortices by dots (●). In addition to the expected primary counter-clockwise and clockwise vortices in Figure 5.38a and Figure 5.38b respectively, additional opposite signed vortices are also observed. Comparing the average position of the cluster of oppositely signed vortices with the mean vorticity contour in Figure 5.29, it is found that these clusters correspond to the secondary vortices. These secondary vortices are also identified most likely because, at certain instants, the primary vortex may be distorted, which results in the secondary structures conforming better with the applied modified criteria.

The instantaneous counter clockwise vortex centres represented by the green dots in Figure 5.38a, are considered to be associated with the primary counter-clockwise vortex. These vortex centres are seen to be enclosed in the depicted vortex box separating the different vortex structures. Based on trial and error, the width of this vortex box for the current case is found to be 2.25 times the standard deviation (obtained by considering all the identified vortex centres) about the mean vortex centre. With a similar approach for the instantaneous clockwise vortex centres represented by the green crosses, the observed vortex kinematics in terms of the spanwise and wall-normal displacement of the counter-clockwise and clockwise vortices about the mean vortex centre is as shown in Figure 5.39 and Figure 5.40 respectively.

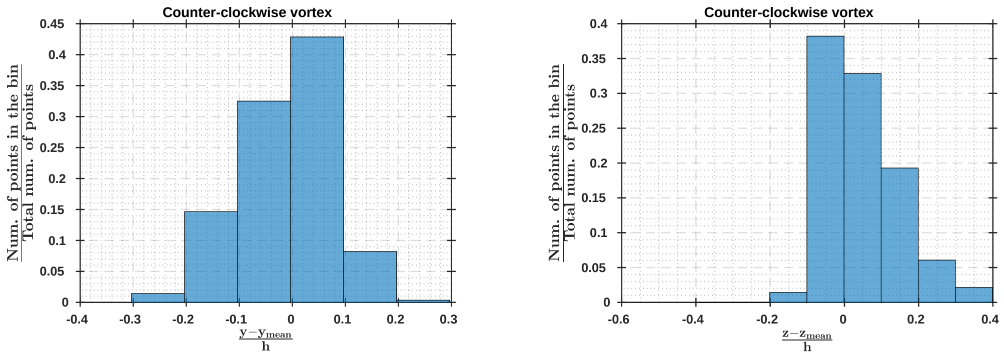

(a) Wall-normal vortex displacement

(b) Spanwise vortex displacemnet

Figure 5.39: Wall-normal and spanwise displacement of the primary counter-clockwise vortex for TVG vanes, $\beta = 14°$ at $\frac{x - x_{vg}}{h} = 5$.

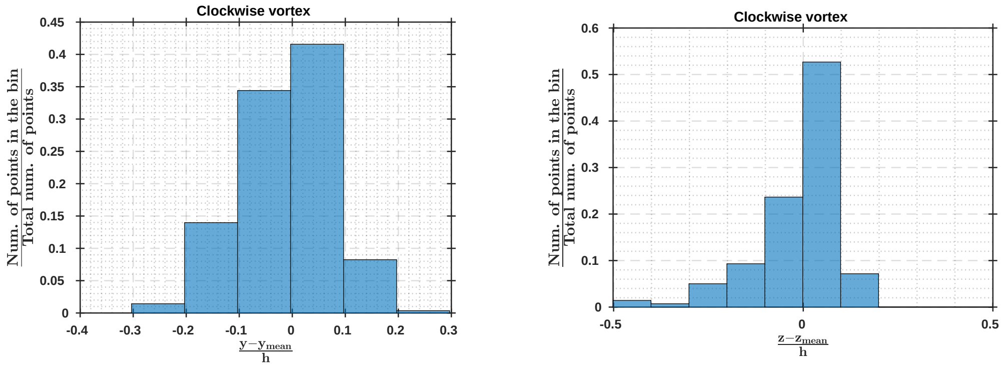

(a) Wall-normal vortex displacement

(b) Spanwise vortex displacemnet

Figure 5.40: Wall-normal and spanwise displacement of the primary clockwise vortex for TVG vanes, $\beta = 14°$ at $\frac{x - x_{vg}}{h} = 5$.

From Figure 5.39 and Figure 5.40, for both primary clockwise and counter-clockwise vortices, although minimal, the displacement of the vortex in the spanwise direction is greater than the displacement in the wall-normal direction. In case of the counter-clockwise vortex, the approximate displacement in the wall-normal and spanwise direction is $0.5h$ and $0.6h$ respectively. Similarly, for the clockwise vortex, the displacement in the wall-normal and spanwise directions is $0.5h$ and $0.7h$ respectively. Interestingly, comparing these values with the magnitude of displacement for the RVG vanes shows that, the displacement for TVGs is only half of that for the RVG vanes at $\frac{x - x_{vg}}{h} = 5$. The reason for this reduction in the magnitude of displacement of the primary vortices for the TVGs is not very clear. A possible explanation could be due to the concentrated nature of vorticity at the centre of vortices induced by TVGs, previously noted in the mean flow results.

From the cluster of the primary vortex centres identified in Figure 5.39 the observed probability density function (PDF) indicating the most likely position of the vortex at any given instant is shown in Figure 5.41.

Comparing the PDF for the primary vortices from TVG vanes with the corresponding PDF contour for the RVG vanes in FIgure 5.17, the distinct elliptical nature of PDF the for TVGs is evident. Having already observed that a major difference in the flow-field induced by the TVG vanes and the RVG vanes is the presence of more

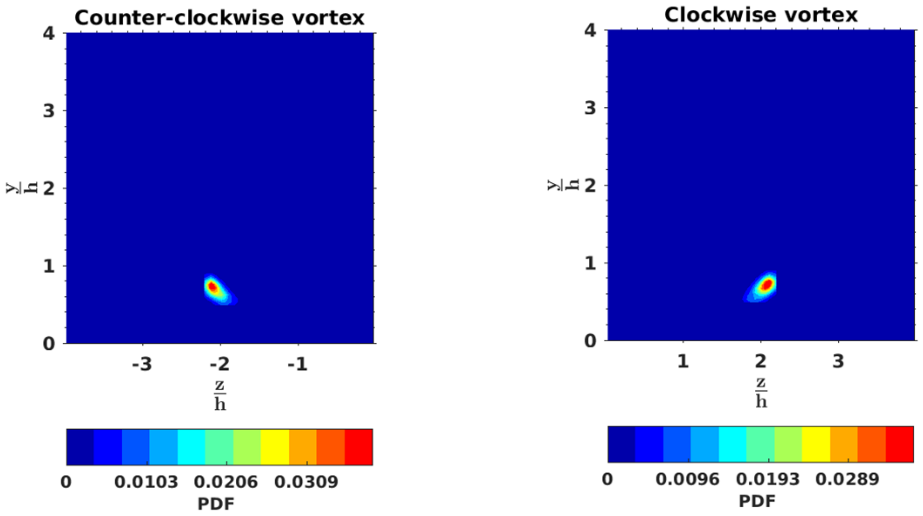

(a) Counter-clockwise vortex. (b) Clockwise vortex.

Figure 5.41: PDF of instantaneous vortex centres for TVG vanes, $\beta = 14°$ at $\frac{x-x_{vg}}{h} = 5$.

persistence secondary structures, the PDF in Figure 5.41 can be considered as an illustration of the influence of the secondary structures.

Similar to the RVG case, the preferred direction of motion (θ_{eig}) of the primary vortices and the magnitude of meandering at different downstream positions for the TVG vanes is shown in Figure 5.42.

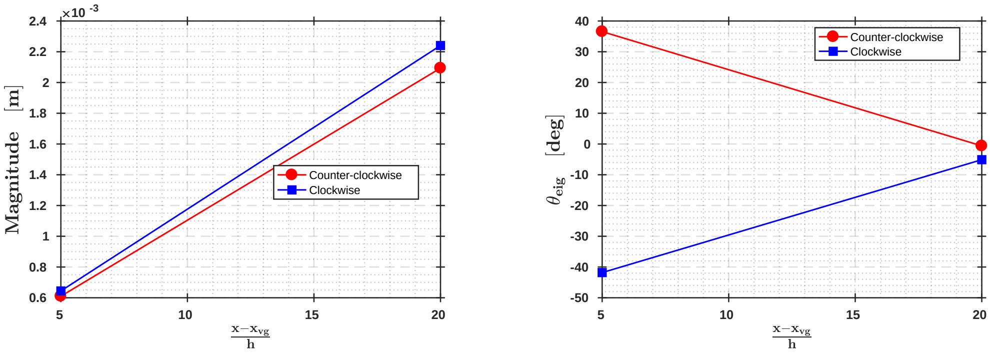

(a) Variation of the magnitude of meandering along the preferred direction with downstream positions.

(b) Variation of chracteristic angle, θ_{eig} with downstream positions.

Figure 5.42: Meandering characteristics for TVG, $\beta = 14°$.

From Figure 5.42a, moving downstream from $\frac{x-x_{vg}}{h} = 5$ to 20, the magnitude of meandering is seen to increase, similar to the trend previously observed for the RVG vanes. The ratio of the magnitude of meandering between the TVG vanes and RVG vanes at $\frac{x-x_{vg}}{h} = 5$, is 0.5. However, at $\frac{x-x_{vg}}{h} = 20$, the ratio increases to approximately 0.73. Thereby, suggesting that the rate of increase in meandering is higher for the TVGs than RVGs at $\beta = 14°$.

Moving to the preferred direction of motion seen in Figure 5.42b, the magnitude of θ_{eig} reduces for both the clockwise and counter-counter clockwise vortices. This trend is similar to that observed for the RVG vanes. However, comparing the angles, θ_{eig} is significantly different, which is due to the difference in the flow-field induced by the VG vanes. In Figure 5.42, the results for the both the magnitude of meandering and preferred direction of motion at $\frac{x-x_{vg}}{h} = 1$ is not presented. This is because it was not possible to distinguish the primary vortices from the multiple structures induced by the TVG vanes. This highlights the shortcoming in the currently employed algorithm using the modified criteria, which fails to identify the dominant vortex structure in the presence of multiple structures in proximity.

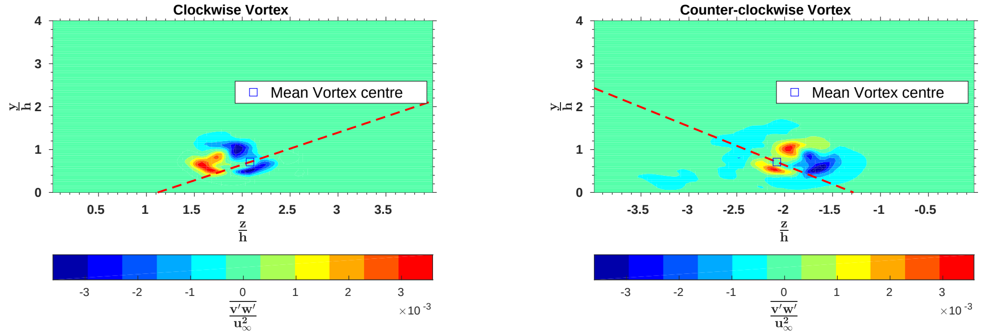

Figure 5.43: Axis of preferred direction of motion (dashed red line) overlapping the distribution of Reynolds shear stress, $\overline{v'w'}$ for TVG , $\beta = 14°$ at $\frac{x-x_{vg}}{h} = 5$.

The results obtained by overlapping the preferred direction of motion with the in-plane Reynolds Shear Stress (RSS), $\overline{v'w'}$ at $\frac{x-x_{vg}}{h} = 5$, is shown in Figure 5.43. It is evident that the RSS distribution is not uniformly four lobed as in Figure 5.21, but is rather deformed such that, there are two positive signed lobes and only one negative signed lobe for counter-clockwise vortex and vice versa for the clockwise vortex. Interestingly, contrary to RVG vanes where the preferred direction of motion (dashed red lines in FIgure 5.43) was seen to be in-line with the dominant lobes, here the preferred direction of motion of vortex is seen to be rather in-line with the minor lobe.

As in case of RVG vanes, the power spectrum of the spanwise component of velocity for TVG vanes is considered to further analyse the possibility of presence co-operative instabilities. As a priori the vortex centre position is not known, probes closest to the primary vortex (clockwise vortex) are considered. Based on previous mean flow-field results in Figure 5.31a the location of the probes correspond to $\frac{z}{h} = 0, 1.6$ and 2.4.

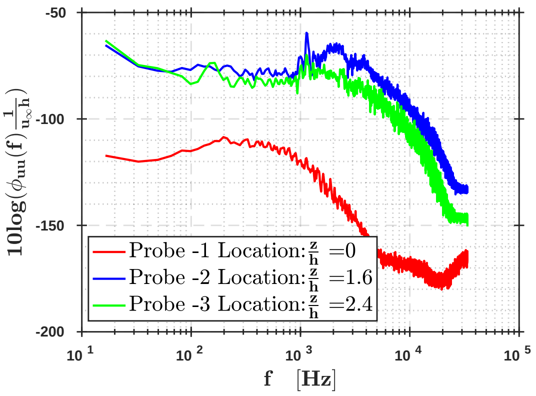

Figure 5.44: Power spectrum of the spanwise component of velocity, TVG $\beta = 14°$.

In Figure 5.44, the power spectrum is obtained using the pwelch function in Matlab. The resultant PSD is non-dimensionalised by $u_\infty h$ and scaled in Decibels (dB). Interestingly, in Figure 5.44 for Probes -2 and 3, there are two distinct dominant frequency zones: one tonal in nature occurring at frequency, $f = 1151\ Hz$ and the other corresponding to a more gradual accumulation of energy in frequencies ranging from approximately, 1600 Hz to 2600 Hz.

To further analyse the behaviour of the dominant frequencies from Figure 5.44 in time, based the study of wavelet analysis for unsteady flow by Indrusiak and Möller (2011), the technique of continuous wavelet transformation (CWT) is employed. To this end, the cwt function in Matlab is used with the analytic 'Morlet' wavelet as the character/basis wavelet. Essentially, in CWT the given signal is compared with a scaled and shifted character wavelet (Morlet wavelet). Thus, based on the properties of the character wavelet that matches with the input signal the best, an overview of the energy distribution in both time and frequency domain is obtained. The resultant spectrogram of the velocity time series considered for Probe-2 and Probe-3 is shown in Figure 5.45.

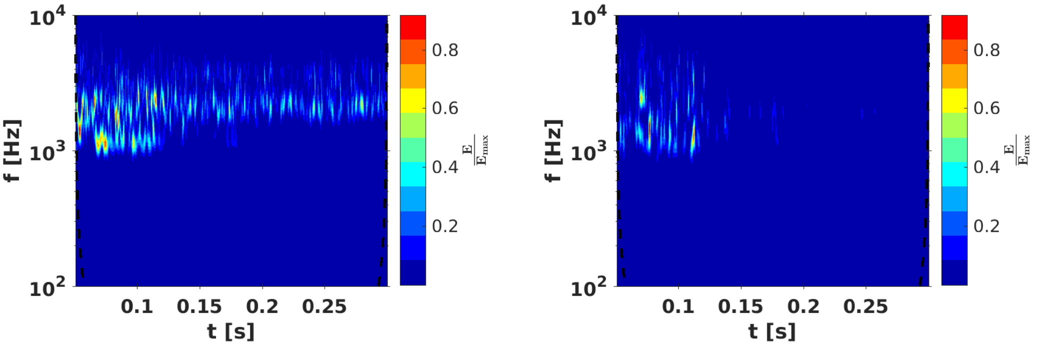

(a) Probe-2.

(b) Probe-3.

Figure 5.45: Spectrogram for Probe-2 and Probe-3, TVG vanes, $\beta = 14°$.

In both Figure 5.45a and Figure 5.45b the energy distribution (E) is non-dimensionalised by their respective maximum values (E_{max}). As is expected, the spectrograms indicate higher energy content in the previously observed dominant frequencies. Interestingly, in both Figure 5.45a and Figure 5.45b the energy content at frequency associated with the tonal peak is dominant only initially, till time $t \approx 0.125s$. Beyond this, the energy distribution at this frequency is sparse. As a result, it is highly likely that the oscillations associated with this frequency could be an artefact of the flow startup process. On the other hand, contrary to this the energy in dominant frequency range observed between, $f = 1600 - 2600 Hz$ is consistent in time. The implication of this is further discussed after the acoustic and surface pressure results in the following section.

5.3.3. ACOUSTICS AND SURFACE PRESSURE PROPERTIES

The far-field acoustics for the TVG vane is computed at a position $500h$ ($2.5m$) directly above the centre of the TVG pair as indicated in Figure 5.2. The resultant Sound Pressure Level (SPL) spectrum for the TVG is as shown in Figure 5.46.

In Figure 5.46, the energy content in the acoustic pressure fluctuations is concentrated in the frequency range, $f < 2000Hz$ with the maximum occurring at $f = 624Hz$. Comparing this with the spectrum for the RVG vanes in Figure 5.24, it is possible to make following observations. First, unlike in RVG vanes, no evidence of a similar strong tonal peak is visible for TVG vanes. Secondly comparing the magnitude of SPL, on an average, the acoustic radiation from the TVG vanes is lower, especially at $f > 1000Hz$.

To further ascertain the possible cause for the maximum in Figure 5.46 at $f = 624Hz$, the standard deviation of the surface pressure bandpass filtered (BPF) between frequencies $400 - 800Hz$ as shown in Figure 5.47 is considered.

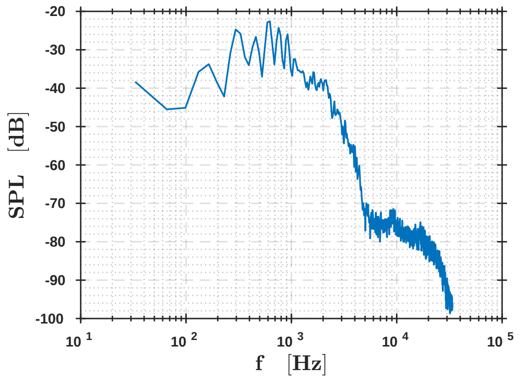

Figure 5.46: SPL Spectrum for TVG, $\beta = 14°$.

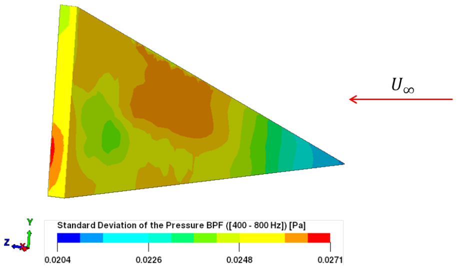

Figure 5.47: Standard deviation of the surface pressure BPF between frequencies, $f = 400 - 800 Hz$ on the suction side for TVG, $\beta = 14°$.

From Figure 5.47, two distinctive regions with a higher standard deviation of the filtered surface pressure is noted. Concurrently considering the λ_2 visualisation of the mean flow-field around the vane, shown in Figure 5.48, the observed regions of high standard deviation are seen to be associated with the formation of the secondary vortices. Finally, for the directivity plot, at the frequency of interest ($400-800 Hz$), the resultant SPL values are found to be less than zero for all the microphones considered and hence not shown here. The setup of the microphone array is shown in Figure 5.2.

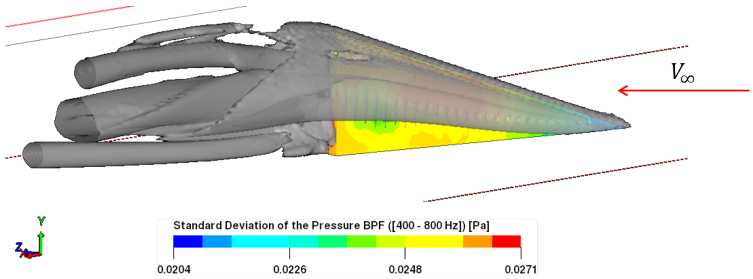
V_∞
Y
Z
Standard Deviation of the Pressure BPF ([400 - 800 Hz]) [Pa]
0.0204
0.0226
0.0248
0.0271

Figure 5.48: λ_2 visualisation of the averaged flow-field with standard deviation of the surface pressure BPF between frequencies, $f = 400 - 800 Hz$ on the suction side for TVG, $\beta = 14°$.

Returning the SPL spectrum in Figure 5.46, in the frequency range, $f = 1600 - 2600$ no energy peak is evident. This is in contrast to the observed energy accumulation at this frequency range in the power spectrum of the probes in Figure 5.44. Therefore this is interpreted as an indication that this frequency range is not associated with the vortex formation or interaction with the VG vane. As a result, we can say that these frequencies are more likely to have originated downstream of the VG vane due to the induced vortex system. One such possibility is due to vortex instabilities. Considering that the primary vortex is seen to be under the straining influence of two secondary vortices, which can trigger instabilities, the presence of vortex instability can not be ruled out. Nevertheless, a more detailed stability analysis would be required to definitively confirm if these frequencies are associated with some form of vortex instabilities.

Based on the above results the induced flow-field for the TVGs at $\beta = 14°$ and subjected to a LBL is found to very different from the previously observed flow-field for the RVGs. The most notable change is with regards to the position, direction of rotation and number of secondary vortices. For RVGs just aft of the vane we have one secondary vortex with the same direction of rotation as the primary vortex. However, for TVGs two secondary vortices with the direction of rotation opposite to that of the primary vortex are noted. Further, at this angle of attack, local re-circulation zones are limited to the leading edge and trailing edge for TVGs. However, in case of the RVGs additional local recirculation zones is also observed in between the vanes. The both RVGs and TVGs magnitude of meandering increases with the downstream position, but the values are higher for vortices induced by RVGs. Interestingly, due to the observed vortex system for TVGs at this angle of attack, the possibility of presence vortex instability is higher for TVGs. Lastly, looking at the acoustic far-field spectra, although for both the VGs far-field noise is minimal, TVGs are seen to be comparatively less noisy.

5.4. INFLUENCE OF CHANGE IN ANGLE OF ATTACK THE VG

In this section, to assess the variation of flow-field properties with the change in angle of attack of the VG vane (β), four angles $\beta = 8°, 14°, 20°$ and $30°$ is selected. Results for Rectangular vortex generators (RVGs) are first discussed followed by the results for the Triangular vortex generators (TVGs). In the current study, β is changed by maintaining the distance between the leading edges of the VG pair constant (see Figure 4.3). Consequently, the distance between vortices from neighbouring VG pairs reduces with an increase in angle of attack.

5.4.1. RECTANGULAR VORTEX GENERATOR

MEAN FLOW-FIELD PROPERTIES

Starting with the downstream evolution of peak streamwise vorticity, the variation with change β is shown in Figure 5.49.

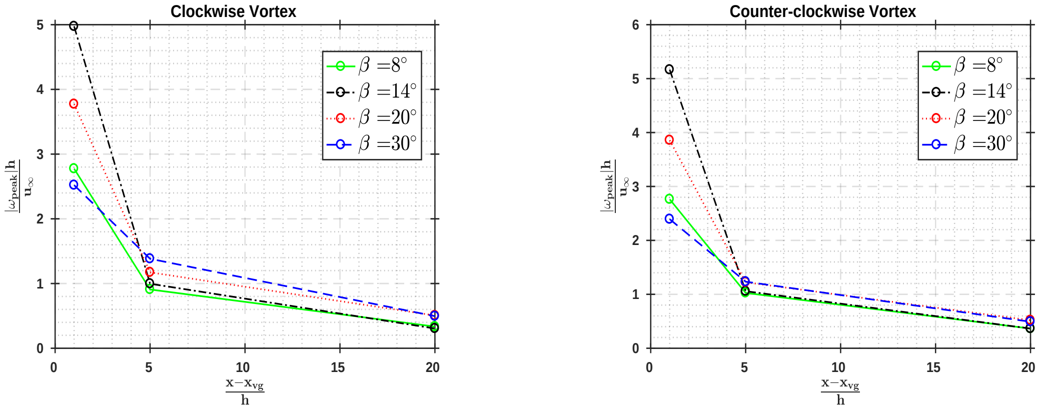

(a) Clockwise Vortex

(b) Counter-clockwise Vortex

Figure 5.49: Streamwise evolution $|\omega_{peak}|$ for RVGs at various β.

Interestingly, in Figure 5.49 for both the clockwise and counter-clockwise vortices at $\frac{x-x_{vg}}{h} = 1$, the peak streamwise vorticity ($|\omega_{peak}|$) is not maximum at the highest angle of attack. In fact, $|\omega_{peak}|$ is maximum for RVGs at $\beta = 14°$, in the plane closest to the vanes . This result indicates that the peak vorticity initially increases with an increase in β from 8° to 14° but with further increase in β to 20° and 30°, $|\omega_{peak}|$ decreases. A possible explanation for this trend in $|\omega_{peak}|$ is due to the enhanced interaction between the secondary structures and the primary vortex. In the mean flow (not shown here), with the increase in β, the secondary structures are seen to be bigger and more prominent. The interaction with this more prominent secondary vortices leads to larger primary vortices with diffused vorticity. Shim *et al.* (2015), in investigating the wake-characteristics of RVGs, notes of a similar peak vorticity trend for laminar boundary layer flow with increase in angle of attack. They also mention that the observed drop in $|\omega_{peak}|$ is due to the interaction of the secondary horseshoe vortex with the primary vortex.

Further in Figure 5.49 comparing the decay of $|\omega_{peak}|$ for different β, it is highest at $\beta = 14°$ and decreases with further increase in β. However, at downstream position $\frac{x-x_{vg}}{h} = 20$, $|\omega_{peak}|$ is almost identical for all β. Comparing these results with the measurement in Shim *et al.* (2015), the observed rate of decay in the current study is seen to be higher. This is likely due to the difference in the wall-normal position of the primary vortices resulting from the difference in VG configuration between the two studies. In Shim *et al.* (2015), the primary vortex in the mean flow is farther away from the wall than in the current study. Consequently, in the present study, the proximity of the vortices to the wall is expected to increase the rate of decay.

The comparison of the mean streamwise vorticity contours at $\frac{x-x_{vg}}{h} = 5$ is shown in Figure 5.50.

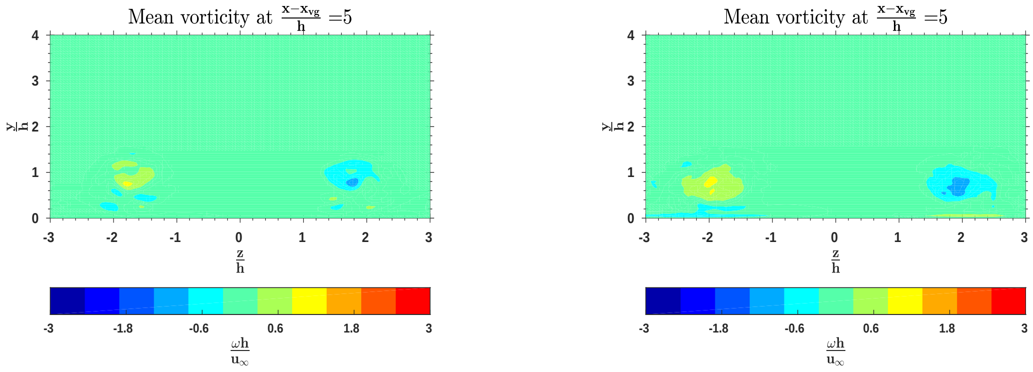

(a) $\beta = 8°$

(b) $\beta = 14°$

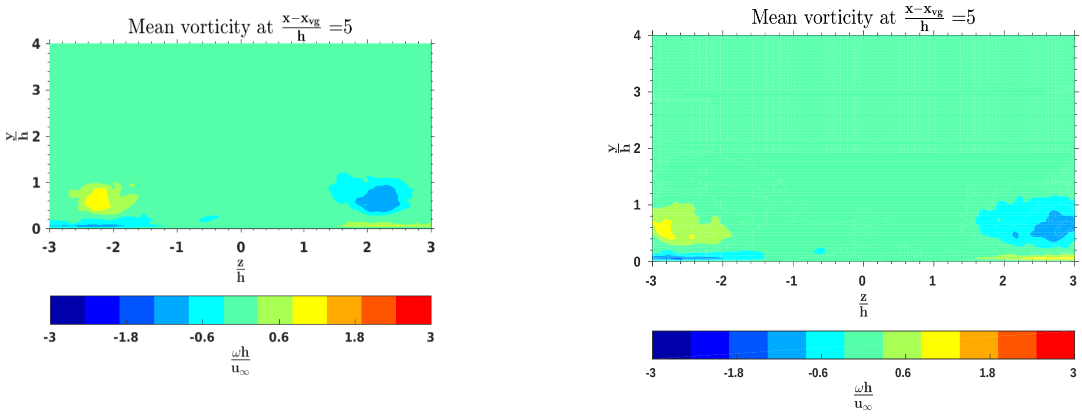

(c) $\beta = 20°$

(d) $\beta = 30°$

Figure 5.50: Streamwise vorticity contour at $\frac{x-x_{vg}}{h} = 5$ for for RVGs at various β.

In Figure 5.50, with increasing β vorticity is seen to be more diffused at a constant downstream position. Thereby, symbolising that increasing β results larger more diffused vortices. The corresponding circulation (Γ), for these vortices, is shown in Figure 5.51. Circulation is defined as the negative line integral of velocity around a closed curve. Here, the circulation of the vortex is computed by integrating along box $5mm$ x $5mm$

centred at the mean vortex centre, according to

$$\Gamma = -\oint_l v(x)dx \tag{5.3}$$

where v is the component of velocity tangential to the line.

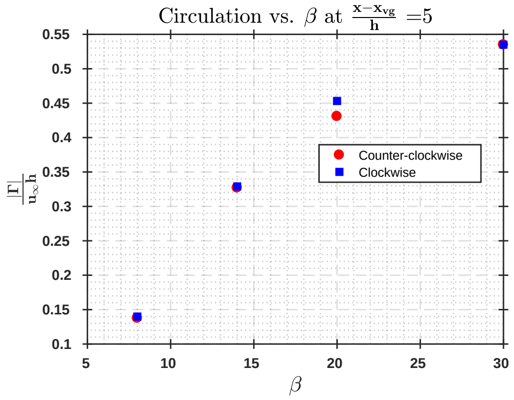

Figure 5.51: Variation in vortex circulation for RVGs with change in β at $\frac{x-x_{vg}}{h} = 5$.

It is evident from Figure 5.51 that with an increase in the β the circulation the primary vortex also increases. Thereby, confirming that the observed larger vortices in Figure 5.50 are stronger as well. In the investigation of the helical structure of vortices embedded in a turbulent wall bound flow by Velte *et al.* (2009), with an increase in β, circulation is shown to increase linearly. However, a similar deduction from Figure 5.51 is not possible as the method employed here is relatively crude. Alternate approaches were attempted, however, due to the proximity of the secondary vortex none of them yielded the desired results.

Turning now to the downstream development of the spanwise averaged mean boundary layer profile, shown in Figure 5.52. It is observed that, with an increase in β, the boundary layer profile is seen to be fuller at the downstream position, $\frac{x-x_{vg}}{h} = 20$. Using the shape factor (H) defined in equation (2.3) as an indicator of the boundary layer state, the observed variation in downstream evolution of H for different β is shown in Figure 5.52b. At the downstream position $\frac{x-x_{vg}}{h} = 20$, for all angle of attack of the RVG vane the boundary layer profile based on value of H can be considered as turbulent (for turbulent profile $H = 1.3-2$). In constrast, at the downstream position closest to the RVG vane ($\frac{x-x_{vg}}{h} = 1$), as β is increased H also increases. At $\beta = 30°$, $H = 3.75$ which indicated of possible flow separation (for separated profile $H > 3.5$).

To further examine the occurrence of flow separation, Iso-Surface of the streamwise component of velocity lesser than zero in a region surrounding the VG vanes, shown in Figure 5.53 is considered. It is evident that, with increase in β, the various local recirculation zones previously identified for the RVG at $\beta = 14°$ in Section 5.2.1, appears to grow. The most notable increase in the re-circulation zones is seen between the VG vanes. This is likely so because, with an increase in β, the vortex strength and size as previously seen, also increases. As a result, it is possible that this stronger vortex can exert a greater influence to entrap flow in between the vanes, thereby aiding the formation of the recirculation zone.

Another parameter which could aid in the formation of recirculation zone is the pressure gradient induced in the flow-field, due to the presence of the VG vanes. In Figure 5.54, the C_p [$C_p := \frac{P-P_{ref}}{P_{ref}}$ with, $P_{ref} = 101.325kPa$] for various β along the bottom surface at $\frac{z}{h} = 0$ is presented. The presence of a pressure gradient is noted, with peak C_p reducing with an increase in device angle, resulting in higher pressure gradient at higher β. This is interesting because, in the current study, a flat plate, corresponding to an external zero pressure gradient scenario is simulated. However, when considering VGs on airfoils, it important to remember that an additional external adverse pressure gradient is also present. Therefore, the pressure

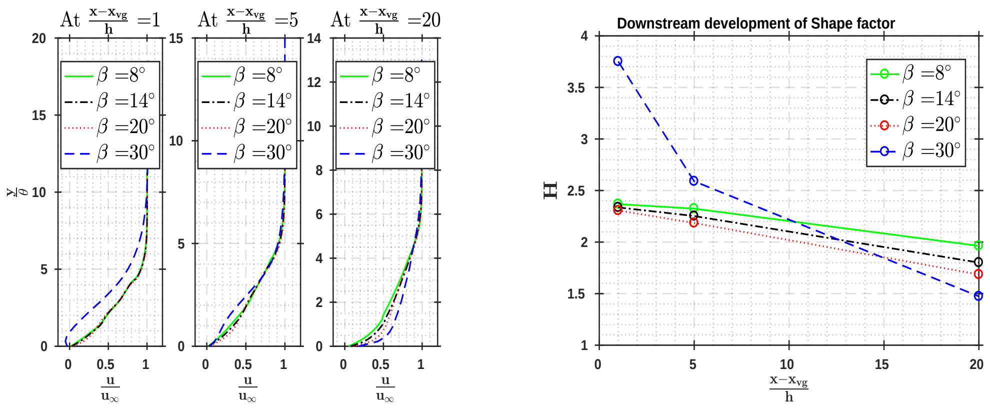

(a) Velocity profile

(b) Shape factor

Figure 5.52: Downstream development of the mean velocity profile and the associated shape factor, H along $\frac{z}{h} = 0$ for RVG, at different β.

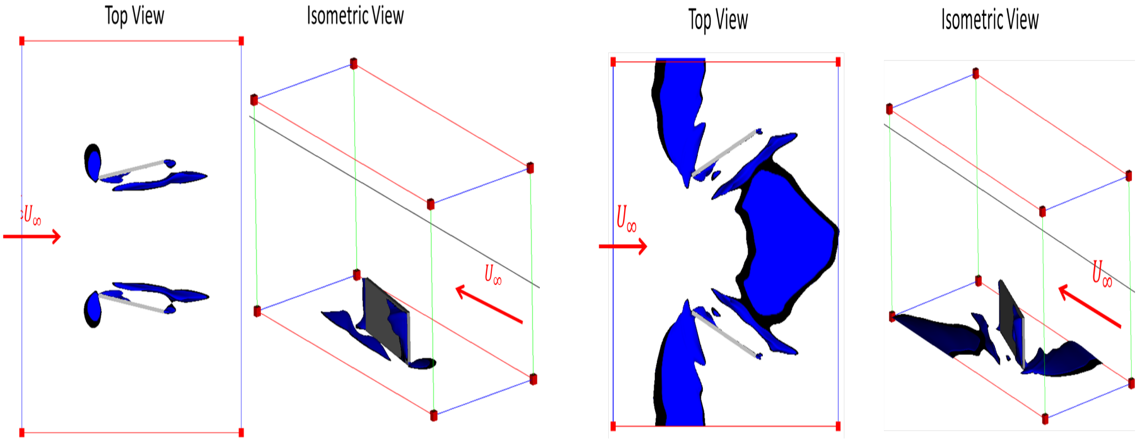
Top View
Isometric View
U_∞
Top View
Isometric View
U_∞

(a) At $\beta = 8°$

(b) At $\beta = 20°$

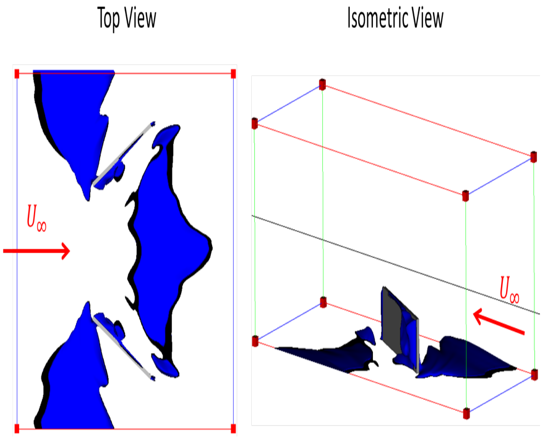
Top View
Isometric View
U_∞

(c) At $\beta = 30°$

Figure 5.53: Iso-Surface of streamwise component of velocity lesser than zero for different β.

gradient induced by the VGs can augment to the existing pressure gradient have a more detrimental effect for VGs at higher β angles.

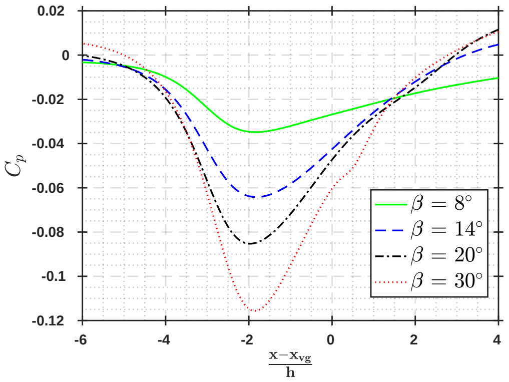

Figure 5.54: C_p along bottom surface at $\frac{z}{h}$ = 0 for RVG for various β.

INSTANTANEOUS FLOW-FIELD PROPERTIES

The observed variation in the magnitude of meandering and preferred direction of motion of the primary vortices at downstream position $\frac{x-x_{vg}}{h}$ = 5 for different β is shown in Figure 5.55.

From Figure 5.55a, with an increase in the angle of attack, the magnitude of meandering also increase. This could be because the size of the vortex is seen to be increasing with β at the downstream position $\frac{x-x_{vg}}{h}$ = 5. Therefore, the observed magnitude of meandering for the different cases is divided by the radius of the corresponding mean flow-field vortex to obtain a relative magnitude of meandering. From Figure 5.55b, the observed relative meandering is maximum for the RVG vane at $\beta = 8°$. It is to be noted here that the vortex radius is computed manually based on the velocity contour in the mean flow-field. Interestingly, for the other three angles of attack, the magnitude of relative meandering is quite similar. Consequently, suggesting that the likelihood of the presence of vortex instability in the primary vortices is higher at the lower angles of attack for the RVGs. Moving now to Figure 5.55c, based on the previous observation on the behaviour θ_{eig} for the RVG vane at $\beta = 14°$ the observed θ_{eig} values for the primary vortices in Figure 5.55c is a result of the influence of the dominant neighbouring vortex.

To further assess the presence of instabilities, power spectrum of the spanwise component of velocity at $\frac{x-x_{vg}}{h}$ = 5 for different β shown in Figure 5.56 is considered.

Comparing the power spectra for the different angles of attack, interestingly, at $\beta = 8°$ a distinct sharp peak at the frequency, $f = 1685Hz$ is visible. In contrast, for all other angles of attack, a gradual increase in energy leading up to a dominant frequency is noted. The dominant frequencies are approximately $2137Hz$, $1447Hz$ and $970Hz$ for $\beta = 14°$, 20° and 30° respectively. This is interesting because, the observed similarity in the spectral trends for $\beta = 14°$, 20° and 30° indicates of almost identical vortex behaviour with different dominant frequency. This is probably the reason for the observed similar relative meandering in Figure 5.55b, especially for $\beta = 14°$ and 20°.

The observed Sound Pressure Level (SPL) spectra for RVGs at different angle of attack of the VG vane is shown in Figure 5.57. The location of the microphone used for the SPL spectra is as previous described in Section 5.1.

Figure 5.57, indicates to the presence of multiple tonal peaks at various distinctive frequencies for the different angles of attack of the RVG vane. The frequency of the most dominant peaks correspond the f =

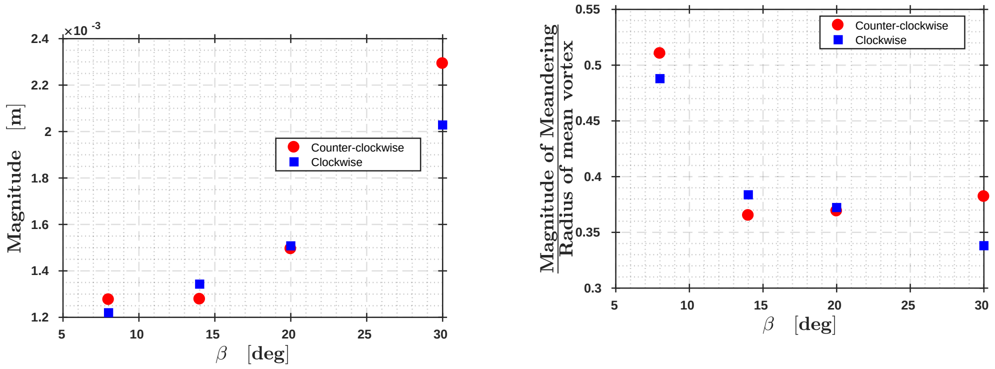

(a) Variation of the magnitude of meandering.

(b) Variation of the magnitude of meandering with respect to the corresponding mean vortex radius.

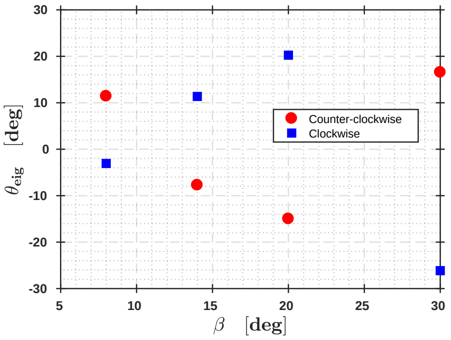

(c) Variation of chracteristic angle, θ_{eig}.

Figure 5.55: Variation of meandering characteristics for RVG with change in β at $\frac{x - x_{vg}}{h} = 5$.

$1677Hz, 2137Hz, 2532Hz$ and $2170Hz$ for $\beta = 8°, 14°, 20°$ and $30°$ respectively. The Overall Sound Pressure Level (OASPL), which is indicative of the total energy content in the signal, is defined as:

$$OASPL = 20log(\frac{P_{rms}}{P_{ref}}) \quad \text{with,} \quad P_{rms}^2 = \int_0^{\infty} PSD(f)df \tag{5.4}$$

The so computed OASPL from the SPL spectra for different β is tabulated in Table 5.1. With increase in β it the acoustic energy at this microphone position also increases.

β	8°	14°	20°	30°
OSPL [dB]	-11.08	1.96	3	4.54

Table 5.1: Variation of OSPL with β for RVG.

Returning to the observed dominant frequencies in the power spectrum of the spanwise component of velocity in Figure 5.56, for all β, at almost identical frequencies, peaks (not necessarily the most dominant) are seen in the SPL spectrum in Figure 5.57. As a result, using a similar argument as before, it is more likely that the dominant frequencies from Figure 5.56 are linked to vortex formation and interaction of the vortex with the VG vane. However, interestingly in case of the RVG at $\beta = 8°$ from Figure 5.56 it is seen that, there are additional frequencies with energy peaks visible as well, the origin of which is not clear. Considering this, together with fact that observed relative meandering from Figure 5.55b is highest for RVG vane at $\beta = 8°$, it can be said that the probability of presence of vortex instability is higher at this β when compared to the other angles of attack considered in the current study.

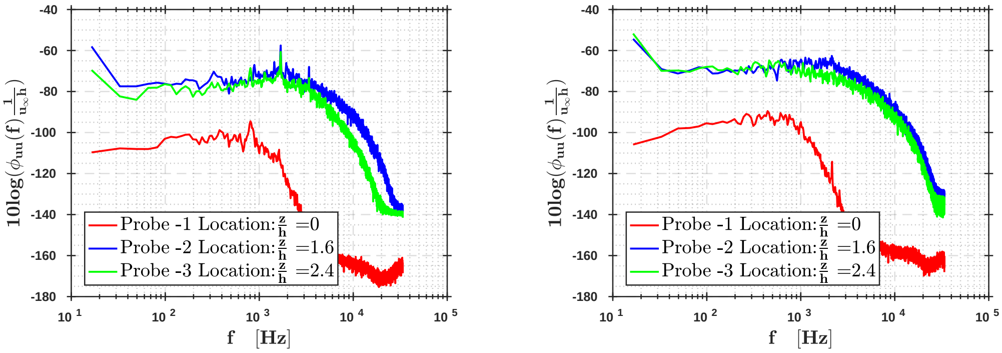

(a) $\beta = 8°$.

(b) $\beta = 14°$.

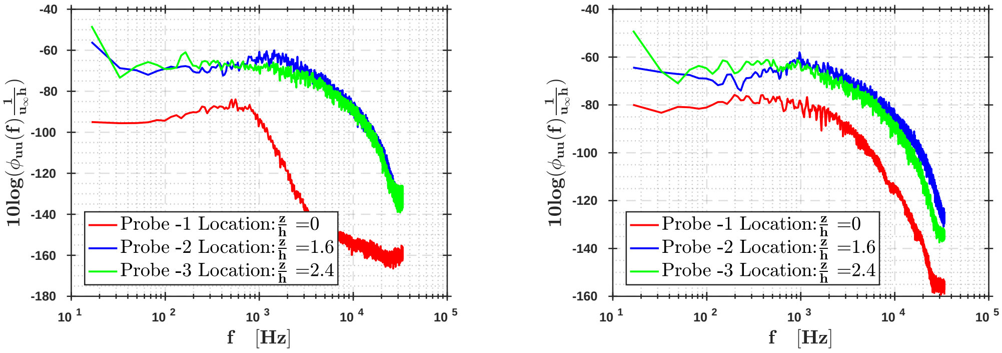

(c) $\beta = 20°$.

(d) $\beta = 30°$.

Figure 5.56: Power spectrum of the spanwise component of velocity at $\frac{x-x_{vg}}{h} = 5$ for RVG vanes at different angle of attack (β).

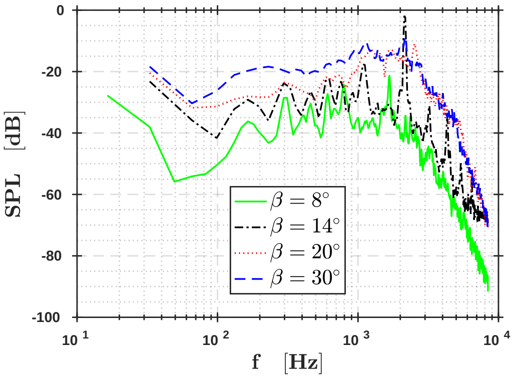

Figure 5.57: SPL Spectrum for RVG at $\beta = 8°, 14°, 20°$and30°.

5.4.2. TRIANGULAR VORTEX GENERATOR

Having discussed the influence of change in angle of attack (β) for the RVGs, we will now consider the same for the TVGs.

MEAN FLOW FILED PROPERTIES

Beginning with the peak streamwise vorticity at different downstream positions, the observed variation with change in β is as shown in Figure 5.58.

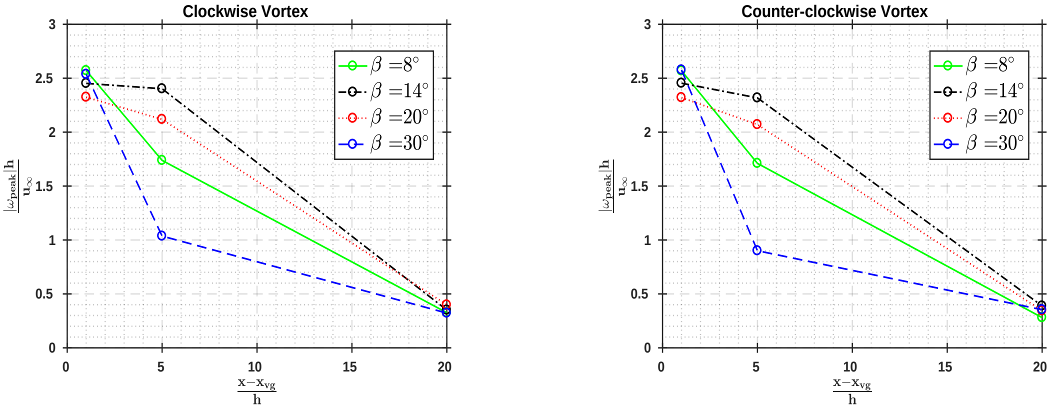

(a) Clockwise Vortex (b) Counter-clockwise Vortex

Figure 5.58: Streamwise evolution $|\omega_{peak}|$ for TVGs at various β.

From Figure 5.58, at $\frac{x-x_{vg}}{h}$ = 1 the observed variation in peak streamwise vorticity is small in comparison to the corresponding change observed in case of RVGs in Figure 5.49. From the experimental and computational results in Shim *et al.* (2015), it is observed that with an increase in β, $|\omega_{peak}|$ also increases. However, the same can not be said about the results at $\frac{x-x_{vg}}{h}$ = 1. Downstream at $\frac{x-x_{vg}}{h}$ = 5, there is a large variation $|\omega_{peak}|$ with change in β. Again, it is seen that these results do not agree with the trend in Shim *et al.* (2015) at this downstream position, with the observed difference being highest for β = 14° and 20°. This is mostly due to the observed difference in the two VG configurations, with VGs considered by Shim being bigger ($\frac{h}{\delta}$ = 1) and longer ($\frac{l}{h}$ = 5). As a result, from the vorticity contour for the TVG vanes in Shim *et al.* (2015) (Figure 14), it is evident that the flow-field differs quite a bit from the observed flow-field in the present study. To illustrate this better, consider the λ_2 visualisation of the mean flow-field around the TVGs at different β shown in Figure 5.59.

From Figure 5.59, the flow-field not only differs from the flow-field in Shim *et al.* (2015) but also changes quite a bit, noticeable in the structure of secondary vortices, with the change in β. With respect to Shim *et al.* (2015), the significant change corresponds to the noted absence of the secondary vortices on the suction side of the VG vane in the results from their study. As a result comparing the two sets of results is not ideal. Moreover, as previously mentioned during the discussion of results for TVGs at β = 14° in Section 5.3.1, the presence of the secondary vortex close to the wall in the wake of the VG vane is not unexpected. Experimental results on longitudinal vortices by Yanagihara and Torii (1993) depicts the presence of the secondary vortex close to the wall. Thereby suggesting that the flow-field visualised in Figure 5.59 is plausible. To further explain the observed variation in $|\omega_{peak}|$ with change in β the streamwise vorticity contour shown in Figure 5.60 is considered.

Figure 5.60 illustrates better, the difference in the flow-field previously noted from the near wake λ_2 visualisation. A notable difference being with regards to the position of the secondary vortices and the number of secondary vortices. In Figure 5.60a and Figure 5.60b corresponding to β = 8° and β = 14°, two distinct secondary vortices having opposite signed vorticity with respect to the primary vortex is visible. However, at β = 20° represented in Figure 5.60c the vorticity contour indicates only one visible secondary vortex and at β = 30° no secondary vortex is the visible in vorticity contour (including data outside the field of view in Figure 5.60d). Based on this it a possible explaination for the observed $|\omega_{peak}|$ is presented. Consider the vortex system illustrated in Figure 5.61, this is similar to the one encountered in Figure 5.60b which corresponds to β = 14°. Additionally $|\omega_{peak}|$ is also maximum for this β at $\frac{x-x_{vg}}{h}$ = 5.

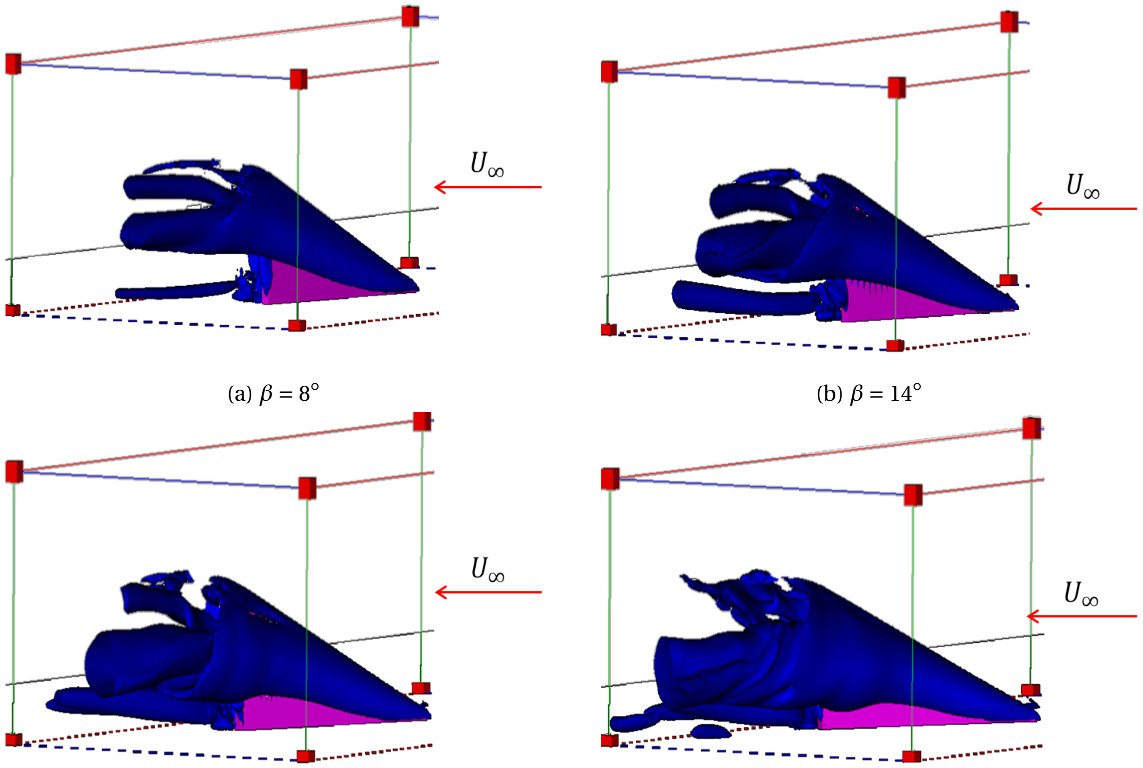

(a) $\beta = 8°$

(b) $\beta = 14°$

(c) $\beta = 20°$

(d) $\beta = 30°$

Figure 5.59: Iso-surface of the λ_2 criteria with a thershold of -1×10^6 in the mean flow-field around the TVGs at $\beta = 8°, 14°, 20°$ and $30°$.

In Figure 5.61, we see that due to the presence of the secondary vortices ($S_{1,2}$) on either side of the primary vortex (P_1), the induced velocity in regions, $R_{1,2}$ due to primary and secondary vortices is oriented in the same direction. Consequently alleviating the process of diffusion in these regions, resulting in a primary vortex which is smaller with concentrated vorticity. Similar argument can be made for the cases, which explains the observed variation in $|\omega_{peak}|$ with change in β at $\frac{x-x_{vg}}{h} = 5$ seen in Figure 5.58.

Computing the circulation (Γ) of the induced primary vortices, as aforementioned in RVGs, but with the size of rectangular region resized to 0.003×0.003m instead of 0.005×0.005m. The observed variation in the magnitude of circulation with change in angle of attack of the VG vane is as shown in Figure 5.62.

Figure 5.62, shows that with increase in β, the strength of the vortex (Γ) also increases. It is to be noted that the observed drop in Γ at $\beta = 30°$ is due to the undersized rectangular region considered for determining Γ and does not reflect the reality. This is so because the primary vortex in case of TVG at $\beta = 30°$ is seen to be diffused much more in comparison to the primary vortices from TVGs at other angles of attack. This is evident in the vorticity contours shown in Figure 5.60.

The observed, spanwise averaged downstream evolution of the boundary layer and shape factor (H) for the TVGs with change in angle of attack of the VG vane is as shown in Figure 5.63.

From Figure 5.63a, for all β the mean boundary layer profile is seen to be fuller at $\frac{x-x_{vg}}{h} = 20$ in comparison to the profile at $\frac{x-x_{vg}}{h} = 1$. This is better illustrated in the variation of H plotted in Figure 5.63b, with the lowest value of H for all β being observed at the corresponding downstream position $\frac{x-x_{vg}}{h} = 20$. Interestingly, comparing these values with the values of H for RVGs in Figure 5.52b, it is observed that the change in H for both the VG profiles is very similar at $\beta = 8°, 14°$ and $20°$, with almost identical H values at $\frac{x-x_{vg}}{h} = 20$. However, the only major difference observed between the RVGs and TVGs is when $\beta = 30°$. With, RVGs it is previously seen that, at high β local re-circulation zones are observed between the VG vanes, however with

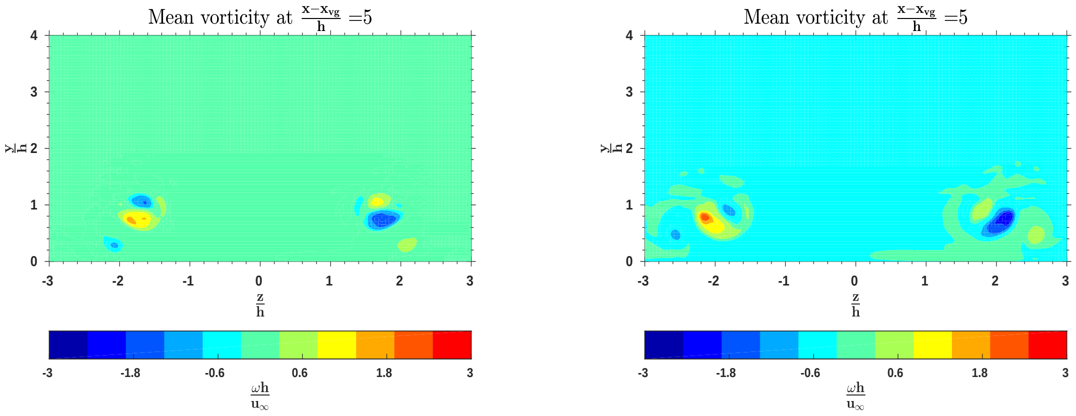

(a) $\beta = 8°$

(b) $\beta = 14°$

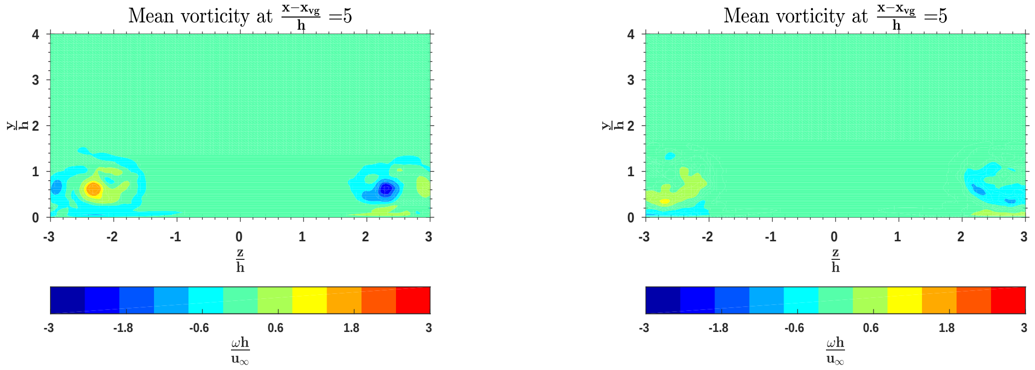

(c) $\beta = 20°$

(d) $\beta = 30°$

Figure 5.60: Streamwise vorticity contour at $\frac{x-x_{vg}}{h} = 5$ for TVGs at various β .

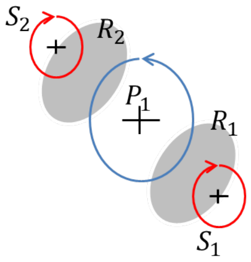

Figure 5.61: Illustration of the vortex sytem for $\beta = 14°$, with primary vortex (P_1) and seondary vortices ($S_{1,2}$).

the TVGs the same is not observed. This is illustrated in the iso-surface of the streamwise component of velocity around the VG vanes shown in Figure 5.64. In Figure 5.64, the regions highlighted indicate streamwise velocity lesser than zero.

Additionally, from Figure 5.64 it can also be observed that with an increase in β the observed re-circulation region at leading edge of the TVGs increases. However, at the trailing edge, with the increase in β beyond 14° it is noticed that recirculation region reduces. This is due to the increase in vortex size evident in the λ_2 visualisation of the flow-field around the VG vanes shown in Figure 5.59.

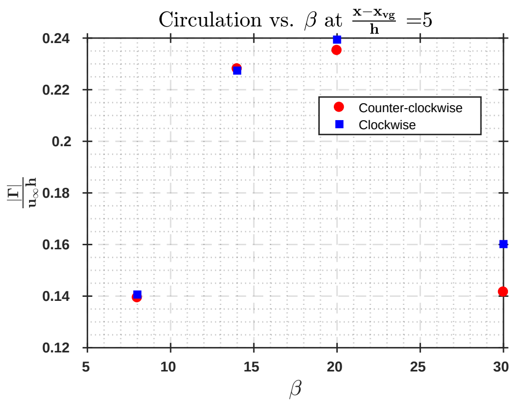

Figure 5.62: Variation in vortex circulation for RVGs with change in β at $\frac{x-x_{vg}}{h}$ = 5.

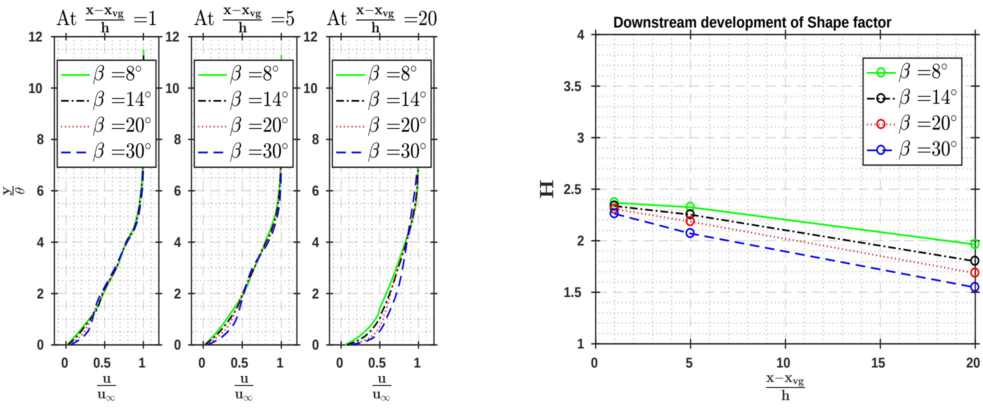

(a) Velocity profile (b) Shape factor

Figure 5.63: Downstream development of the spanwise averaged mean velocity profile and the associated shape factor, H for TVGs at different β.

INSTANTANEOUS FLOW-FIELD PROPERTIES

Considering the instantaneous flow-field properties, the observed variation in magnitude of meandering and preferred direction of motion of the primary vortices at $\frac{x-x_{vg}}{h}$ = 5 with change in angle of attack, β for the TVG vanes is as shown in Figure 5.65.

From Figure 5.65a, it is noted that with an increase in β the magnitude of meandering increases linearly. As in the case of RVGs, the size of the primary vortex for TVGs is also seen to increase with β. Therefore, dividing the obtained magnitude of meandering with the radius of the mean vortex, results in the relative meandering distribution shown in Figure 5.65c. Interestingly, the trend of increasing magnitude with β is observed for relative meandering as well. It is important to note that, in case of the TVGs at low angles of attack the VG vane, the primary vortices are seen to be more elliptical than circular. Therefore the error associated with determining the mean vortex radius is likely to higher in this case, especially in case of $\beta = 14°$. Notwithstanding this, looking back at the key change observed with change in β for TVGs, namely the presence of multiple, more persistent secondary structures at lower β could be a major factor. An indication of this is seen in the plot of the preferred direction of motion of the primary clockwise and counter-clockwise vortices shown in Figure 5.65c. For $\beta = 8°$ and 14° from Figure 5.65, where multiple secondary vortices are observed, the observed direction of motion of the vortices is oriented in a similar manner. At $\beta = 20°$, where only one secondary structure is noticed, the principal direction of motion of the vortices is inverted in comparison to

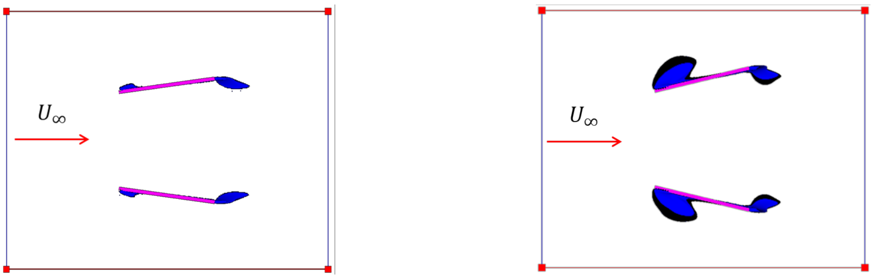

(a) $\beta = 8°$ (b) $\beta = 14°$

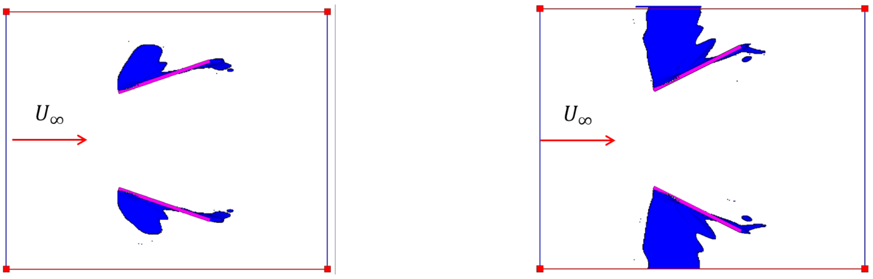

(c) $\beta = 20°$ (d) $\beta = 30°$

Figure 5.64: Variation of local-recirculation zones for TVGs at various β .

the previous angles of attack. However, at $\beta = 30°$, where the presence of secondary vortex at the currently considered downstream position $\frac{x - x_{vg}}{h} = 5$ is not visible in the mean flow-field, the principal direction of motion it is seen to be oriented similar to vortices at $\beta = 20°$ but at different angles.

Further, the results for the power spectrum of the spanwise component of velocity at locations corresponding to Probe-1,2 and three depicted in Section 5.1 for different angles of attack of the TVG vanes is shown in Figure 5.66.

In Figure 5.66, it is seen that, as a result of the different vortex systems observed at different β, multiple dominant frequencies are visible. Even so, it is possible to notice certain similarities in the spectrum which can be related to the observed flow-field. Further illustrating this, at $\beta = 8°$ and 14° where the presence of two secondary structures around the primary is seen, the corresponding spectra in Figure 5.66a and Figure 5.66b indicate of a gradual increase in energy leading upto the spectrum peak. However, in contrast, for $\beta = 20°$ and 30° where either one or no secondary structure is seen around the primary, sharp energy peaks are noted in spectra in Figure 5.66c and Figure 5.66d respectively. The observed most dominant frequencies for the different angles of the TVGs correspond to $f = 1891Hz$, $1085Hz$ and $575.4Hz$ for $\beta = 8°, 20°$ and 30° respectively.

The observed Sound Pressure Level (SPL) spectra for TVGs at different angle of attack of the VG vane is shown in Figure 5.67. The location of the microphone used to compute the spectra is as previously described in Section 5.1.

From Figure 5.67, it is evident that the SPL spectra for the different angles of attack of the TVG vanes are very similar, except for an increase in the SPL level at higher angles. The observed most dominant frequency for various β corresponds to $f = 575Hz$. Comparing this to the SPL spectra for the RVGs at different β, shown in Figure 5.57, it is seen that the spectra for RVGs are not as consistent as the spectra for the TVGs. Moreover, all the dominant frequencies for RVGs are seen to be much higher ($f > 10^3 Hz$) in comparison to the dominant frequencies noted in case of TVGs. Further, for TVGs, at higher frequencies ($f > 10^3 Hz$) it is seen the SPL spectra indicates of rapid decline in the energy content of the acoustic signal, very different from the spectra for the RVGs. Considering that the acoustics waves are generated as a result of the interaction of the flow-field with the VG vanes, a significant difference observed between the two sets of VGs is the presence of leading edge separation/re-circulation on the suction side of the VG vane, only in case of the RVGs. For the TVGs, owing to its profile, leading edge separation on the suction side is not noted. Additionally, with an increase

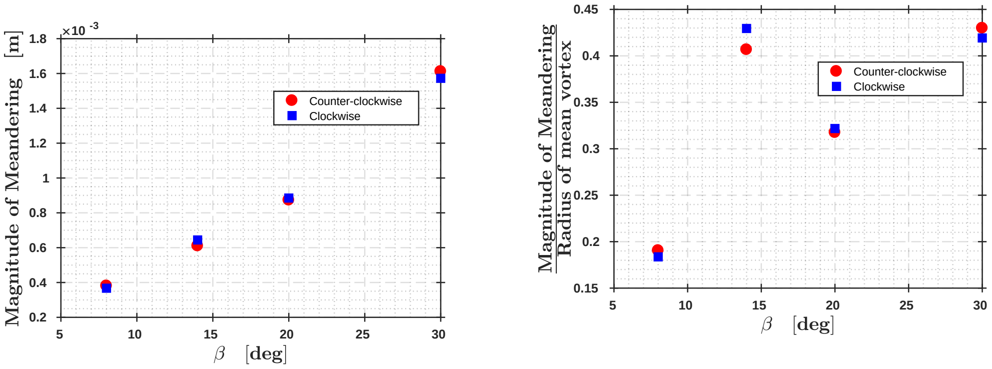

(a) Variation of the magnitude of meandering.

(b) Variation of the magnitude of meandering with respect to the corresponding mean vortex radius.

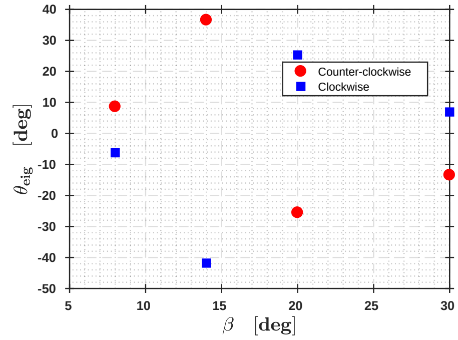

(c) Variation of chracteristic angle, θ_{eig}.

Figure 5.65: Variation of meandering characteristics for TVG with change in β at $\frac{x-x_{vg}}{h} = 5$.

in the angle of attack of the VG vane for the RVGs, it is seen in Figure 5.53, that the leading edge separation is also increasing. This is expected to influence the formation and interaction of the vortices with the VG vanes, consequently, responsible for some of the observed differences in the SPL spectra.

The Overall Sound Pressure Level (OASPL) for the TVGs at the different angle of attack of the VG vane, computed from the SPL spectra is tabulated in Table 5.2. Comparing the values of OASPL for TVGs with the corresponding OASPL values for RVGs, it is evident that TVGs are less noisy. The observed difference is approximately $15dB$ at $\beta = 14°$ and $20°$.

β [deg]	8°	14°	20°	30°
OASPL [dB]	-12.26	-13.045	-12.27	-8.96

Table 5.2: Variation of OSPL with β for TVG

Finally, comparing the power spectra of the spanwise component of velocity in Figure 5.66 with the SPL spectra in Figure 5.67, except at $\beta = 30°$, the most dominant frequency at different angles of the TVG vane are not comparable. Thereby suggesting that the some of the dominant frequencies previously noted develops as a result of the induced vortex system and not due to interaction with the VG vane. These results need to be interpreted with caution, as it is not clear if one single vortex or a combination of vortices are responsible for the observed peak at these frequencies. However, one of the possibility, as previously noted, could be due to the presence of vortex instability. Nevertheless, a more detailed study is necessary to ascertain the source and causality of the noted dominant frequencies at different angles of the TVG vanes.

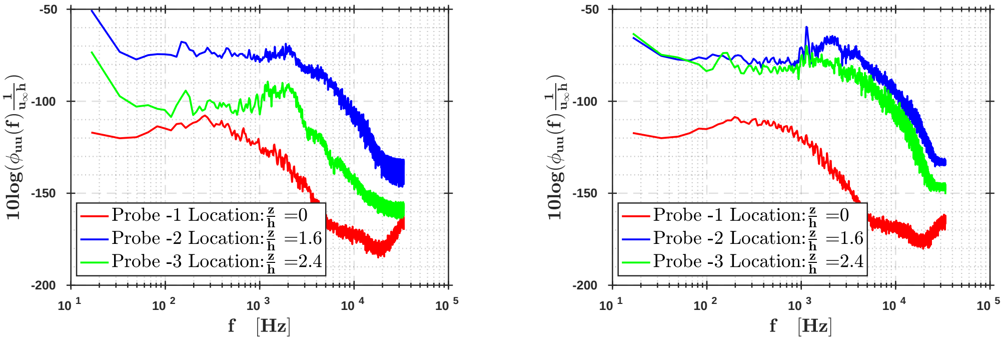

(a) $\beta = 8°$.

(b) $\beta = 14°$.

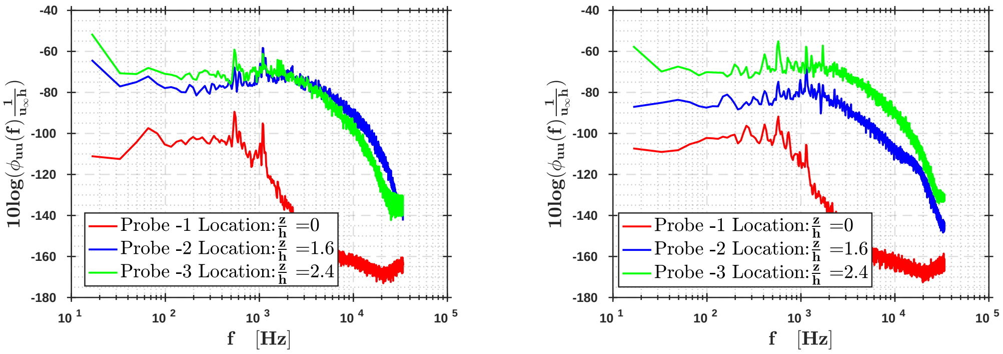

(c) $\beta = 20°$.

(d) $\beta = 30°$.

Figure 5.66: Power spectrum of the spanwise component of velocity at $\frac{x-x_{vg}}{h} = 5$ for TVG vanes at different angle of attack (β).

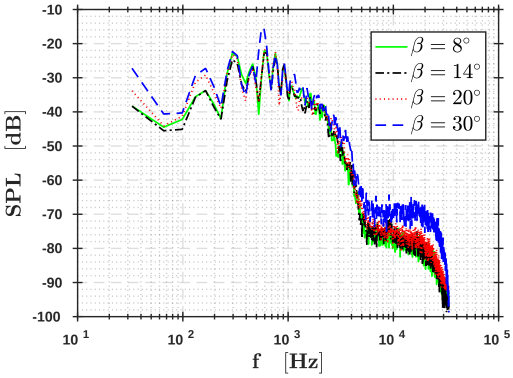

Figure 5.67: SPL Spectra for TVGs at $\beta = 8°, 14°, 20°$and$30°$.

Overall based on the above results, it is possible to make the following observations with the change in angle of attack of the VG vane:

- For both RVGS and TVGs, it is noted that the peak streamwise vorticity in the mean flow-field is seen to be influenced by the secondary structures, which in turn are seen to be sensitive to change in angle of attack of the VG vane.

- Increasing the angle of attack of the VG vanes is seen to increase local-recirculation zones for both TVGs and RVGs. More so, for RVGs with large local-recirculation zones being noted in between the VG vanes.
- The magnitude of meandering is seen to increase with an increase in angle of attack of the VG vanes for both RVGs and TVGs.
- The OASPL for RVGs is seen to increase with an increase in angle of attack of VG vanes. However, for TVGs, OASPL is found to similar at lower angles ($\beta = 8°, 14°$ and $20°$) which is seen to only increase at a very high angle ($\beta = 30°$).

6

CONCLUSIONS AND RECOMMENDATIONS

In the final chapter, the main findings of this thesis are summarised in section 6.1. The recommendations and potential areas of further research is presented in section 6.2.

6.1. CONCLUSIONS

The primary goal of the current study is to characterise the properties of the flow field induced by the sub-boundary layer vortex generators (SBVGs). To this end, *PowerFLOW 5.3b* a commercial Lattice Boltzmann solver is used to simulate the flow field. Two different vortex generator profiles, rectangular vortex generators (RVGs) and triangular vortex generators (TVGs) subjected to a laminar boundary layer are used to analyse the flow field. The main findings of this thesis are summarised as answers to the research questions stated in Section 1.3.1.

What are the general properties of the flow-field induced by SBVGs?

- The instantaneous flow indicates the presence of distorted vortex structures. In contrast, the mean flow shows the presence of circular vortices, due to averaging of the data.

- In the mean flow the primary vortices induced by the VGs move away from each other, and away from the wall as well.

- In the mean flow, peak streamwise vorticity of the primary vortex, just aft of the VG vanes depends on the interaction of the primary vortex with the secondary structures. In turn, these secondary structures are sensitive to the angle of attack (β) of the VG vanes.

- Peak streamwise vorticity of the primary vortices in the mean flow decays rapidly downstream of the VG vanes. For RVGs, at $\beta = 14^\circ$ peak streamwise vorticity $20h$ downstream of the VG, reduces to approximately 10% of the initial value. Similarly, for TVGs, peak streamwise vorticity decreases to 32% of the initial value.

How does the VG profile influence the induced flow-field?

- VG profile influences the origin and sign of secondary structures. For RVGs, secondary structures originate as horseshoe vortices from the leading edge of the VG vane. For TVGs, two secondary vortices, one originating on the surface of VG vane and the other just aft of the trailing edge of the VG vane. Further, for both the profiles secondary structures are noted to be sensitive to change in angle of attack of the VG vane.

- VG profile influences the general flow around the vanes, with emergence different local-recirculation zones in the mean flow on changing the VG profile. These recirculation zones are also observed to be sensitive to change in angle of attack of the VG vane. Of the two VG profiles considered, RVGs are more susceptible to change in angle of attack with recirculation zones present in between the VG vanes as well.

What is the influence of the induced vortices on the downstream development of the boundary layer?

- For both RVGs and TVGs in the mean flow, the boundary layer is fuller with an increase in downstream distance. At the farthest downstream position considered ($20h$ from the VG vanes), the shape-factor is seen to reduce with increase in angle of attack of the VG vanes.

What are the characteristics of unsteady nature of the induced vortices?

- For both RVGs and TVGs, the magnitude of meandering increases with the downstream position. Increasing the angle of attack of the VG vanes also increased the magnitude of meandering.
- The preferred direction of motion of the primary vortices is influenced by the nearest neighbouring vortex.
- Probes downstream of both RVGs and TVGs indicate the presence certain dominant frequencies. For RVGs, results show that the dominant frequency is related to the primary vortex formation and interaction with the VG vanes. However, for TVGs multiple dominant frequencies are observed, and its origin is not clear. One of the possibility is the presence of vortex instabilities. However, to confirm this, linear stability analysis considering the observed vortex system is necessary.

What is the contribution of SBVGs to far-field noise?

- The contribution of SBVGs to far-field noise is minimal. For RVGs, overall sound pressure level (OASPL) increases with increase in angle of attack of the VG vane. In the current study, for RVGs the highest OASPL corresponds to $4.54 dB$ at $\beta = 30°$. However, TVGs are not very sensitive to angle of attack of VG vane, with an increase in OASPL noted at only high angles. For TVGs, at $\beta = 30°$ the OASPL is $-8.94 dB$.

This study has provided detailed insights into the flow-field induced RVGs and TVGs in a laminar boundary layer. The results show that the flow-field induced by the different VG profiles are unique, although parameters such as shape factor indicating the effectiveness of theses devices show similar trends. More so, the uniqueness is more pronounced in regions just aft of the VG vanes, where secondary vortices are prominent. With multiple parameters such as peak streamwise vorticity in the mean flow and meandering motion being influenced by the secondary structures, it appears to play a significant role in the evolution of the primary vortices. Recalling that the use of SBVG is limited to situations with relatively-fixed regions of flow separation, effectively managing the secondary vortices using suitable design changes to the VG profile, could be one possible approach to increase its operating range.

NOTE ON THE VORTEX IDENTIFICATION TECHNIQUE

During this study, it is observed that some of the widely used vortex identification methods discussed in Section 4.4 might not be suitable for flows with multiple vortices in proximity interacting with each other. As a result, to alleviate this problem, a combination of vortex identification methods is used in this thesis. However, Haller (2005) points out that, the classical description of the vortex in Section 4.4 is only Galilean invariant but not objective. Subsequently, Haller observes that these classical definitions 'identify different structures as vortices in frames that rotate relative to each other'. Thus it is essential to use a definition of a vortex which does not change with an arbitrary change in the reference frame, i.e. an objective definition of a vortex to identify structures. More so, in flows involving interacting vortices. Since this was realised very late in this thesis, it is strongly recommended that in future studies involving interacting vortices, using an objective definition of a vortex as suggested by Haller be considered.

This limitation implies that the unsteady characteristics of the vortices extracted using the modified criteria need to interpreted more cautiously.

6.2. RECOMMENDATIONS AND FUTURE RESEARCH

Based on the observations in the previous sections, the recommended areas of future research include:

- Investigating the unsteady characteristics of vortices induced by VGs in a turbulent boundary layer (TBL). This would be a natural progression of the current work. In this frame of work, it would be intriguing to assess the influence of freestream turbulence on the properties of the induced vortex. Additionally, it would be interesting to also consider the influence of adverse pressure gradient in a TBL setting. Results from these studies can offer interesting findings which can help design more efficient flow control devices.

- Linear stability analysis with the induced vortex system as the base flow. This can provide some valuable information on the instability, its wavelength and growth rate. The resultant data can further be used to support results from experiments and simulation.
- Experimental studies to visually capture the vortex core motion using techniques such as dye visualisation could provide more definitive information on vortex meandering. These qualitative results could be very beneficial to validate the computational results.
- Evaluating the acoustic performance by either simulating VGs on a section of the blade or the entire blade, if possible. Considering that there are hundreds of VGs on a modern wind turbine blade, these finding can provide insights into their collective acoustic behaviour which could be helpful for the future design and optimisation processes.

A

APPENDIX

A.1. TURBULENT BOUNDARY LAYER VALIDATION

Initially, in addition to laminar boundary layer (LBL), a turbulent boundary layer (TBL) was also to be used in the current study. However, due to the shortage of time further post-processing of results for the TVGs in TBL was not possible. Nevertheless, considerable effort went into the generation of TBL. Hence the results for TBL validation is presented here.

Before assessing the properties of the flow-field induced by the VGs in the presence of TBL, it is necessary to confirm that the general properties of the TBL itself agree with theory and empirical knowledge. The technique of bypass transition, previously described in Section 2.1.1 is used to generate the required turbulent boundary layer. To this end, an appropriate zigzag strip is used. Previous studies, both experimental and computational have suggested that using zigzag strips is one of most effective techniques for triggering bypass transition (Van Rooij et al., 2003 [75]; Elsinga et al., 2012 [76]; van der Velden, 2017 [21]). Braslow et al. (1958) [77] suggested that the minimum roughness height required for bypass transition can be determined based on a critical Reynolds number (Re_k) defined as:

$$Re_k = \frac{u_{ht} h_{strip}}{\nu} \tag{A.1}$$

where u_{ht} is the velocity at the tip of the roughness of height h_{strip}. Van Rooij et al. (2003) [75] points out that for zigzag strips $Re_k = 200$ is sufficient. Using the laminar boundary layer thickness at the location of the strip, δ_0 ($\approx 5mm$) the corresponding Blasius profile (see Section 2.1.1) with the same thickness is re-represented in Figure A.1 as a function of local height and velocity.

From Figure A.1, it is seen that the minimum height of zigzag strip required for $Re_k = 200$ is $0.6mm$. Thus with a certain factor of safety, h_{strip} is chosen as $0.12mm$. For the spanwise length/pitch of one zigzag element in the strip, Elsinga et al. (2012) [76] in the experimental investigation of flow around zigzag strips, suggests selecting a value between δ_0 and $2.8\delta_0$. This is because, the maximum spatial energy growth for the LBL is observed in the wavelengths with a magnitude between δ_0 to $2.8\delta_0$ (Andersson et al., 1999 [78]). Following this, the pitch of the zigzag strip is selected as $5mm$. The dimension of the zigzag strip is summarised in Table A.1.

Type	**Height [m]**	**Pitch [m]**	**Streamwise length [m]**	**Re at tip**
Zigzag Strip	0.0012	0.005	0.01	500

Table A.1: Zigzag Strip details

In Figure A.2, results for the mean value of the streamwise component of velocity in a plane parallel to the wall at $\frac{y}{h_{strip}} = 1$ is shown. The contour plot indicates to the presence of vortex streaks directly downstream

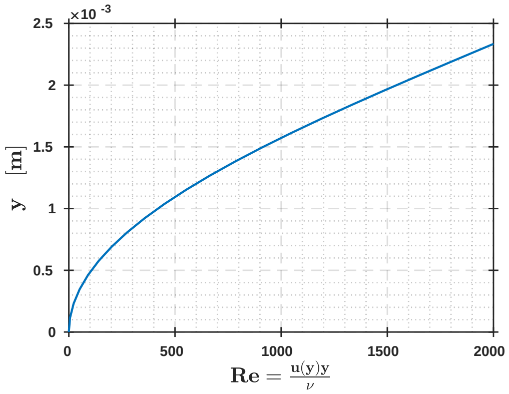

Figure A.1: Blasius profile as a function of height and corresponding local Reynolds number, *Re*

of the zigzag strip, characterised by regions of low speed flow. This is further elucidated by visualising the vortices using the λ_2 - criteria (see Section 4.4) in a volume surrounding the zigzag strip, shown in Figure A.3.

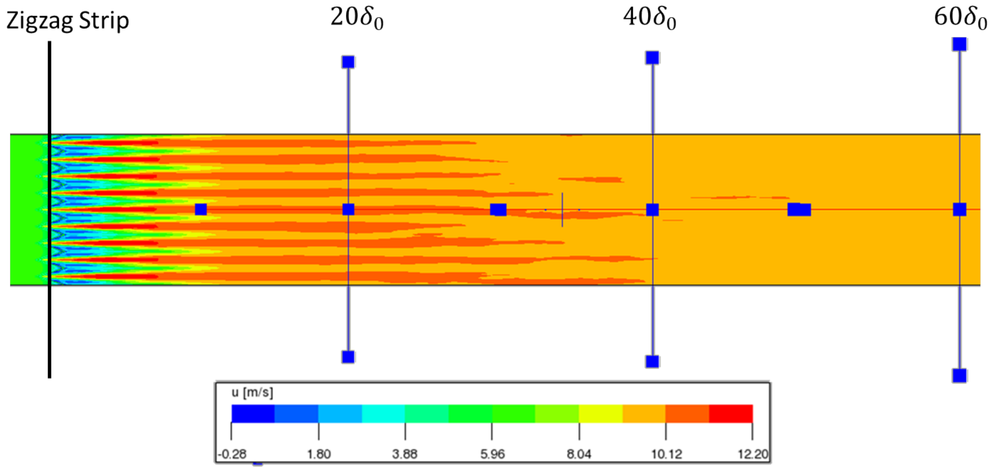

Figure A.2: Mean value of streamwise velocity in a plane parallel to the wall at $\frac{y}{h_{strip}} = 1$.

Returning to Figure A.2, it is seen that, as we move downstream from the zigzag strip, the spanwise uniform nature of the boundary layer flow is gradually regained. This indicates that the flow features induced by the zigzag strip are no longer coherent. At the downstream position, $60\delta_0$ variation in the streamwise velocity is seen to be minimal. The mean velocity profile at this downstream position, in terms of the outer layer and inner layer variables, is shown in Figure A.4.

In Figure A.4, the mean velocity profiles are compared with the measurements of zero pressure gradient turbulent boundary layer by Osterlund et al. (2001) [14]. Scaling the velocity profile with the outer layer variables Figure A.4a, there is a good agreement between experimental and simulated velocity profile in all regions, except very close to the wall. This is expected, as the influence of approximations such as the wall function and turbulence model is highest in this region. The same argument holds for the observed difference in the velocity profile when scaled using the inner layer variables in Figure A.4b. In fact, the influence of both the wall model and turbulence model is more pronounced here, as the computation of the scaling parameter u_τ is dependent on these approximations. Notwithstanding, the trends in the velocity profile in Figure A.4b are similar.

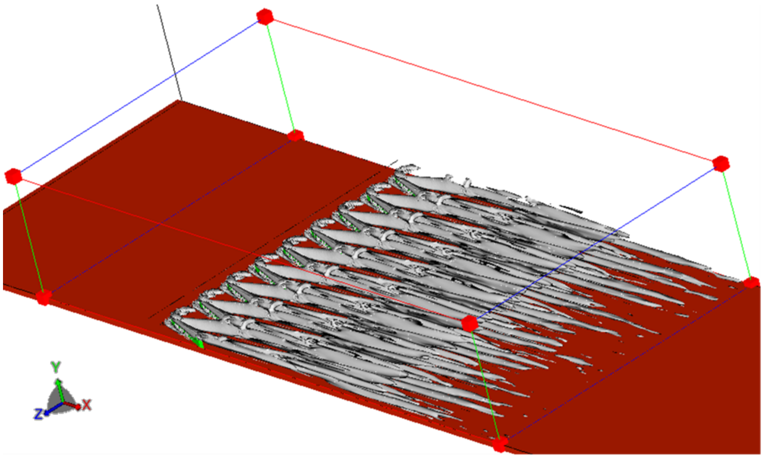

Figure A.3: Iso- surface of λ_2 - criteria in the mean flow-field around the zigzag strip, with a threshold of -1×10^5.

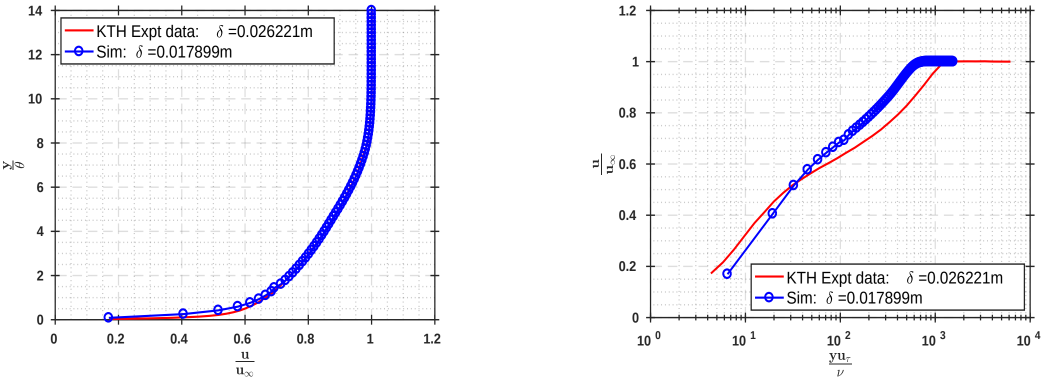

(a) Velocity profile in terms of outer layer variables

(b) Velocity profile in terms of inner layer variables

Figure A.4: Comparision of mean velcity profile at downstream station $60\delta_0$ with Osterlund et al. (2001) [14].

In Figure A.5, the Reynolds shear stress $(\overline{u'v'})$ for the simulated velocity profile at the downstream position $60\delta_0$, is compared with the results of Adrian et al. (2000) [17]. Visually comparing Figure A.5a with Figure A.5b, it is seen that the trends agree quite well.

Thus, based on the above results, at $60\delta_0$ downstream of the zigzag strip, the simulated boundary layer can be regarded as fully developed and free from the coherent structures induced by the zigzag strip.

A.1.1. COMPUTATIONAL SETUP FOR TURBULENT BOUNDARY LAYER CASE

For the turbulent boundary layer case, the previously used setup the laminar boundary layer flow is modified to accommodate the zigzag strips. An illustration of the modified domain is shown Figure A.6.

At the inlet, a laminar Blasius profile with boundary layer thickness (δ) of $4mm$ and freestream velocity, $u_\infty = 15m/s$ is prescribed. This laminar flow is tripped by a zigzag strip placed at a distance of $50mm$ from the start of the domain. The details of the resultant turbulent boundary layer flow are discussed in Section A.1. The thickness of the resultant boundary layer is found to be approximate $18mm$ at the position of VG vanes. The selection of this downstream location is also discussed in Section A.1. Consequently, the height of the VG vanes (h) is set at $9mm$, so that $\frac{h}{\delta}$ consistent at 0.5. The summary of both the cases is tabulated in Table A.2.

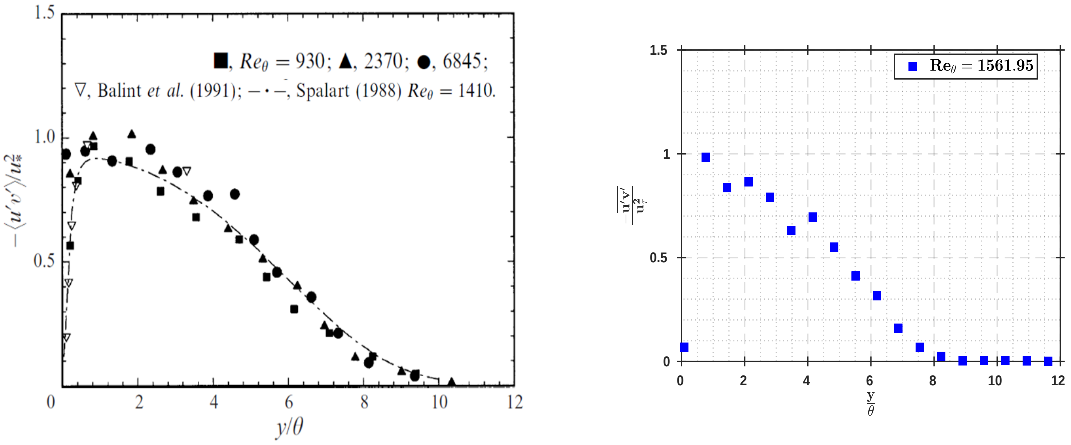

(a) Reynolds shear stress for various Re_θ from Adrian et al. (2000) [17]

(b) Reynolds shear stress from from simulation at downstream position $60\delta_0$

Figure A.5: Comparision of Reynolds shear stress scaled in inner layer variables and plotted with outer layer variables.

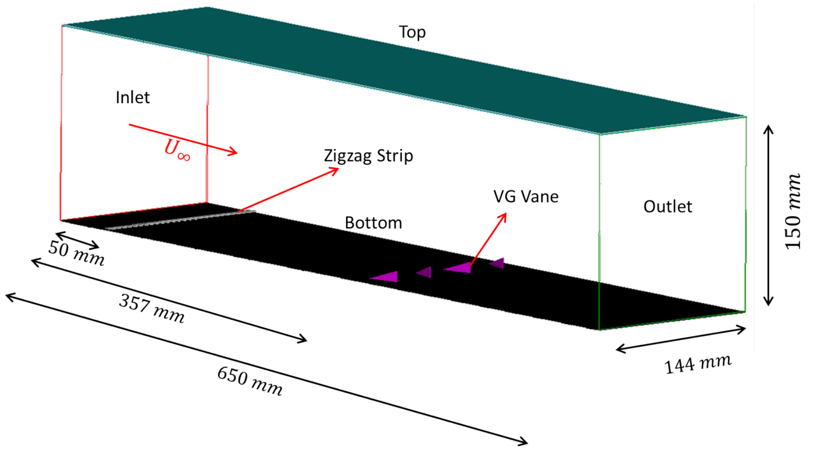
Top
Inlet
U_∞
Zigzag Strip
VG Vane
Bottom
Outlet
150 mm
50 mm
357 mm
650 mm
144 mm

Figure A.6: Illustration of the computational domain for turbulent boundary layer flow.

	LBL	**TBL**
Domain Length	500 mm	650 mm
Domain Height	150 mm	150 mm
Domain Width	80 mm	144 mm
Inlet	Blasius Profile, $\delta = 9mm$, $u_\infty = 15m/s$	Blasius Profile, $\delta = 4mm$, $u_\infty = 15m/s$
Trip	No	At $x = 50mm$
X_{VG}	150 mm	357 mm
δ_{VG}	10 mm	18 mm
h	5 mm	9 mm

Table A.2: Summary of the Computational Domain.

BIBLIOGRAPHY

[1] *Wind energy,* .

[2] F. M. White and I. Corfield, *Viscous fluid flow*, Vol. 3 (McGraw-Hill New York, 2006).

[3] L. G. Pack and R. D. Joslin, *Overview of active flow control at nasa langley research center,* in *5th Annual International Symposium on Smart Structures and Materials* (International Society for Optics and Photonics, 1998) pp. 202–213.

[4] Y. A. Cengel and J. M. Cimbala, *Fluid dynamics: Fundamentals and applications,* Seoul, Korea: McGraw-Hill Korea (2006).

[5] H. Schlichting, *Boundary-layer theory, 7th edn mcgraw-hill,* New York , 66 (1979).

[6] S. B. Pope, *Turbulent flows,* (2001).

[7] S. Wagner, R. Bareiss, and G. Guidati, *Wind turbine noise* (Springer Science & Business Media, 2012).

[8] O. Jianu, M. A. Rosen, and G. Naterer, *Noise pollution prevention in wind turbines: status and recent advances,* Sustainability **4**, 1104 (2012).

[9] P. Ashill, J. Fulker, and K. Hackett, *A review of recent developments in flow control,* Aeronautical Journal **109**, 205 (2005).

[10] K. Angele and F. Grewe, *Instantaneous behavior of streamwise vortices for turbulent boundary layer separation control,* Journal of Fluids Engineering **129**, 226 (2007).

[11] P. Cathalifaud, G. Godard, C. Braud, and M. Stanislas, *The flow structure behind vortex generators embedded in a decelerating turbulent boundary layer,* Journal of turbulence , N42 (2009).

[12] T. Leweke, S. Le Dizès, and C. H. Williamson, *Dynamics and instabilities of vortex pairs,* Annual Review of Fluid Mechanics **48**, 507 (2016).

[13] N. Forestier, L. Jacquin, and P. Geffroy, *The mixing layer over a deep cavity at high-subsonic speed,* Journal of Fluid Mechanics **475**, 101 (2003).

[14] J. M. Osterlund and A. V. Johansson, *'turbulence statistics of zero pressure gradient turbulent boundary layers,* (2001).

[15] J. C. Lin, *Review of research on low-profile vortex generators to control boundary-layer separation,* Progress in Aerospace Sciences **38**, 389 (2002).

[16] H. Shim, Y.-H. Jo, K. Chang, K.-J. Kwon, and S.-O. Park, *Wake characteristics of vane-type vortex generators in a flat plate laminar boundary layer,* International Journal of Aeronautical and Space Sciences **16**, 325 (2015).

[17] R. J. Adrian, C. D. Meinhart, and C. D. Tomkins, *Vortex organization in the outer region of the turbulent boundary layer,* Journal of Fluid Mechanics **422**, 1 (2000).

[18] M. Wang, J. B. Freund, and S. K. Lele, *Computational prediction of flow-generated sound,* Annu. Rev. Fluid Mech. **38**, 483 (2006).

[19] F. van den Berg, E. Pedersen, J. Bouma, and R. Bakker, *Visual and acoustic impact of wind turbine farms on residents,* (2008).

[20] E. Maris, P. J. Stallen, R. Vermunt, and H. Steensma, *Noise within the social context: Annoyance reduction through fair procedures,* The Journal of the Acoustical Society of America **121**, 2000 (2007).

[21] W. C. P. van der Velden, *Computational Aeroacoustic Approaches for Wind turbine blade noise prediction,* PhD dissertation, Technische Universiteit Delft (2017).

[22] W. Blake, *Mechanics of flow-induced sound and vibration, vol. ii: Complex flow-structure interactions academic,* New York (1986).

[23] T. F. Brooks and M. A. Marcolini, *Airfoil tip vortex formation noise,* AIAA journal **24**, 246 (1986).

[24] C. K. Tam, *Computational aeroacoustics: an overview of computational challenges and applications,* International Journal of Computational Fluid Dynamics **18**, 547 (2004).

[25] N. Curle, *The influence of solid boundaries upon aerodynamic sound,* in *Proceedings of the Royal Society of London A: Mathematical, Physical and Engineering Sciences*, Vol. 231 (The Royal Society, 1955) pp. 505–514.

[26] J. F. Williams and D. L. Hawkings, *Sound generation by turbulence and surfaces in arbitrary motion,* Philosophical Transactions of the Royal Society of London A: Mathematical, Physical and Engineering Sciences **264**, 321 (1969).

[27] F. Farassat, *Linear acoustic formulas for calculation of rotating blade noise,* AIAA journal **19**, 1122 (1981).

[28] H. D. Taylor, *The elimination of diffuser separation by vortex generators,* United Aircraft Corporation, East Hartford, CT, Technical Report No **4012**, 3 (1947).

[29] J. Lin, F. Howard, and G. Selby, *Small submerged vortex generators for turbulent flow separation control,* J. Spacecr. Rockets **27**, 503 (1990).

[30] R. Mehta and P. Bradshaw, *Longitudinal vortices imbedded in turbulent boundary layers part 2. vortex pair with 'common flow'upwards,* Journal of Fluid Mechanics **188**, 529 (1988).

[31] D. M. Rao and T. T. Kariya, *Boundary-layer submerged vortex generators for separation control-an exploratory study,* in *AIAA, ASME, SIAM, and APS, National Fluid Dynamics Congress* (1988) pp. 839–846.

[32] B. J. Wendt and T. Biesiadny, *Initial circulation and peak vorticity behavior of vortices shed from airfoil vortex generators,* (2001).

[33] G. Godard and M. Stanislas, *Control of a decelerating boundary layer. part 1: Optimization of passive vortex generators,* Aerospace Science and Technology **10**, 181 (2006).

[34] C.-S. Yao, J. C. Lin, and B. G. Allan, *Flow-field measurement of device-induced embedded streamwise vortex on a flat plate,* (2002).

[35] C. M. Velte, C. Braud, S. Coudert, and J. Foucaut, *Vortex generator induced flow in a high re boundary layer,* in *Journal of Physics: Conference Series*, Vol. 555 (IOP Publishing, 2014) p. 012102.

[36] O. Lögdberg, J. H. Fransson, and P. H. Alfredsson, *Streamwise evolution of longitudinal vortices in a turbulent boundary layer,* Journal of Fluid Mechanics **623**, 27 (2009).

[37] C. M. Velte, V. Okulov, and I. Naumov, *Regimes of flow past a vortex generator,* Technical Physics Letters **38**, 379 (2012).

[38] W. J. Devenport, M. C. Rife, S. I. Liapis, and G. J. Follin, *The structure and development of a wing-tip vortex,* Journal of Fluid Mechanics **312**, 67 (1996).

[39] L. Jacquin, D. Fabre, D. Sipp, V. Theofilis, and H. Vollmers, *Instability and unsteadiness of aircraft wake vortices,* Aerospace Science and technology **7**, 577 (2003).

[40] L. Jacquin, D. Fabre, D. Sipp, and E. Coustols, *Unsteadiness, instability and turbulence in trailing vortices,* Comptes Rendus Physique **6**, 399 (2005).

[41] J. Schröttle, A. Dörnbrack, and U. Schumann, *Excitation of vortex meandering in shear flow,* Fluid Dynamics Research **47**, 035508 (2015).

[42] D. Harris and C. Williamson, *Instability of secondary vortices generated by a vortex pair in ground effect,* Journal of Fluid Mechanics **700**, 148 (2012).

[43] B. Gardarin, L. Jacquin, and P. Geffroy, *Flow separation control with vortex generators,* in *AIAA 4th Flow Control Conference, Seattle, WA, June* (2008) pp. 23–26.

[44] C. Yao, J. Lin, and B. Allen, *Flowfield measurement of device-induced embedded streamwise vortex on a flat plate,* in *1st Flow Control Conference* (2002) p. 3162.

[45] P. L. Bhatnagar, E. P. Gross, and M. Krook, *A model for collision processes in gases. i. small amplitude processes in charged and neutral one-component systems,* Physical review **94**, 511 (1954).

[46] S. Chen and G. D. Doolen, *Lattice boltzmann method for fluid flows,* Annual review of fluid mechanics **30**, 329 (1998).

[47] V. Yakhot and S. A. Orszag, *Renormalization group analysis of turbulence. i. basic theory,* Journal of scientific computing **1**, 3 (1986).

[48] D. Casalino, A. F. Ribeiro, E. Fares, and S. Nölting, *Lattice–boltzmann aeroacoustic analysis of the lagoon landing-gear configuration,* AIAA journal (2014).

[49] B. E. Launder and D. B. Spalding, *The numerical computation of turbulent flows,* Computer methods in applied mechanics and engineering **3**, 269 (1974).

[50] F. Farassat and G. P. Succi, *A review of propeller discrete frequency noise prediction technology with emphasis on two current methods for time domain calculations,* Journal of Sound and Vibration **71**, 399 (1980).

[51] D. Casalino, *An advanced time approach for acoustic analogy predictions,* Journal of Sound and Vibration **261**, 583 (2003).

[52] W. van der Velden, S. Pröbsting, A. van Zuijlen, A. de Jong, Y. Guan, and S. Morris, *Numerical and experimental investigation of a beveled trailing-edge flow field and noise emission,* Journal of Sound and Vibration **384**, 113 (2016).

[53] L. Jahanshaloo, E. Pouryazdanpanah, and N. A. Che Sidik, *A review on the application of the lattice boltzmann method for turbulent flow simulation,* Numerical Heat Transfer, Part A: Applications **64**, 938 (2013).

[54] S. Succi, *The lattice Boltzmann equation: for fluid dynamics and beyond* (Oxford university press, 2001).

[55] T. Leweke and C. Williamson, *Cooperative elliptic instability of a vortex pair,* Journal of fluid mechanics **360**, 85 (1998).

[56] P. J. Roache, *Quantification of uncertainty in computational fluid dynamics,* Annual review of fluid Mechanics **29**, 123 (1997).

[57] J. Jeong and F. Hussain, *On the identification of a vortex,* Journal of fluid mechanics **285**, 69 (1995).

[58] R. W. Metcalfe, A. Hussain, S. Menon, and M. Hayakawa, *Coherent structures in a turbulent mixing layer: a comparison between direct numerical simulations and experiments,* in *Turbulent Shear Flows 5* (Springer, 1987) pp. 110–123.

[59] D. Bisset, R. Antonia, and L. Browne, *Spatial organization of large structures in the turbulent far wake of a cylinder,* Journal of Fluid Mechanics **218**, 439 (1990).

[60] M. S. Chong, A. E. Perry, and B. J. Cantwell, *A general classification of three-dimensional flow fields,* Physics of Fluids A: Fluid Dynamics **2**, 765 (1990).

[61] J. C. Hunt, A. A. Wray, and P. Moin, *Eddies, streams, and convergence zones in turbulent flows,* (1988).

[62] Q. Chen, Q. Zhong, M. Qi, and X. Wang, *Comparison of vortex identification criteria for planar velocity fields in wall turbulence,* Physics of Fluids **27**, 085101 (2015).

[63] P. Chakraborty, S. Balachandar, and R. J. Adrian, *On the relationships between local vortex identification schemes,* Journal of fluid mechanics **535**, 189 (2005).

[64] L. Graftieaux, M. Michard, and N. Grosjean, *Combining piv, pod and vortex identification algorithms for the study of unsteady turbulent swirling flows,* Measurement Science and technology **12**, 1422 (2001).

[65] Y. Huang and M. A. Green, *Detection and tracking of vortex phenomena using lagrangian coherent structures,* Experiments in Fluids **56**, 147 (2015).

[66] H. Pearcy, *Boundary layer and flow control: Its principle and applications, vol. 2,* (1961).

[67] V. Vatsa and J. Carter, *Analysis of airfoil leading-edge separation bubbles,* AIAA journal **22**, 1697 (1984).

[68] C. Roy, T. Leweke, M. C. Thompson, and K. Hourigan, *Experiments on the elliptic instability in vortex pairs with axial core flow,* Journal of Fluid Mechanics **677**, 383 (2011).

[69] L. Jacquin, D. Fabre, P. Geffroy, and E. Coustols, *The properties of a transport aircraft extended near field: an experimental study,* in *AIAA conference proceedings*, Vol. 1038 (2001).

[70] B. Pershing, *Separated Flow Past Slender Delta Wings with Secondary Vortex Simulation*, Tech. Rep. (AEROSPACE CORP EL SEGUNDO CA, 1964).

[71] J. Yanagihara and K. Torii, *Heat-transfer augmentation by longitudinal vortices rows,* Experimental Thermal and Fluid Science **7**, 137 (1993).

[72] M. L. S. Indrusiak and S. V. Möller, *Wavelet analysis of unsteady flows: Application on the determination of the strouhal number of the transient wake behind a single cylinder,* Experimental Thermal and Fluid Science **35**, 319 (2011).

[73] C. M. Velte, M. O. Hansen, and V. L. Okulov, *Helical structure of longitudinal vortices embedded in turbulent wall-bounded flow,* Journal of Fluid Mechanics **619**, 167 (2009).

[74] G. Haller, *An objective definition of a vortex,* Journal of fluid mechanics **525**, 1 (2005).

[75] R. Van Rooij and W. Timmer, *Roughness sensitivity considerations for thick rotor blade airfoils,* Transactions-American Society of Mechanical Engineers Journal of Solar Energy Engineering **125**, 468 (2003).

[76] G. Elsinga and J. Westerweel, *Tomographic-piv measurement of the flow around a zigzag boundary layer trip,* Experiments in fluids **52**, 865 (2012).

[77] A. L. Braslow and E. C. Knox, *Simplified method for determination of critical height of distributed roughness particles for boundary-layer transition at mach numbers from 0 to 5,* (1958).

[78] P. Andersson, M. Berggren, and D. S. Henningson, *Optimal disturbances and bypass transition in boundary layers,* Physics of Fluids **11**, 134 (1999).